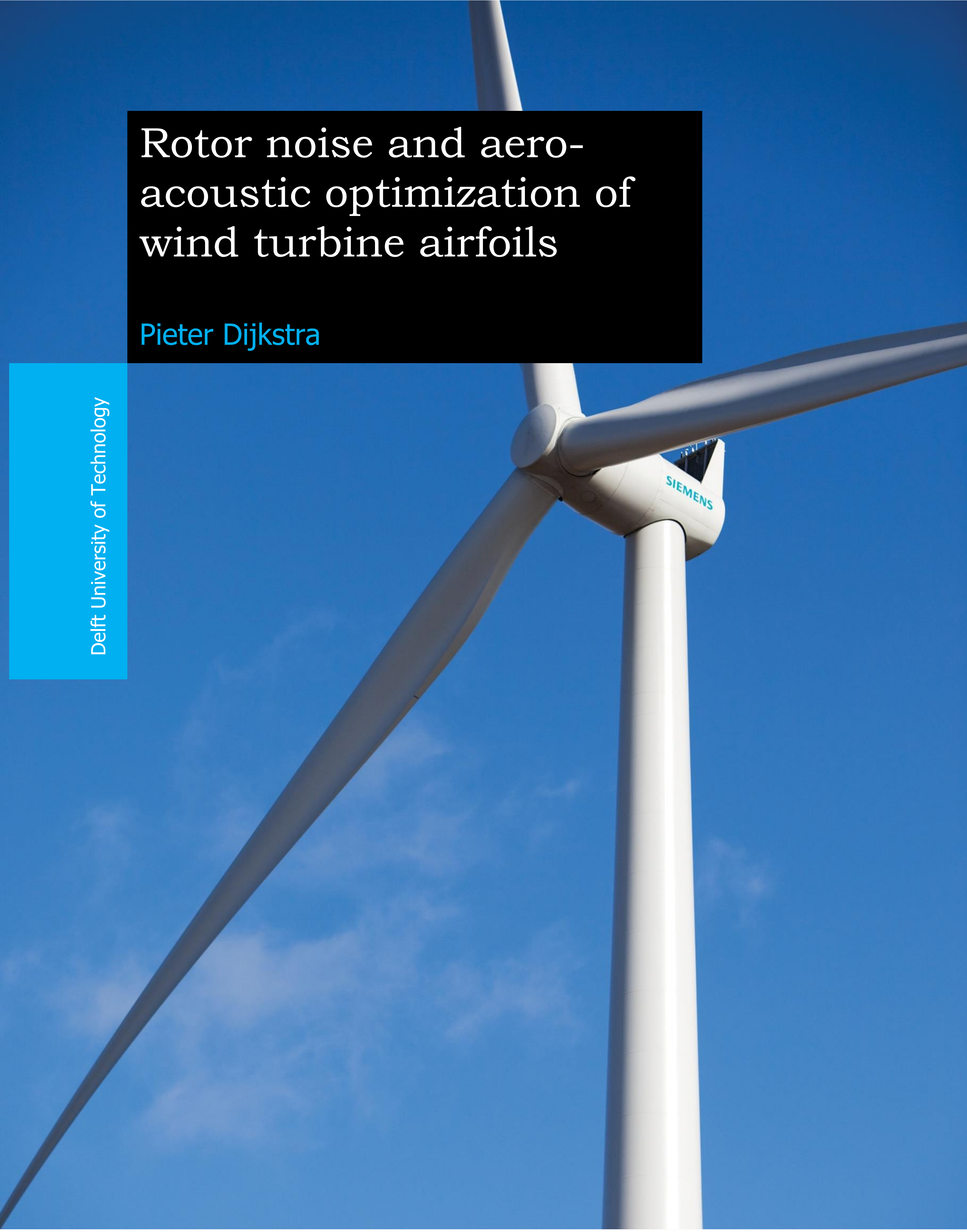

Rotor noise and aero-acoustic optimization of wind turbine airfoils

Pieter Dijkstra

Delft University of Technology

Challenge the future

Rotor noise and aero-acoustic optimization of wind turbine airfoils

By

Pieter Willem Dijkstra

in partial fulfilment of the requirements for the degree of

Master of Science
in Sustainable Energy Technology

at the Delft University of Technology,
to be defended publicly on 8 July 2015

Supervisor: Ir. W. A. Timmer
Thesis committee: Prof. dr. G. J. W. van Bussel, TU Delft
Dr. D. Ragni, TU Delft
Dr. Ir. B.W. van Oudheusden, TU Delft

Acknowledgements

This master thesis is completed in the Wind Energy department as a part of the master program in Sustainable energy technology.

In this section, I would first like to express my gratitude towards my supervisor, Nando Timmer, who helped me during the course of this thesis. His knowledge and recommendations regarding wind turbine airfoils and wind energy in general aided me in completing this work.

Through my supervisor, I was put in contact with Gael de Oliveira Andrade, who also helped me a tremendous amount during this project. He introduced me to the topic of optimization and was always willing to help me with solving problems I had with the optimizer. Without the several long sessions in which he provided me with advice this would not be possible.

The road towards this moment was long and hard. Last but not least I owe big thanks to the people that surround me. Family and friends kept supporting me throughout the process by motivating and encouraging me. They were an indispensable factor in completing this journey.

P. Dijkstra
Zoetermeer, June 2015

Abstract

The thesis is focused on designing a tip-region airfoil for a multi-MW wind turbine. It is approached with the objective of optimizing the geometry of the airfoil for the best trade-off between aero-acoustics and aerodynamic requirements. Using the wind turbine noise prediction tool SILANT it is established that trailing edge noise is the most dominant noise source. Reduction of airfoil self-noise should therefore focus on this noise mechanism. A modified version of the semi-empirical aero-acoustic prediction code by Brooks, Pope and Marcolini is used to compute this trailing edge noise. The panel code RFOIL is used for the boundary layer computations as well as the generation of the aerodynamic polars. A quality assessment of both codes is performed based on aerodynamic and acoustic wind tunnel measurements acquired by the Institut für Aerodynamik und Gasdynamik on the NACA 64_3-418 airfoil. The multi-objective optimization is executed using the genetic algorithm NSGA-II. The airfoil parameterization that is used is the Class Shape Transformation (CST) method by Kulfan. The results of the optimization are captured in the Pareto front and six individuals are assessed thoroughly. It is found that airfoils can be designed that fulfill all the aerodynamic requirements. Acoustically, only marginal differences can be observed and further research should be conducted on the topic.

Contents

List of Tables

List of Figures

Nomenclature

Latin:

$\overline{D}_{h,}\overline{D}_{l}$	High and low frequency directivity functions	[-]
$\overline{u_2^2}$	RMS of vertical velocity fluctuations	[m^2/s^2]
a	Axial induction factor	[-]
A	Effective rotor aera	[m/s^2]
A	(II) spectral shape function for TBL-TE noise	[dB]
a’	Tangential induction factor	[-]
B	(II) spectral shape function for separation stall noise	[dB]
c	chord	[m]
C(x)	Class function	[-]
C_d	Drag coefficient	[-]
C_f	Skin friction coefficient	[-]
CF_{aero}	Aerodynamic cost function score	[-]
CF_{sound}	Acoustic cost function score	[-]
C_l	Lift coefficient	[-]
$C_{l,design}$	Design lift coefficient	[-]
C_m	Moment coefficient	[-]
c_o	Speed of sound	[m/s]
C_p	Power coefficient	[-]
C_T	Thrust coefficient	[-]
f	frequency	[Hz]
f	Tip/hub loss correction factor	[-]
F_N	Normal force	[N]
F_T	Tangential force	[N]
I	Sound intensity	[W/m^2]
I_{ref}	Reference sound intensity	[W/m^2]
K_1	Scaling term TBL-TE noise	[dB]
K2	Scaling term TBL-TE noise	[dB]
k_e	Wave number of energy-containing eddies	[m^{-1}]
k_i	Wave number vector	[m^{-1}]
L_2	Vertical turbulence length scale	[m]
L_{att}	Atmospheric attentuation	[dB]
L_{CA}	Convective amplification	[dB]
L_{day}	Equivalent sound level during the day	[dB]
L_{den}	Equivalent sound level day evening night	[dB]

$L_{evening}$	Equivalent sound level during the evening	[dB]
l_m	Turbulent mixing length	[m]
L_{meteo}	Refraction and ground effect	[dB]
L_{night}	Equivalent sound level during the night	[dB]
L_p	Sound Pressure Level	[dB]
$L_{p,inflow}$	Inflow noise Sound Pressure level	[dB]
$L_{p,TBL-TE}$	Turbulent Boundary Layer-Trailing Edge sound pressure level	[dB]
L_{spread}	Geometrical spreading	[dB]
L_w	Sound Power Level	[dB]
Ma	Mach number	[-]
M_c	Convection Mach number	[-]
P_{AoA}	Angle of attack gap penalty function	[-]
$P_{Cl,des}$	Design lift penalty function	[-]
P_i	Penalty function	[-]
p_{ref}	Reference pressure	[Pa]
p_{rms}	Root means squre sound pressure	[Pa]
P_{th}	Trailing edge thickness penalty function	[-]
Q	Torque	[Nm]
R	Rotor radius	[m]
r_e	Source-receiver distance	[m]
Re	chord Reynolds number	[-]
s	Segment width	[m]
S(x)	Shape function	[-]
St	Strouhal number	[-]
T	Thrust	[N]
u^*	Friction velocity	[m/s]
U_0	Undisturbed flow velocity	[m/s]
u_i	Velocity vector	[m/s]
V_{hub}	Wind speed at hub height	[m/s]
V_{ref}	Wind speed at reference height	[m/s]
W	Wake function	[-]
z(x)	Trailing Edge Thickness function	[-]
z_o	Roughness length	[m]
ΔK1	Scaling term TBL-TE noise	[dB]

Greek:

α	Angle of attack	[°]
α_{design}	Design angle of attack	[°]
α_{Gauss}	Gaussian constant	[-]
α_{max}	Stall angle of attack	[°]
δ	Boundary layer thickness	[m]
δ^*	Boundary layer displacement thickness	[m]
θ	Boundary layer momentum thickness	[m]
θ_r	angle between the blade flow velocity and the source-observer line	[°]
θ_t	Twist angle	[°]
κ	Von Karman constant	[-]
μ	Dynamic viscosity	$[m^2/s]$
ν	Kinematic viscosity	[kg/(ms)]
ρ	Density	$[kg/m^3]$
T_w	Wall shear stress	[Pa]
ϕ	Inflow angle	[°]
Φ_{22}	Vertical velocity fluctuations spectrum	[m/s]
Φ_m	Moving axis spectrum	[m/s]
φ_r	angle between plane of the blade and plane containing the chord line and the observer	[°]
Ω	Rotational velocity	[rad/s]

Subscripts

p	Pressure side
s	Suction side
α	Angle dependent
Clean	Clean conditions
Rough	Rough conditions

List of abbreviations

AoA - Angle of Attack
BEM - Blade Element Momentum
BL - Boundary Layer
BPM - Brooks, Pope & Marcolini
BPO - Bernstein Polynomial Order
CF - Cost function
CFD - Computational Fluid Dynamics
CPV - Coherent Particle Velocity
CST - Class Shape Transformation
FW-H - Ffowcs Williams-Hawking
GA - Genetic Algorithm
GBA - Gradient-Based Algorithm
GWEC - Global Wind Energy Council
IAG - Institut für Aerodynamik und Gasdynamik
LWT - Laminar Wind Tunnel
NAFNoise - NREL AirFoil Noise
NASA - National Aeronautics and Space Association
NLR - Dutch Aerospace Laboratory
NREL - National Renewable Energy Laboratory
NURBS - Non-Uniform Rational B-Spline
NWEA - Nederlandse Wind energie associatie
OAPWL - Overall Average Power Watt Level
OASPL - Overall Average Sound Power Level
SPL - Sound Power Level
TBL-TE - Turbulent Boundary Layer – Trailing Edge
TNO - Netherlands Organization for Applied Scientific Research
V&C - Viterna & Corrigan
WWEA - World Wind Energy Association

1. Introduction

Initially, wind energy was mainly used to aid people in their daily lives. It was used for transportation and mobility, by using the wind to sail ships from one point to another. The other main applications were to grind grain and pumping water by using wind mills. The latter was especially done in the Netherlands. Later, due to the invention of the steam engine the role of wind energy reduced significantly. The tasks that were performed by using the power in the wind were now taken over by steam engines.

Then in the late 1960s, but especially in the 1970s, events happened that triggered the development of wind energy and changed its role once again. In the late 1960s, events began to unfold that led to a big global oil oil crisis in the 1970s. With the decrease in oil supply, while demand remained at level, a shortage in oil developed, which led to high prices. This led to an increased awareness that the fossil fuel reserves of the earth are finite. This awareness was strengthened by books and studies such as *Limits to Growth* (Meadows et al. 1972), which was published during this time. In this book the interaction between human activities and the possible impacts it has on the Earth was pointed out.

By the 1990s, the change that had been initiated in the 1960s continues, and the role of wind energy had changed again. It was also in this decade that the shift towards larger wind turbines was made, and the MW-size wind turbine was developed. Furthermore, in 1997, the Kyoto protocol was signed, a binding agreement between (initially) 37 countries that implemented the objective to fight global warming by reducing greenhouse gas concentrations in the atmosphere. These events combined stimulated the large number of government funded research and development programmes on renewable energies in general and wind energy in particular.

1.1. Wind energy worldwide

Nowadays, the use of wind energy to generate electricity is widely used across the world. In the recent few years, the worldwide energy production that comes from the wind has been increasing every year (WWEA 2014). By the end of June 2014, worldwide wind capacity reached 336.3 GW, which amounts to roughly 4% of the world’s electricity demand. Moreover, the yearly growth in recent years has been over 12%. Reasons mentioned for this relatively positive development of the worldwide wind market include: economic advantages, increasing competitiveness relative to other sources of electricity as well as the pressing need to implement emission free technologies in order to mitigate climate change and air pollution (WWEA 2014).

Of the total installed capacity, the five traditional wind countries –China, USA, Germany, Spain and India- combined represent 72% of the global wind capacity. As can be seen in Figure 1.1, the capacity is expected to keep increasing according to the forecast of the Global Wind Energy Council (GWEC 2014).

Table 1.1: top 10 leading countries & the Netherlands in wind energy production (WWEA 2014)

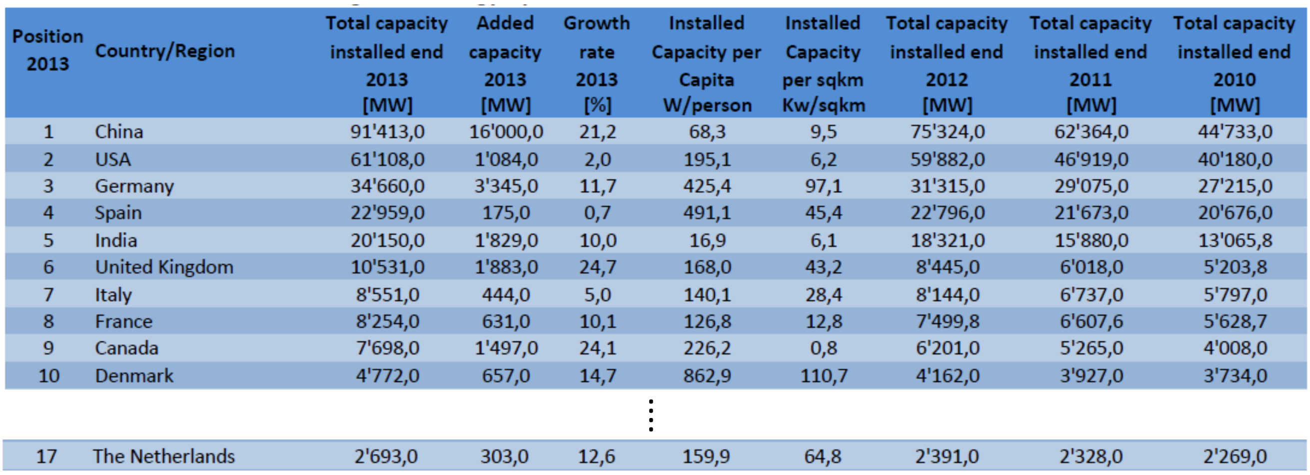

Position 2013	Country/Region	Total capacity installed end 2013 [MW]	Added capacity 2013 [MW]	Growth rate 2013 [%]	Installed Capacity per Capita W/person	Installed Capacity per sqkm Kw/sqkm	Total capacity installed end 2012 [MW]	Total capacity installed end 2011 [MW]	Total capacity installed end 2010 [MW]
1	China	91'413,0	16'000,0	21,2	68,3	9,5	75'324,0	62'364,0	44'733,0
2	USA	61'108,0	1'084,0	2,0	195,1	6,2	59'882,0	46'919,0	40'180,0
3	Germany	34'660,0	3'345,0	11,7	425,4	97,1	31'315,0	29'075,0	27'215,0
4	Spain	22'959,0	175,0	0,7	491,1	45,4	22'796,0	21'673,0	20'676,0
5	India	20'150,0	1'829,0	10,0	16,9	6,1	18'321,0	15'880,0	13'065,8
6	United Kingdom	10'531,0	1'883,0	24,7	168,0	43,2	8'445,0	6'018,0	5'203,8
7	Italy	8'551,0	444,0	5,0	140,1	28,4	8'144,0	6'737,0	5'797,0
8	France	8'254,0	631,0	10,1	126,8	12,8	7'499,8	6'607,6	5'628,7
9	Canada	7'698,0	1'497,0	24,1	226,2	0,8	6'201,0	5'265,0	4'008,0
10	Denmark	4'772,0	657,0	14,7	862,9	110,7	4'162,0	3'927,0	3'734,0
				⋮					
17	The Netherlands	2'693,0	303,0	12,6	159,9	64,8	2'391,0	2'328,0	2'269,0

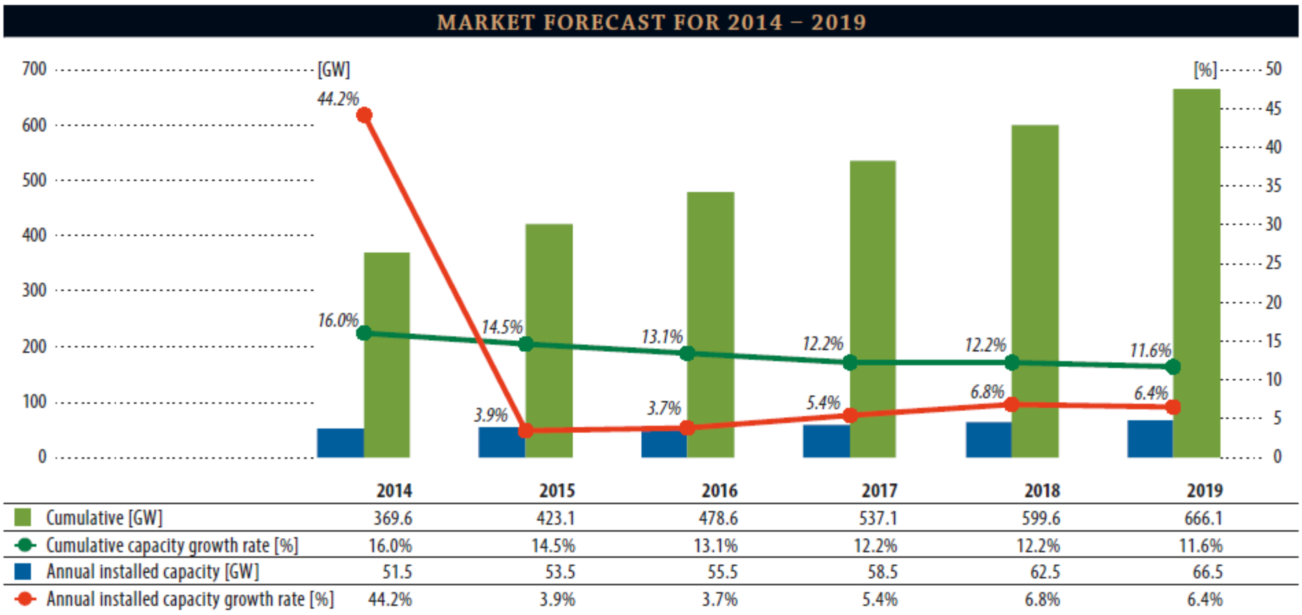

	2014	2015	2016	2017	2018	2019
🟩 Cumulative [GW]	369.6	423.1	478.6	537.1	599.6	666.1
● Cumulative capacity growth rate [%]	16.0%	14.5%	13.1%	12.2%	12.2%	11.6%
🟦 Annual installed capacity [GW]	51.5	53.5	55.5	58.5	62.5	66.5
● Annual installed capacity growth rate [%]	44.2%	3.9%	3.7%	5.4%	6.8%	6.4%

Figure 1.1: Wind energy market forecast for the period 2014-2019 (GWEC 2014)

1.1.1. Wind energy in the Netherlands

In light of the Kyoto protocol, to reduce the carbon emission in the Earth's atmosphere, as well as an agreement between countries within the European Union, the Netherlands has set some objectives concerning the installed capacity in the (near) future. Since one wind turbine with a capacity of 3 MW prevents the emission of approximately 4,000 tons of CO_2, the Netherlands has set the following targets (NWEA 2015):

- 2020: 6000 MW of onshore as well as off shore wind turbine installed capacity
- 2050: A total installed capacity of 26,000 MW; 6,000 MW on shore and 20,000 off shore

These targets imply that in 2020, about 14% of the total electricity consumption must be produced by renewable energy sources. From the report of the GWEC, the installed capacity at the end of 2014 was 2,805 MW. Of this total capacity, 247 MW comes from offshore wind turbines; the remaining power is produced on shore. Since the newly installed power over 2014 amounts to 141 MW, the targets will not be met at the current rate.

1.2. Environmental impact

As is the case with all technologies, also wind turbines have flaws and disadvantages. Despite being environment friendly, the installation of wind turbines often leads to resistance from within the community. A commonly mentioned excuse being: ‘not in my backyard’, to point out that people do want to benefit from wind energy, but are not if it affects their own living area. The potential negative effects can be divided into the following categories:

- *Birds/bat interaction* – negative effects include: death due to collision with a wind turbine and loss of natural habitat
- *Visual impact* – as is the case with all objects, wind turbines too have a visual impact on the landscape
- *Electromagnetic interference* – wind turbines cause electromagnetic interference which can affect radio signals and other communication that occurs through electromagnetism.
- *Land use impact* – obviously, the siting of wind turbines occupies space.
- *Wind turbine noise* – Wind turbines radiate sound towards the environment due to either mechanical (rotary equipment) or aerodynamic reasons. People might be annoyed by this and some reports even mention physical discomfort.

All of the categories are addressed at some stage of a wind project. Each country has its own rules and regulations, but they can also differ from one region to another. This is why each project should make a separate analysis as to which limitations might affect the project.

The problem of wind turbine noise has been one of the most studied environmental impact subjects. Although noise can be measured objectively, the impact it has on its surrounding and how it is perceived is subjective. Besides the subjective ‘annoyance’, the impact of wind turbine noise might even include health problems such as sleep disturbance, reduced concentration and stress (Colby et al. 2009).

1.3. Regulations on wind turbine noise

In order to minimize the aforementioned negative noise effects and discomfort, the government has issued noise limits. These rules and regulations can differ, as stated before, from country to country or even from region to region.

Currently, in the Netherlands, the noise limits are as follows. In contrast to other countries, the Netherlands makes no distinction between rural and residential areas; the noise level is only related to a ‘noise-sensitive receptor’, e.g. a house. The yearly averaged equivalent sound level L_{den} may not exceed 47dB. This equivalent sound level comprises of the sound level, during the day, evening and night. The subscript ‘den’ refers to these three periods. The day is hereby defined as the period between 07:00 and 19:00, the evening is between 19:00 and 23:00 and the night is during the remaining hours, 23:00 and 07:00. Furthermore, the measured sound level during the evening is increased by 5 dB, during the night even 10 dB. The yearly averaged equivalent sound level is now calculated by the following formula:

$$L_{den} = 10\log\left(\frac{12}{24}10^{\frac{L_{day}}{10}} + \frac{4}{24}10^{\frac{L_{evening}+5}{10}} + \frac{8}{24}10^{\frac{L_{night}+10}{10}}\right) \tag{1.1}$$

How the terms in the equation are defined and measured exactly, is described in (IEC 61400-11 2002). In addition, a limit has been imposed for the yearly averaged sound level during the night, which amounts to 41 dB. Furthermore, a 5 dB penalty is added if the sound spectrum shows any severe tonal peaks. However, in practice, this is seldom done because in general, especially for modern day wind turbines, severe tonal noise is not present.

Other countries have different legislation regarding the sound limit. For instance, in some countries different noise limits exist for each region. However, each country has one thing in common: rules apply regarding wind turbine noise. Therefore each wind project should take this under consideration.

1.4. Wind turbine noise research

The previous paragraphs pointed out the negative effects as well as the legislation that applies in order to diminish them. One of the ways to tackle these problems is to explore the possibilities to decrease the sound emission by wind turbines. This thesis is focused on designing a low noise wind turbine airfoil in order to reduce aerodynamic noise. An attenuation of the noise level could have the following advantages:

- Public acceptance might increase. Wind turbine noise is one of the main reasons that people are reluctant to have wind turbines placed nearby. If this could be reduced, their opposition against wind energy might decrease.
- Wind turbine operation could be more efficient. As explained, the noise limit during the night is stricter than during the day, while the wind speed often increases at night. The consequence is that, due to a possibility of exceeding the sound limit, the wind turbine might have to operate at a reduced power setting. The power production is now lower than what could potentially be generated. This could be avoided if the noise emission is reduced.
- More wind energy sites could become available. Since the noise limit is related to the nearest ‘noise-sensitive receptor’, e.g. a house, a reduction of the noise emission can lead to a reduction of the minimum radius to a noise-sensitive object. Previously unsuitable sites might become suitable after noise reduction measures.
- The energy production per unit area might increase. If for instance reduction of sound by 3 dB could be achieved, twice the amount of the same turbines could be placed in the same area. So this could potentially double the power production for the same area.

1.5. Report overview

The topic of this thesis is to optimize horizontal axis wind turbines, both aerodynamically and aero-acoustically. For this, it is first necessary to briefly introduce the reader to the most fundamental knowledge necessary to understand the basics. Chapter 2 and 3 therefore outlines these basic knowledge of both aerodynamics and acoustics. Then, in chapter 4, the types of noise that play a role in the total noise emission are explained. In the chapter that follows, chapter 5, an initial analysis will be performed in order to determine the of aerodynamic noise on a rotor level. Chapter 6 & 7 will then focus on selecting and validating a noise prediction model. The three chapters that succeed, 8, 9 and 10, the various aspects regarding optimization and airfoil parameterization will be outlined. The final three chapters will describe both the optimization settings and discuss the results of the optimization, as well as conclude on these optimization results.

2. Wind turbine aerodynamics

This chapter begins by outlining the basics description of the geometry of an airfoil in order to familiarize the reader with this, if necessary. In the paragraph that follows, the basics of wind turbine aerodynamics is introduced. This is done by outlining the actuator disc model and the Blade Element Momentum (BEM) theory. These are interesting models to get a grasp of which parameters of an airfoil are of major importance from an aerodynamic point of view. The final section of the chapter introduces the boundary layer theory of Prandtl. It is important to apprehend the basics of this topic for the properties of the boundary layer play an import role in the prediction of aerodynamic noise.

2.1. Airfoil aerodynamics and terminology

The structures that are used to generate these mechanical forces that rotate are called airfoils. This is due to the relative motion of the airfoil and the surrounding fluid (mostly air). In order to generate mechanical power that is converted to electric power, the blade of a wind turbine makes use of airfoils. The cross-section of a blade has the shape of an airfoil. Across the span of the blade, the shape of the cross-section deviates, so a blade consists of multiple airfoils. This is illustrated in Figure 2.1 below. The width and length of a blade are a function of various aspects: the desired aerodynamic performance, the desired rotor power as well as structural considerations. The basic aspects of airfoil aerodynamics as well as the terminology are briefly touched upon in this section.

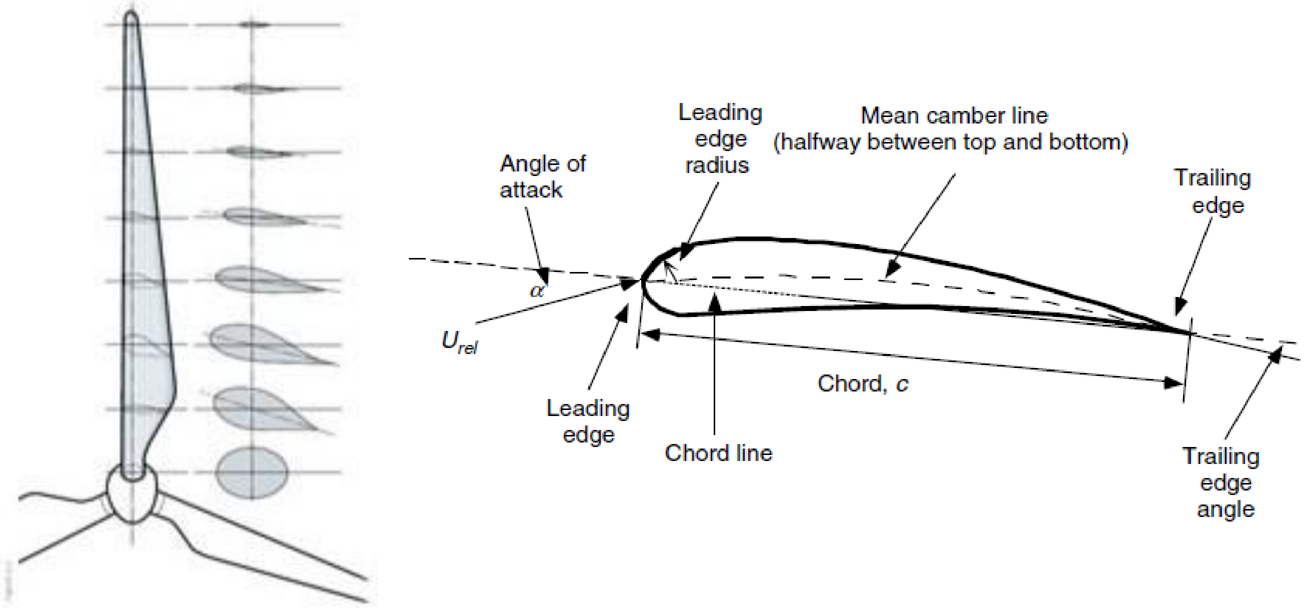

Figure 2.1: distribution of airfoils over a blade (left) (Comsa 2015) and the airfoil nomenclature (right) (Manwell et al. 2002)

First, the terminology related to the airfoil is described. The most forward and backward points of the airfoil are termed leading and trailing edge, respectively. The straight line connecting these points is the chord line of the airfoil; the distance along the chord line between these two points is the chord *c*. The line halfway between the upper and lower surfaces from leading to trailing edge is the mean camber line. The thickness of the airfoil is defined as the distance between the upper and lower surfaces. Finally, the camber is designated by the distance between the mean camber line and the chord line, measured perpendicular to the chord line. ; This is all graphically represented in Figure 2.1 above.

The airflow over the airfoil produces a distribution of forces over the airfoil surface. The flow velocity increases on the upper side of the airfoil resulting in a lower pressure, therefore named ‘suction’ side, compared to the lower or ‘pressure’ side. Adjacent to the surface of the airfoil, the airflow is slowed down due to viscous friction. This phenomenon is described in further detail in the section 0.

The resultant of these pressure and viscous forces is decomposed into two main forces, one perpendicular and one parallel to the flow direction, and a moment that act at a position along the chord line at a distance of c/4 from the leading edge. They are defined as follows:

Lift force – defined perpendicular to the direction of the oncoming flow. The lift force is the result of an unequal pressure on the lower and the upper side of the airfoil.

Drag force – defined parallel to the direction of the oncoming air flow. The drag force consists of a contribution due to viscosity and a contribution as a result of unequal pressures on the surfaces facing toward and away from the oncoming flow.

Pitching moment – defined about an axis perpendicular to the airfoil cross-section. This torque is a result of the net lift and drag forces that act on the airfoil.

These definitions are used to characterize the way the airfoil reacts to certain flow conditions. The most important non-dimensional parameter to define the flow conditions is the Reynolds number. It is defined by the relation:

$$Re = \frac{\rho U c}{\mu} = \frac{Uc}{\nu} \tag{2.1}$$

This parameter describes the ratio between the inertial forces and the viscous forces on the airfoil. In the expression, ρ is the density of air, μ is the dynamic viscosity and $\nu = \mu/\rho$ represents the kinematic viscosity. Furthermore U and c denote the flow velocity and the chord length, respectively. The Reynolds number is one of the key parameters that play a role in how the airfoil, and consequently the blade, performs and it will be mentioned frequently in the coming chapters.

Additionally, the forces and moment can be described by non-dimensionalized parameters as well. Usually, airfoil performance expressed in two-dimensional coefficients, determined for a range of angles of attack and Reynolds numbers. If a section of the blade is considered, the coefficients are denoted by lower case subscripts, as in C_d for the two-dimensional drag coefficient. In this case, the coefficients are defined by the lift and drag on that section (per unit span), both normalized by the dynamic pressure, respectively. They are expressed in the following way:

$$C_l = \frac{L/l}{1/2\, \rho U_0^2 c} \tag{2.2}$$

$$C_d = \frac{D/l}{1/2\, \rho U_0^2 c} \tag{2.3}$$

$$C_m = \frac{M/l}{1/2\, \rho U_0^2 c^2} \tag{2.4}$$

In the expressions, the density is represented by ρ, U_0 is the undisturbed air flow velocity, c is the chord length and the l is the sectional span. In the next section it will be explained how these forces relate to the incoming flow velocity and how this contributes to the power production of the wind turbine.

2.2. Actuator disc concept

The function of a wind turbine rotor is to extract the kinetic energy of the incoming flow by reducing the velocity upstream of the rotor and converting it to a rotation of the blade. Because of this, it is inevitable that the rotor experiences a thrust force parallel to the flow which magnitude is directly related to the change in kinetic energy. The frictional drag experienced by the blade, along with its rotation, both contribute to the change in kinetic energy by imparting a torque on the flow. Thus, a balance between the thrust and torque on the rotor and the kinetic energy of the incoming flow is directly related by the forces and velocities involved in operating a wind turbine.

This concept is utilized by the axial momentum theory. The basic idea is that the rotor is replaced by a permeable actuator disc with an area equal to the rotor area. The forces on the actuator disc affect both the local velocities through the disc and the general flow field around the disc. Hence, the mass conservation law and momentum balance can describe the applied forces and the changed flow field. Since the actuator disc is one dimensional, only axial momentum is considered. For a real turbine, both axial and tangential momentum equations apply. The concept is illustrated in Figure 2.2 below.

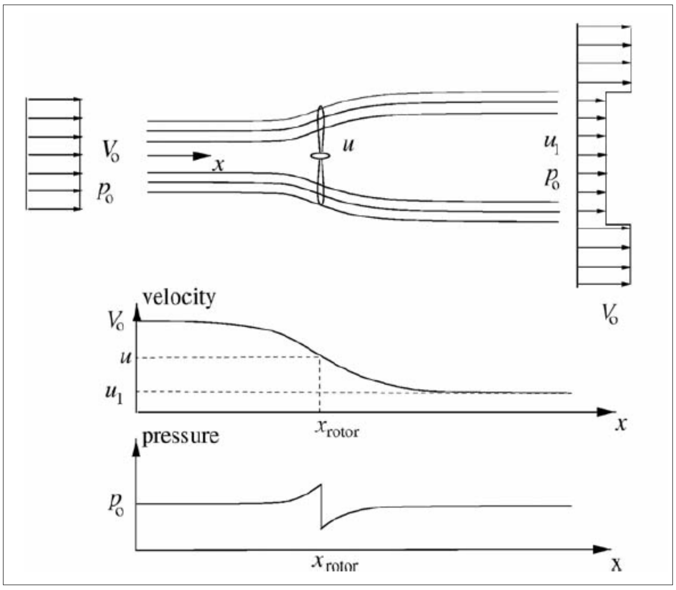

Figure 2.2: illustration of axial velocity and pressure development before and after the rotor (Hansen 2008)

As can be seen from the figure, the streamlines that pass the disc are expanding due to the reaction from the thrust. Before the axial momentum balance is applied to both sides of the disc, it is first convenient to define the axial induction factor a. This factor can be seen as the ratio of the reduction of wind speed between the velocity far upstream and the wind speed at the rotor.

$$a \equiv \frac{U_0 - u_1}{U_0} \tag{2.5}$$

By using the observations mentioned above, combined with the definition of the axial induction, one is now able to derive a relation for the power and thrust at the rotor. First, Bernoulli’s equation can be applied to the stream tube on either side of the actuator disc. Then the momentum balance is used to find a relation for the thrust, and it is substituted into the Bernoulli equation to find the following expressions for the power and thrust of the rotor.

$$T = {}^{1}\!/_{2}\, \rho A U_0^2 \cdot 4a(1-a) \tag{2.6}$$

$$P = {}^{1}\!/_{2}\, \rho A U_0^3 \cdot 4a(1-a)^2 \tag{2.7}$$

The performance of the rotor is usually evaluated by the dimensionless power coefficient C_P, it is defined as the rotor power divided by the power available in the wind.

$$C_P = \frac{P}{{}^{1}\!/_{2}\, \rho U_0^3 A} = 4a(1-a)^2 \tag{2.8}$$

The thrust coefficient C_T is defined in a similar manner:

$$C_T = \frac{P}{{}^{1}\!/_{2}\, \rho U_0^2 A} = 4a(1-a) \tag{2.9}$$

To find the maximum, the formula above is differentiated with respect to a and is set equal to zero. This yields that the theoretical maximum C_P amounts to 16/27 ≈ 0.5926 when a=1/3. This is known as the Betz limit. Note: for a>0.5, the velocity in the wake becomes negative, this violates the assumptions upon which the theory is based, and makes it invalid.

2.3. Blade element momentum theory

The disadvantage of the linear momentum theory explained in the previous section is that it does not include the actual geometry of the rotor, e.g. the number of blades, twist and chord distribution and the airfoil at each section. The BEM theory is an important add-on to actuator disc model. The model is extensively described in virtually every wind turbine related book. In this section, only the basic outcomes are presented. For a more detailed description as well as derivations of the equations, the reader is referred to books by Manwell, Burton or Hansen, for example (Manwell et al. 2002), (Burton et al. 2001) and (Hansen 2008).

It does not perform accurately in all situations and conditions, but the BEM method is especially helpful to outline the basic concepts of wind turbine aerodynamics. The BEM theory is a 2D model that combines a linear and angular momentum analysis with a force analysis performed on a small blade element. Both analyses yield relations for the thrust and the torque on a wind turbine which can be combined to obtain the distributions for both the induction factors and thrust/torque coefficients.

In the BEM method, the stream tube is expanded radially into discrete annular elements, with no radial dependency. The momentum equations can be applied to each of the segments, similar to the way described in the previous section. This yields the following relations for the torque and thrust for an element dr:

$$dT = {}^{1}\!/_{2}\, \rho U_0^2 4a(1-a) 2\pi r dr \tag{2.10}$$

$$dQ = 4\pi r^3 \rho U_0 \Omega (1-a) a' dr \tag{2.11}$$

The changes in momentum, described in the previous equations, are balanced with aerodynamic forces on the blades. For each of the radial segments, an airfoil element is found, with forces and velocities depicted in the Figure 2.3 below. The figure shows a cross-sectional airfoil element positioned on the blade at a radius *r*. the aerodynamic forces are governed by the local velocities and are determined with the use of 2D airfoil characteristics, as explained in the section 2.1.

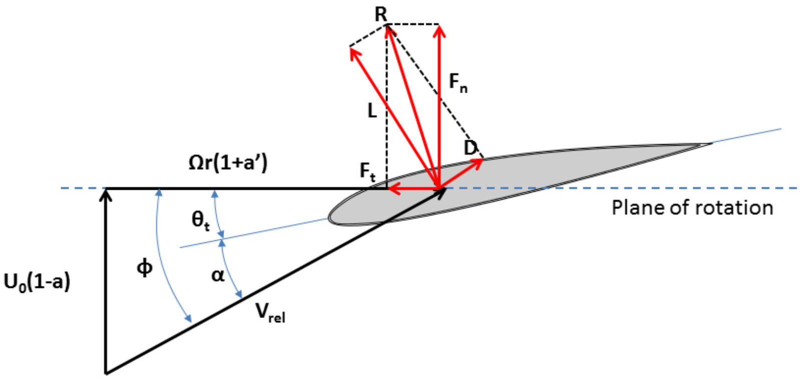

Figure 2.3: force (red) and velocity (black) vectors that act on an airfoil element

In the figure, the angles ϕ, θ_t and α represent the inflow angle, the twist angle and the angle of attack, respectively. The resulting force *R*, which constitutes of the lift *L* and drag *D*, can be decomposed in a force normal to the plane of rotation F_n and a tangential component, F_t. As shown in equations (2.2) and (2.3), the lift and drag can be computed based on their associated coefficient, which in turn are dependent on Reynolds number and angle of attack. The angle of attack is found by subtracting the twist angle from the inflow angle, which can be, by using trigonometry, expressed as follows:

$$\tan\phi = \frac{(1-\mathrm{a})\mathrm{U}_0}{(1+\mathrm{a}')\Omega\mathrm{r}} \tag{2.12}$$

Where the tangential induction factor *a'* is defined as ω/2Ω. The definition comes from the assumption that the flow at the inlet of the blade is not rotating, while at the exit the flow rotates at rotational speed ω. The flow will have gained this rotational speed as it passes the blade. Therefore, the average rotational speed over the blade is ω/2. Since the blade itself rotates with velocity Ω, the average tangential velocity of the blade is $\Omega r + {}^{1}/_{2}\,\omega r$. The tangential velocity component is now described by the relation $\Omega r(1+a')$.

Now that the inflow angle is known, equations for the thrust and torque on a blade element can be established.

$$F_n = L\cos\phi + D\sin\phi \tag{2.13}$$

$$F_t = L\sin\phi - D\cos\phi \tag{2.14}$$

The total thrust and torque on the blade is now found by integrating the contribution of each element over the entire blade. The mechanical power of the rotor is now the product of the rotational speed of the rotor Ω and the torque. From the analysis it can be concluded that a high tangential velocity is desirable in order to maximize the rotor power. Since the highest velocities occur in the outer region of the blade, this section has the largest contribution to the total power production.

2.4. Boundary layer theory

In order to understand the basic concepts of wind turbine aeroacoustics, it is important to have some background knowledge concerning airfoil viscous boundary layer theory. For some of the parameters that describe the boundary layer play a significant role in the emission *and* the prediction of aerodynamic noise. For this reason, the basics of this topic will briefly be introduced. For a more elaborate description the reader is referred to text books by White (White 1991) and Schlichting (Schlichting 1968).

The origin of the boundary layer concept is attributed to the work of Ludwig Prandtl, a professor at the University of Göttingen. The term 'boundary layer' is first introduced in his paper written in 1904. It was his idea that a body immersed in a fluid can be divided in two regions: a thin layer immediately adjacent to the surface of the body (the boundary layer) in which frictional forces play an important role, and the remaining outer region where friction forces can be neglected.

The flow inside the boundary layer is dependent on both geometric and ambient conditions. Under certain conditions the flow can become reversed and detach from the surface of the body (or airfoil). This phenomenon is accompanied by an increase in drag and a sudden drop in lift on bodies such as an airfoil and is known as boundary layer separation. It is also related to the creation of eddies in the wake of the airfoil.

2.4.1. Boundary layer basics

Prandtl's reasoning was as follows: Since the flow is assumed to behave like a frictionless and incompressible fluid, meaning no shear stresses are present between two consecutive layers. This absence of tangential forces implies that close to the surface, a difference in tangential velocity exists (slip). In real flows this is not possible, so a region must exist where, under the influence of viscosity, the fluid particles adhere to the wall. Because the flow attaches to the wall, the velocity at the surface must be zero, the *no-slip condition*. The no slip condition inside the boundary layer implies that fluid particles are being slow down due to frictional forces, creating a velocity gradient $\partial u/\partial y$. This thin layer where the flow velocity increases from zero until the free stream velocity as a result of viscosity is termed the *boundary layer*. A graphical representation of the development of the boundary layer as the flow progresses over a surface can be seen in Figure 2.4

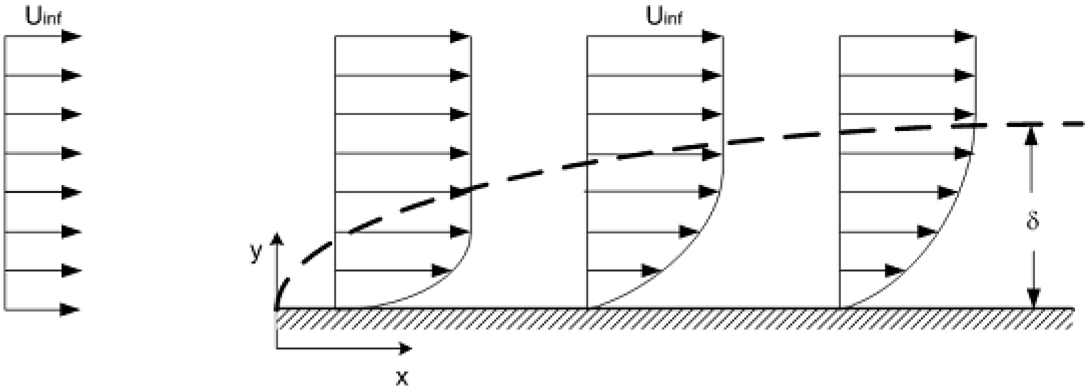

Figure 2.4: Boundary layer velocity profile over a flat plate (Chklovski 2012)

From the figure, it can be seen that the thickness of the boundary layer δ increases as the flow moves further downstream. This can be explained by the fact that as the flow progresses, an increasingly bigger region becomes affected by the frictional forces. The slower moving particles across the surface retard the particles adjacent to them which in turn affect the neighboring particles, thereby increasing the thickness of the boundary layer.

The retarded particles do not remain attached to the surface of the airfoil for the entire length of the boundary wall. In certain circumstances the flow becomes reversed and the decelerated particles are forced outwards, thus enforcing the flow to separate. This boundary layer separation is always associated with vortex generation in the wake of the body. This situation induces a large drag due to the large deviation of the pressure distribution with respect to the potential flow.

2.4.2. Laminar and turbulent boundary layers

The boundary layer can be categorized into two different regimes, a laminar one a turbulent. In laminar flow, the flow moves in different layers, or lamina, without exchange of mass between these layers. The result is that the shear developed in the velocity gradient in Figure 2.4, is entirely due to viscosity. Because the mass transfer between two layers is zero, there is no exchange in momentum as well. In turbulent flow, a significant exchange of both momentum and mass is taking place in both streamwise direction and perpendicular to the flow, because of velocity fluctuations. Due to these fluctuations the velocity profile is varying with time, therefore, a time averaged velocity profile is usually defined. The velocity profile for the laminar and the turbulent case are depicted in the figure below.

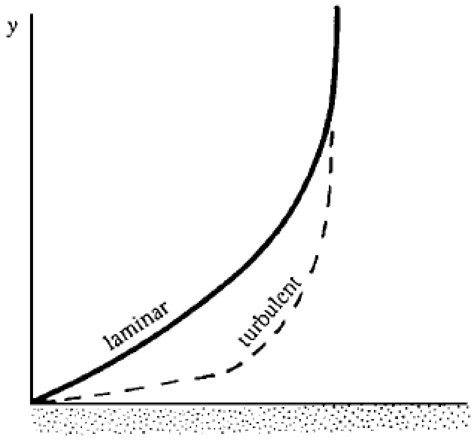

Figure 2.5: Laminar and turbulent boundary layer velocity profile (Kundu & Cohen 2008)

The figure above assumes the pressure gradient to be zero and therefore represents the velocity profile over a flat plate. For the laminar case the velocity is reduced over a significant region of the boundary layer, since viscosity is the only mechanism which affects the velocity of the neighboring particles. Because in the turbulent case a significant exchange of both mass and momentum from the free stream into the inner layer exists, a high fluid velocity close to the wall can be observed.

The boundary layer remains laminar until a point is reached where the viscous stresses are not able to cope with the developed disturbances. The disturbances may originate from various sources: surface roughness, turbulence in the free stream or vibrations of the body itself can all be sources of radial velocity fluctuations. At this transition point, the radial fluctuations in the flow become stronger, until a turbulent state is reached.

So far the flow over a flat plate has mainly been considered, where the pressure gradient of the external stream is zero. For the flow around an airfoil or any other curved surface this is not the case. The velocity distribution around a curved object is such, that the speed increases upstream of the highest point, and the velocity decreases downstream. From the Bernoulli equation it can be deduced that the pressure decreases if the velocity increases, and vice versa. This leads to negative or favorable pressure gradient ($dp/dx<0$) upstream, and a positive or adverse pressure gradient downstream of the maximum thickness point. In Figure 2.6, the development of the boundary layer in an external stream with adverse pressure gradient (so downstream of the maximum thickness point) is shown.

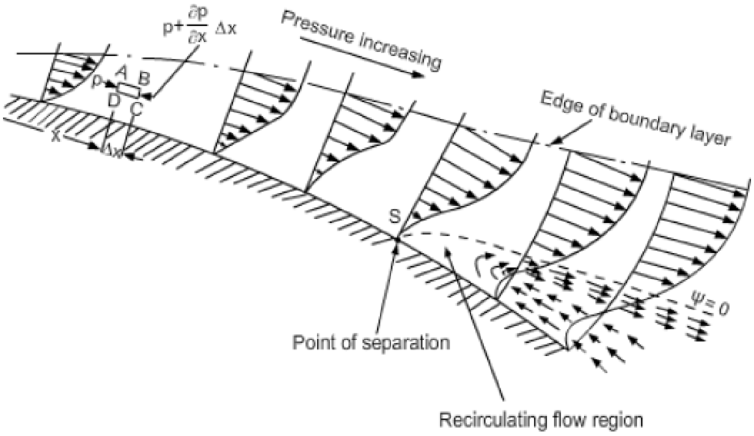

Figure 2.6: Flow in boundary layer leading to separation due to an adverse pressure gradient (Tulapurkara 2015)

The positive pressure gradient causes the flow to decelerate, in addition to the deceleration due to viscosity. Because of viscosity, this effect is more pronounced near the surface. When the flow moves further downstream, the flow continues to slow down, until a point is reached where the slope of the velocity profile at the wall, $(\partial u/\partial y)_{wall}$, becomes zero. At this inflection point, denoted as point S in the figure above, the flow direction at the wall reverses which causes the boundary layer thickness to grow rapidly. This reversed flow forces the forward moving flow outward into the mainstream, leading to flow separation. This flow separation causes the pressure drag of the body to increase significantly, because the pressure recovery that would take place in an unseparated flow, does not take place.

Because the velocity profile in a turbulent boundary layer is ‘fuller’ (Figure 2.5), e.g. the velocity gradient is steeper, a turbulent boundary layer is more capable of withstanding an adverse pressure gradient. Because of this, the separation point moves further downstream in a turbulent flow compared to a laminar one.

2.4.3. Quantities that define the boundary layer

In addition to the boundary layer thickness itself, which is usually somewhat arbitrarily defined as 99% of the free stream velocity (but other definitions are used as well), more parameters exist to describe the boundary layer more thoroughly. Each of the definitions provides different information regarding its characteristics. As will become clear in chapter 6, these parameters play a role in the prediction of aerodynamic noise of a wind turbine.

2.4.3.1. *Displacement thickness*

This quantity is a measure for the missing mass flow as a result of the presence of the boundary layer. The mass flow within a streamtube approaching the body (inviscid case) has a value of $\rho_e U_e$. Due to the existence of the boundary layer (viscous case), this value is decreased to a value ρu. Because of mass conservation, the cross section of the streamtube must increase. For a 2D situation the consequence is therefore that the width of the streamtube within the boundary layer will increase thus displacing the streamlines of the free flow outward. The displacement thickness δ^* is now the distance by which the free stream is displaced as a result of the presence of the boundary layer. This definition is illustrated in the picture below.

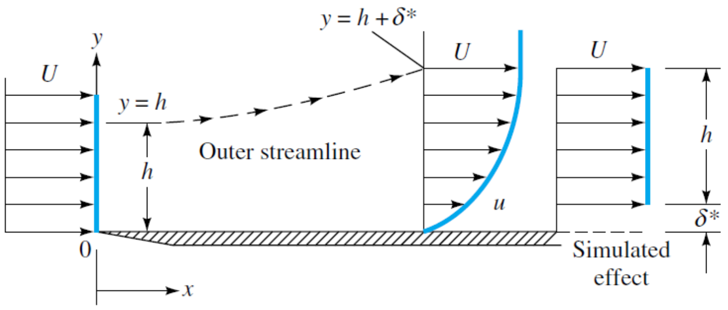

Figure 2.7: Definition of the displacement thickness (White 2009)

This can mathematically be written as:

$$\delta^* = \int_0^\infty (\rho_e U_e - \rho u) dy \tag{2.15}$$

Assuming the density remains constant and rearranging terms one finds:

$$\delta^* = \int_0^\delta (1 - \frac{u}{U_e}) dy \tag{2.16}$$

2.4.3.2. *Momentum loss thickness*

The momentum thickness is, analogue to the definition of the displacement thickness, related to the missing momentum flow as a result of the presence of the boundary layer. Because of the existence of the boundary layer, the momentum flow rate is less due to a reduction of the velocity near the wall. The momentum thickness ϑ is now defined as the distance the surface has to be displaced for the momentum flow in the inviscid case to be equal with the flow of momentum for the viscous case. Again, assuming the densities inside and outside of the boundary layer to be equal, the momentum thickness can be expressed the following way:

Inviscid case momentum flow:

$$U_e \int_0^\infty (\rho u) dy \tag{2.17}$$

For the viscous case:

$$\int_0^\infty (\rho u^2) dy \tag{2.18}$$

Expressing the missing momentum flow as the product of $\rho_e U_e^2$ and the distance ϑ, leads to:

$$\rho_e U_e^2 \theta = \int_0^\infty \rho u (U_e - u) dy \tag{2.19}$$

$$\theta = \int_0^\infty \frac{u}{U_e} (1 - \frac{u}{U_e}) dy \tag{2.20}$$

2.4.3.3. *Skin friction coefficient*

Another quantity that one stumbles upon in literature in the modelling of aerodynamic wind turbine noise is the skin friction coefficient. It is defined as, similarly to the lift and drag coefficient outlined in section 2.1, a ratio between the friction force exerted on the surface and the dynamic pressure. This friction force per unit area is depicted as the wall shear stress; it is defined by the relation:

$$\tau_w = \mu \frac{\partial u}{\partial y}\bigg|_{y=0} \tag{2.21}$$

Incorporating the wall shear stress rather than the friction force leads to:

$$C_f \equiv \frac{\tau_w}{\frac{1}{2}\rho u^2} \tag{2.22}$$

3. Basics of sound

In this section, the basics of acoustics will be outlined, to provide the reader with the bare essentials related to sound. The first sections elude on the basic phenomena that play a role in general acoustics. Then the difference is established between emitted and received and how they are defined. The section that follows touches upon how this sound is perceived by humans and finally the influence of the position of the observer and the source is explained.

3.1. Principles of acoustics

Sound is an oscillation of pressure waves propagating through medium as sound waves. It can be generated by various different mediums. The sound waves are characterized by its wavelength λ, frequency f and velocity c_0 (which in the case of air is equal to 340 m/s, at standard conditions). Before reaching the eardrum of the observer, the sound can be propagated in various ways. It can be reflected, refracted of attenuated by a medium. Whether a sound is perceptible to humans depends on the amplitude and frequency. If the sound is considered unwanted by the receiver, sound may turn in to noise. This depends both on measureable quantities, such as level and duration of a sound, and subjective factors, e.g. sensitivity of the listener and the situation. For example, a dripping faucet produces a relatively low sound level but it can make it impossible for people to sleep. On the other hand, many people can sleep in a car or an airplane, even when they produce sound levels that are significantly higher.

3.2. Sound pressure and power level

The response of the human ear to the amplitude of sound pressure is not linear. When the amplitude of the pressure is doubled, it is not perceived by humans as twice as high. This is because the response of the human hearing system can be approximated by a logarithmic scale. The definition of the sound pressure level L_p, expressed in decibel (dB), is

$$L_p = 10\log_{10}\left(\frac{p_{rms}^2}{p_{ref}^2}\right) = 20\log_{10}\left(\frac{p_{rms}}{p_{ref}}\right) \tag{3.1}$$

Where p_{ref} is a reference pressure and has the value of $2 \cdot 10^{-5}$ Pa (in normal air), which is the threshold for human hearing at a frequency of 1 kHz, the weakest audible sound. P_{rms} is the root mean square sound pressure and is defined by

$$p_{rms}^2 = \lim_{T\to\infty}\left(\frac{1}{T}\int_0^T p^2(t)dt\right) \tag{3.2}$$

According to this definition, doubling the sound pressure of the source will result in an increase of 3 dB (because $10 \cdot \log_{10} 2 \approx 3\ dB$), when the amplitude is increased by a factor of 10, the difference will be 20 dB.

As in the case of electromagnetic waves, sound waves transport energy from a source of sound through a medium. The sound intensity I is defined as the energy transmitted per unit time and unit area, in other words the power per unit area, the unit thus being W/m^2. It can be calculated as follows

$$I = \frac{p_{rms}^2}{\rho_0 c_0} \tag{3.3}$$

So the intensity is simply the mean square sound pressure divided by the speed of sound and the density of the medium. For air at standard conditions $\rho_0 c_0$ amounts to 416 kg/m^{2}s. With this formula, it is now possible to express the sound pressure level L_p as the ratio of the intensity and a reference intensity

$$L_p = 10\log_{10}\left(\frac{p_{rms}^2}{p_{ref}^2}\right) = 10\log_{10}\left(\frac{I}{I_{ref}}\right) \tag{3.4}$$

where $I_{ref} = p_{rms}^2/\rho_0 c_0$ and has a value of 10^{-12} W/m^2. Both sound intensity and sound pressure level are dependent on the position of the observer. The greater the distance between the sound object and the observer, the smaller these parameters will be. The total strength emitted by a source of sound is characterized by the sound power. The sound power transmitted through a surface S is the integral over the intensity I over S. This yields

$$P = \int_S I dS = \int_S \frac{p_{rms}^2}{\rho c} dS \tag{3.5}$$

If the surface S encloses the source of sound, P is the total sound power emitted by the source. Now, analogously to the definition of the sound pressure level, one can define the sound power level L_W as follows

$$L_W = 10\log_{10}\left(\frac{P}{Pref}\right) \tag{3.6}$$

Where $P_{ref} = 10^{-12}$W is the reference sound power, the lowest detectable sound power of the human eardrum. The sound power level is again measured in dB. The intensity and sound pressure decrease as the distance is increased. In a free field, where viscous damping is neglected, they decrease with the inverse square of the distance R. This law of spherical spreading is illustrated in Figure 3.1 below.

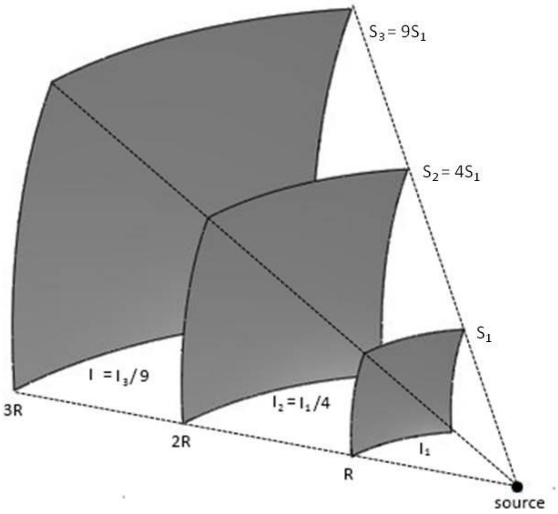

Figure 3.1: Law of spherical spreading

The power emitted by the source P_s is equal to the intensity multiplied by the surface area. This power is transmitted through all three surfaces S_1, S_2 and S_3, and each consecutive surface area decreases with the square of the radius. If the intensity remains the same the following is obtained

$$I = \frac{P_S}{4\pi R^2} \tag{3.1}$$

The difference between sound *pressure* level and sound *power* level must be understood very clearly. The sound power level L_W is the acoustic power emitted by the source. The sound pressure level is a property of sound that is received at the location of the observer. The sound pressure level is dependent on the direction and distance of the observer relative to the sound, thus the determination of L_W requires combined measurements of L_P at several locations around the source. Furthermore, emission refers to the sound emitted by the source and is thus related to the sound power level. Whereas immission is also a property of the observer position is characterized by the sound pressure level Lp.

3.3. Sound frequency spectrum

In order to characterize the sound, it is necessary to determine its frequency spectrum. Not only the amplitude of the emitted sound is important, its frequency is as well. To analyze a sound source, the frequency spectrum of the sound source has to be determined. The frequency spectrum indicated which frequencies are prevalent in the sound pressure signal, showing whether there are tonal components or a broadband swishing. As will be seen later on, the different noise mechanisms will have different frequencies dominating in the spectrum.

The frequency spectrum can be divided into several bands, either narrowband or broadband. The ones that are most commonly used are the narrow bands, 1/3 octave bands and 1/1 octave bands. In the narrow-band representation each frequency has the same Δf. This spectrum gives the most detailed picture of the sound signal.

The terms 1/1 octave bands and 1/3 octave bands describe the frequency band according to the ratio of the upper and lower frequencies that bound the band. In a 1/1-octave band, the upper bounding frequency is twice the lower. In a 1/3-octave band, the lower frequency has to be multiplied by $\sqrt[3]{2}$ to obtain the upper bounding frequency.

The human ear does not respond equally to the tones at various frequencies. For some frequencies the ear is more sensitive than for others. At the frequencies where the maximum response occurs (between 3000 and 4000 Hz), the threshold for hearing is somewhat less than 0 dB, while a 100 Hz tone must have a frequency of at least 20 dB to be heard. In order to account for this, several weighting systems have been introduced (A-, B- and C-weighting) to de-emphasize the lower frequencies in a manner similar to human hearing.

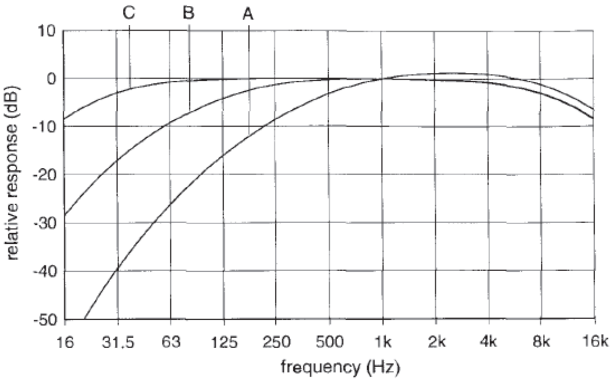

Figure 3.2: A, B, and C-weighting (Wagner et al. 1996)

The most commonly used acoustic weighting filter is the A-weighting because of its response at not the lower frequencies. B- and C-weighting is applied when strong low-frequent sound levels occur. Since the noise radiated from wind turbines is predominantly medium/high frequent, the A-weighting filter is applied.

3.4. Directivity

Directivity is a phenomenon that determines the reduction of the sound pressure level depending on the location of the observer relative to the source. The sound emitted from a source can be omni- or directional according to Vargas (Vargas 2008).

If a source of sound is omni-directional it means that the sound emitted is radiated equally in all directions. When it is directional, the strength of the noise level may vary in different directions from the sound source. If the source radiates predominantly in two directions, it is called bipolar, when it radiated in four directions, quadrupolar, etc. This can be graphically represented by the radiation pattern, see Figure 3.3.

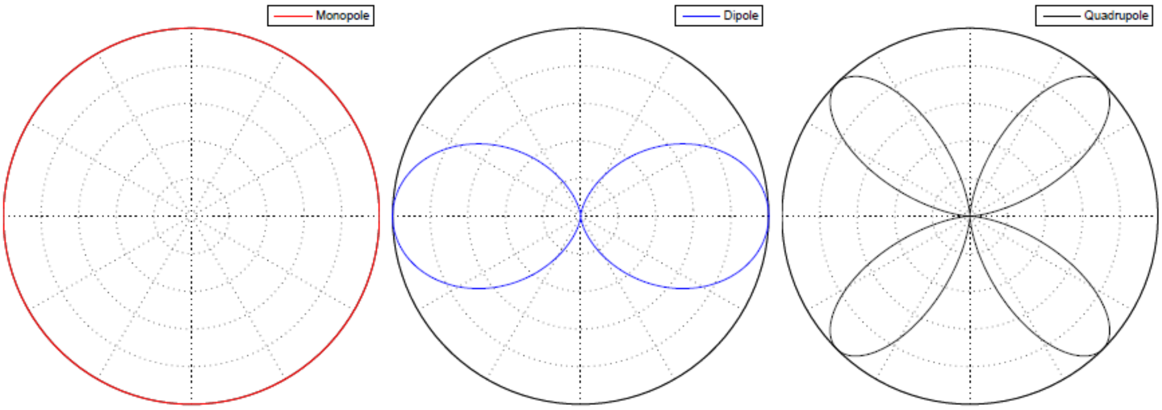

Figure 3.3 Radiation pattern of a monopole (L), dipole (M) and a quadrupole (R) (Gasch 2014)

Each of the various noise mechanisms explained in the next chapter can have a different radiation pattern, this is explained in further detail in section 4.2.1.

4. Airfoil aero-acoustics

The sound from a wind turbine can be categorized into mechanical noise and aerodynamic noise. Mechanical noise is generated in components in the hub of the turbine such as the gearbox, generator and cooling fans. The aerodynamic noise is radiated from the blades and is mainly associated with the interaction of turbulence and the flow with the blade surface. The turbulence can originate either from the incoming natural turbulence present in the wind, of from the viscous flow in the boundary layer around the blades.

In contrast to aerodynamic noise, mechanical noise can be reduced significantly provided it is adequately treated. It also does not increase with dimensions as rapidly as aerodynamic noise, so the aerodynamic noise dominates as the size of the turbine increases. Aerodynamic noise sources can be divided into three main components, namely: low-frequency noise, inflow turbulence noise, and airfoil self-noise (Oerlemans 2011). First a brief overview of the noise mechanisms that play a role will be outlined shortly.

4.1. Airfoil noise mechanisms

4.1.1. Low frequency noise

During operation of the turbine, the blades encounter localized flow deficiencies which are caused by the presence of the tower. Often wind turbines have a tower with a cylindrical cross section which forces the air to move around it, thereby modifying both the flow upstream and downstream. This can be visualized as the flow of air around a cylinder: the air upstream is decelerated whereas the airflow downstream cannot follow the curvature of the cylinder and separates.

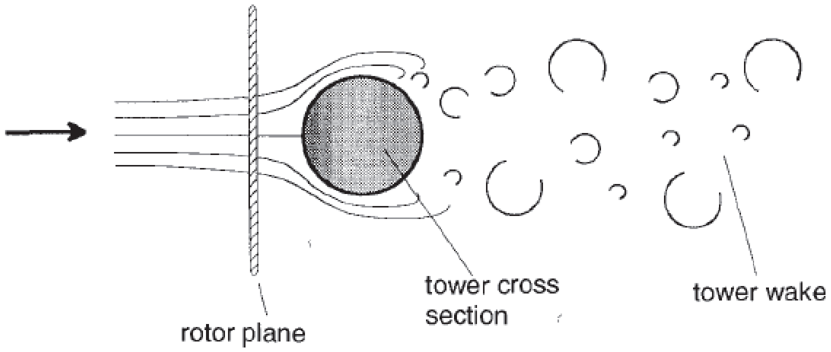

Figure 4.1: Typical flow around a cylindrical wind turbine tower in upwind configuration (Wagner et al. 1996)

The blades (either located upwind or downwind) encountering the flow field of the tower exhibit a change in angle of attack as well as a pressure change resulting in a change in blade loading. The fluctuation in blade loading is directly related to the emission of noise according to the Ffowcs Williams-Hawking[1] (FW-H) equation. Since this noise mechanism is directly related to the passing frequency of the blades, the noise spectrum is dominated by this frequency, typically in the order of 1-3 Hz (thus the term ‘low frequency noise’).

---

[1] The FW-H extended Lighthill’s formulation, by applying the same analogy on a domain split in two parts; the surrounding flow and the moving surfaces. It couples the acoustic radiation of an arbitrary moving surface within the flow in which it is immersed.

However, since the rotor is almost always placed upwind of the tower, the effect of this noise mechanism is reduced considerably (Kim et al. 2010). Furthermore, since the dominant frequency range in the spectrum is below the audible hearing range of humans, this low frequency noise is of minor importance. Low frequency noise can, however, excite vibration of building structures such as windows, walls and floors (Wagner et al. 1996).

4.1.2. Inflow-turbulence noise

When the atmospheric turbulence encounters buildings or some other solid structures, it will generate noise which is the so-called turbulent inflow noise. The broadband noise generated by this noise mechanism is mainly driven by the characteristics and properties of the turbulence. Therefore the properties of turbulence will be explained briefly (Zhu 2004).

This turbulence is created due to both aerodynamic and thermal effects. The aerodynamic effect is mainly due to wind shear, thus the viscous interaction of the flow with the surface. The thermal turbulence is generated by the buoyancy of the air caused by local heating differences by the sun. Each component is driven by a different mechanism; the longitudinal component is mainly driven by wind shear whereas the vertical component is driven by both mechanisms.

Inflow turbulence noise can be subdivided into low frequency and high frequency noise, depending on the size of the eddy compared to the chord of the blade. The scale of these eddies is dependent on the type of turbulence, the frequency and the corresponding wavelength. As can be seen in Figure 4.2 below.

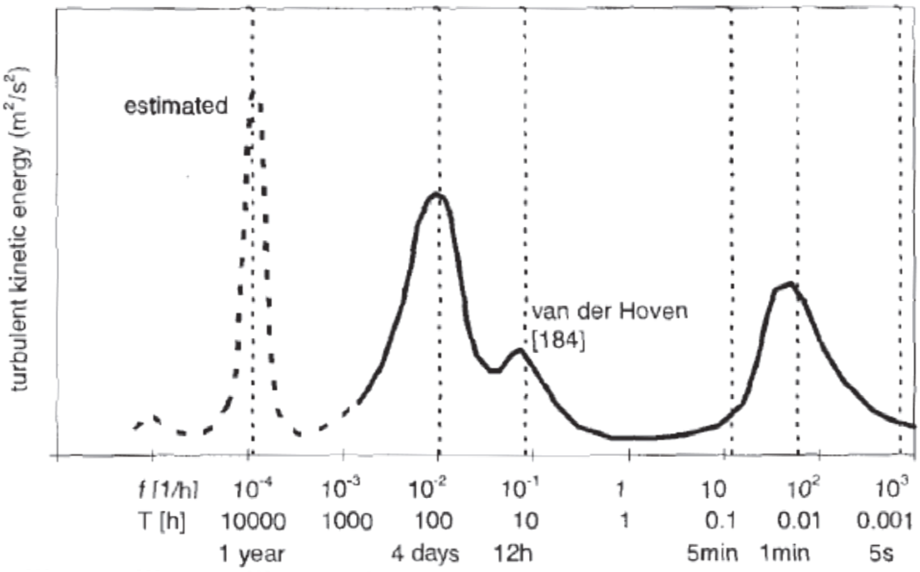

Figure 4.2: Turbulent kinetic energy spectrum of the horizontal wind speed (Wagner et al. 1996)

In this figure, each peak corresponds to a typical time scale of occurrence of a type of turbulence. The first maximum represents the annual seasonal change. The second maximum occurs at 4 days, the typical period for a change in the global weather. The third peak at 12 hours is due to the change between day and night and the corresponding temperature changes. The final peak around 1-2 minutes is part of the real gust spectrum. The typical size for the turbulent eddies is given in the Table 4.1 below.

Table 4.1: Typical size of turbulent eddies (Wagner et al. 1996)

Frequency [hz]	10	100	500	2000
Wavelength [m]	34.0	3.4	0.68	0.17
Eddy size [m]	8.5	0.85	0.17	0.04
Eddy size/chord length [%]	850.0	85.0	17.0	4.25

As stated, the two regimes are categorized in low frequency and high frequency inflow turbulence noise. If the size of an eddy (Λ) is much larger than the blade chord, the total blade load will be affected and the total blade will respond. This will cause noise radiation of dipole character, varying with M^6. The frequency of this noise will approximately be $f = U/\Lambda$, where U denotes the local flow velocity.

High frequency turbulence noise occurs when the size of an eddy is comparable or much less than the dimensions of the blade. This eddy will then induce local pressure variations rather than influence the whole blade loading. This results in a radiation of noise of a higher frequency. Below a figure can be found which explains this phenomenon in a graphical way.

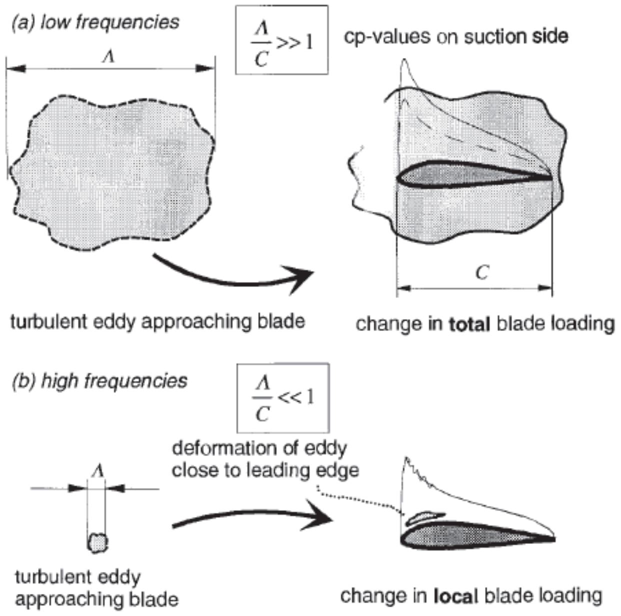

Figure 4.3: Size of the turbulent eddies and blade loading (Wagner et al. 1996)

Inflow turbulence noise is not yet fully understood and is estimated to be a major source of aerodynamic noise in the frequency range up to 1000 Hz. It is often perceived by observers as a swishing noise.

4.1.3. Airfoil self-noise mechanisms

The previous two noise mechanisms involved either the presence of turbulence or unsteady airflow, which induced vibrations and in that way radiated noise. Even the case of perfectly steady and turbulence an airfoil still radiates noise in case instabilities in the boundary layer occur or due to interaction of eddies in the boundary layer with the airfoil surface. In the report of Brooks, Pope and Marcolini (Brooks et al. 1989), they distinguished five mechanisms that generate this so-called self-noise. In this section the mechanisms will be outlined and evaluated.

1. Turbulent-boundary-layer – trailing-edge noise
2. Laminar-boundary-layer – vortex-shedding noise
3. Separation-stall noise
4. Trailing-edge-bluntness – vortex-shedding noise
5. Tip vortex formation noise

4.1.3.1. *Turbulent boundary layer – trailing edge noise*

As the wind progresses from the leading to the trailing edge, a boundary layer develops on the blade surface. The transition from a laminar to a turbulent boundary layer occurs at a certain chord wise position, depending on the profile shape, angle of attack, Reynolds number, etc. The most important parameter concerning the boundary layer is the normal coordinate. Beneath the boundary layer, the turbulence induces a fluctuating pressure field. Certain properties of this boundary layer can be used to compute trailing edge noise. Particularly the boundary layer displacement thickness is often used.

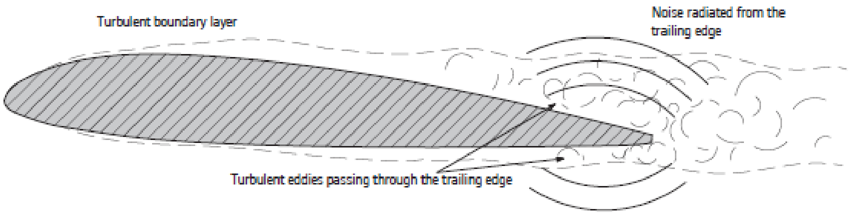

Figure 4.4: Principle mechanism of trailing edge noise (Gasch 2014)

At low Mach numbers, turbulent eddies are not very efficient sound sources. However, when they arrive at a discontinuity, e.g. the trailing edge, the will become more efficient. This is the principle mechanism of the turbulent boundary layer – trailing edge noise. It seems the noise is dependent on the angle between the turbulent eddies and the trailing edge. This implies that the noise level can be reduced by giving the wing a swept shape. Another suggestion to lower the noise is to give the trailing edge a serrated shape (Howe 1991). The noise is often perceived as a swishing sound. The peak frequency is typically in the order of 500-1500 Hz, depending on the turbine type and operation. It is generally considered to be the most dominant noise source for large wind turbines.

4.1.3.2. *Laminar boundary layer – Vortex shedding noise*

At various blade radii of a blade, different Reynolds numbers may occur, due to changes of relative wind speed and different chord lengths. When a section operates at a Reynolds number between 10^5 and 10^6, the following is likely to occur. A laminar boundary layer exists on one or both sides of the airfoil and might cover most of the airfoil surface, a resonant interaction between the unsteady laminar-turbulent transition with the trailing edge noise, described in the previous paragraph, will occur (Zhu 2004).

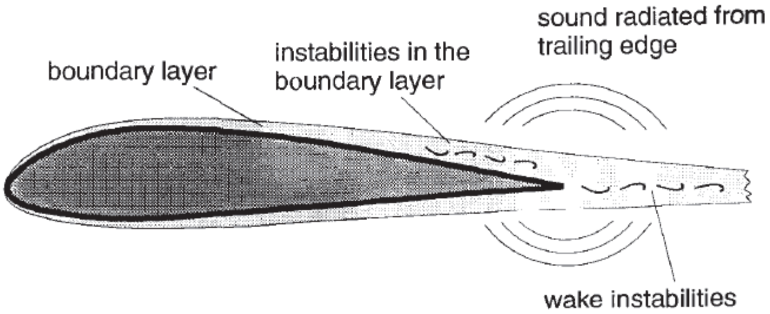

Figure 4.5: Laminar boundary layer – vortex shedding noise (Wagner et al. 1996)

However, since most modern wind turbines operate at much higher Reynolds numbers, laminar-boundary layer vortex shedding noise is of lesser importance. Only for the medium-sized wind turbines this is expected to produce a significant contribution. It then produces a tonal noise which then often dominates the sound pressure level at the high frequency spectrum. If this noise does turn out to be a problem, a possible solution may be tripping of the boundary layer. The transition point of the boundary layer is now brought farther upstream of the trailing edge, thereby preventing the resonant interaction.

4.1.3.3. *Tip vortex formation noise*

At the tip, the pressure difference between the suction and pressure side of the blade result in a cross flow over the side edge of the tip which results in the formation of a tip vortex. Brooks, Pope and Marcolini suggest that this tip vortex interacts with the trailing vortex in the same manner as the boundary layer turbulence does for trailing edge noise (Brooks et al. 1989). The tip vortex noise is estimated to possibly produce an extra 1-2 dB of noise in some parts of the frequency range. It is also dependent on the shape of the blade tip. Therefore a reduction of this tip noise is mainly focused on the proper design of the shape of the tip.

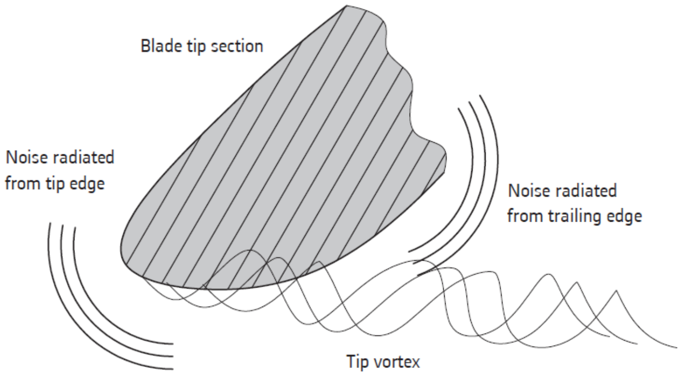

Figure 4.6: Sketch of Turbulent boundary layer – tip vortex formation noise (Gasch 2014)

4.1.3.4. *Separation-stall noise*

For high angles of attack, stall conditions occur resulting in unsteady flow around the airfoil. These turbulent eddies from the separated flow radiate substantial levels of noise. Fink and Bailey found an increase of more than 10 dB for stalled flow compared to trailing edge noise for low angles of attack (Fink & Bailey 1980). It was also found that mildly separated flow, for moderate angles of attack, causes sound radiation from the chord as a whole. Beyond a certain angle of attack, separation stall noise is the only major contributing noise mechanism. It can only be limited by avoiding stall conditions. For modern day wind turbines, this is achieved by pitching the blade. This noise source will therefore not be taken into account in the design process.

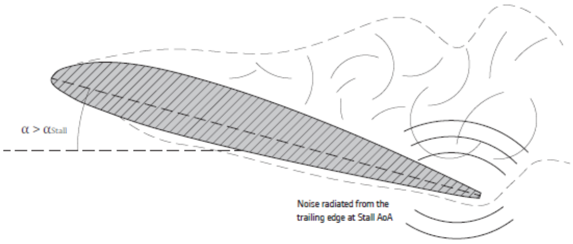

Figure 4.7: Separation-Stall noise (Gasch 2014)

4.1.3.5. *Trailing-edge-bluntness - vortex-shedding noise*

The final mechanism of airfoil self-noise is vortex shedding noise. At certain conditions, depending on the bluntness and shape of the airfoil and the Reynolds number, vortex shedding can occur in the form of a von Karman type vortex street. When this happens, an asymmetrical flow pattern forms around the airfoil and changes the pressure distribution. The alternating vortices in the near wake produce higher surface pressure fluctuations close to the trailing edge, causing it to vibrate.

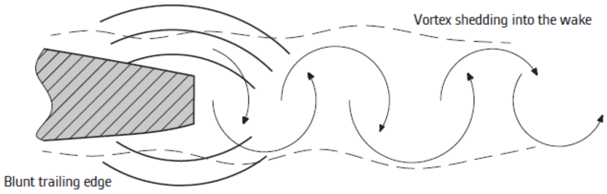

Figure 4.8: Trailing edge bluntness - Vortex Shedding noise (Zhu 2004)

The most important parameter is the t*/δ* (trailing edge thickness over boundary layer thickness) ratio, as it increases, the band width of the noise decreases resulting in noise of tonal nature. This tonal character results in a sharp hump shape in the frequency spectrum. The peak frequency depends on a number of factors, i.e. the shape of the trailing edge, the Reynolds number, and the bluntness parameter (δ*/ t*).

The paper by Blake suggests that the lower the trailing-edge thickness, the higher the peak shedding frequency (Blake 1988). So sharpening the trailing edge will result in a shift of the peak towards the ultrasound region. Blake also states that vortex streets are not generated when the bluntness ratio remains smaller than 0.05-0.3. If the bluntness parameter is larger than 0.3, tones are generated and the geometry is the driving parameter.

4.2. Sound propagation

As mentioned earlier in the report, the sound level received by an observer is not equal to the sound emitted by the source. In between, it is subject to the influence of several factors, which can either have an amplifying or attenuating effect. Aspects such as position and distance both play a role in the received sound level. The most important phenomenon related to the sound propagation of an airfoil is directivity, a topic which is briefly mentioned in section 3.4. Now that the main noise mechanisms of an airfoil have been introduced, the effects of directivity can be outlined more thoroughly in this section.

4.2.1. Directivity

Directivity was introduced as the effectiveness of the sound radiation in each direction. Directivity is source type dependent; this means that every noise source has its own directivity pattern. Which directivity pattern is applicable to which noise source, depends on the acoustic wavelength. If the wavelengths produced are much shorter than the chord length, the noise emission behaves as a baffled dipole. If the wavelengths are comparable, the noise emission follows a pure dipole. These directivity patterns are denoted as D_h and D_l for high and low frequency patterns, respectively.

The equations describing both the 'baffled'-dipole and the pure-dipole were presented in the works of BPM (Brooks et al. 1989). They are based upon the analytical expressions derived by Amiet (Amiet 1976) for the directivity of trailing edge noise from a flat plate of arbitrary chord. These equations are as follows:

$$\overline{D}_h = \frac{2\sin^2\left(\frac{\theta_r}{2}\right)\sin^2\varphi_r}{(1+M\cos\theta_r\,)[1+(M-M_c\cos\theta_r)]^2} \tag{4.1}$$

$$\overline{D}_l = \frac{\sin^2(\theta_r)\sin^2\varphi_r}{(1+M\cos\theta_r\,)^4} \tag{4.2}$$

In formula (4.1), M_c is the convection Mach number; it is based on the convection velocity of the turbulence present in the boundary layer with respect to the surface of the airfoil. Furthermore, θ_r is the angle between the blade flow velocity and the source-observer line; φ_r is the angle between the plane of the blade and the plane containing the chord line and the observer. The overbar in both equations indicate that it is normalized by the trailing edge noise radiated in the θ_r=90°, φ_r=90° direction, so $\overline{D}_h(90°,90°)=1$. These angles are defined in the retarded coordinate system, graphically represented in the illustration below.

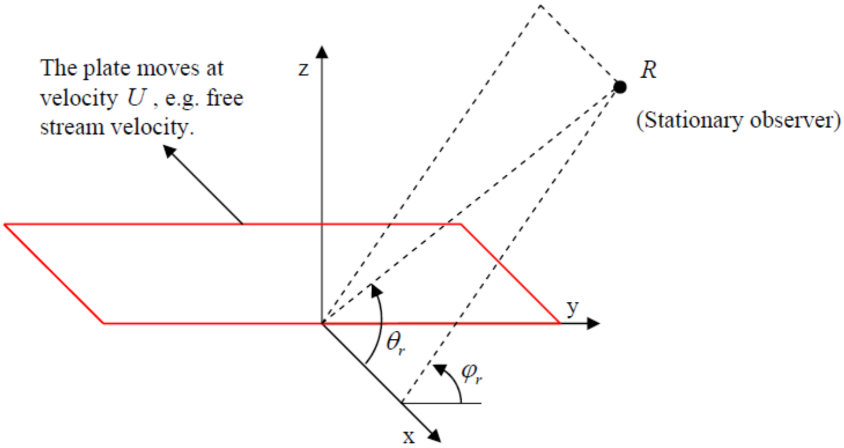

Figure 4.9: Local coordinate system of a flat plate in motion (Errasquin 2009)

This coordinate system represents a case where the source of the noise is located at the trailing edge of a thin plate, or in this case an airfoil. The plate is in motion with velocity U in the direction of the negative x-axis and the observer is located at a stationary position R. Although being developed for when the velocity U is parallel to the plate along the x-axis, the expressions can also be applied when the airfoil is at an angle of attack α. This is because the angles should be defined with respect to a coordinate system with the x-axis attached to the chord line, rather than the direction of motion. The figures below show the patterns that are created by the expressions presented earlier.

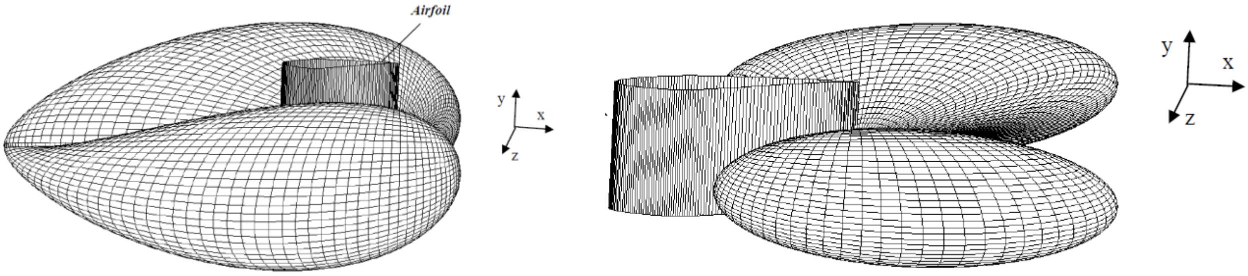

Figure 4.10: Directivity function representation for high (L) and low (R) frequency noise (Errasquin 2009)

5. Wind turbine noise on a rotor scale

In the previous chapters the mechanisms that generate aerodynamic noise have been explained. This chapter will now focus on establishing which noise mechanisms should be focused on in order to reduce the total aerodynamic noise emission. This is done by first gaining insight into the influence of each of the noise mechanisms on a rotor level.

The tool that will be used for this analysis is the noise prediction program SILANT. In the first paragraph, some background information will be given regarding the tool as well as a short introduction as to how to use it. The focus will then be on preparing the necessary data for the proper utilization of the tool. For the data preparation, it is necessary to elaborate on the aerodynamic model that is used to do this. In the section that follows the noise mechanisms that are incorporated will be outlined and what models are used to predict them. A short elaboration will be given on the sound propagation influences that are taken into account, and which models are used for them. Once the background and assumptions are covered, it will be pointed out how the tool is utilized. Finally, the tool is validated against measurements, in order to determine whether it is accurate enough to draw valid conclusions from it, which is done in the final part of the chapter.

5.1. Acoustic prediction tool SILANT

SILANT originated in 1996 from a Dutch consortium consisting of Stork Product Engineering BV, the Netherlands Organization for Applied Scientific Research (TNO) and the Dutch Aerospace Laboratory (NLR). The model was first designed to calculate noise emission of wind turbines, based on trailing-edge noise and inflow noise, which are considered to be the most important sources. Later, ECN became the manager of the tool and several improvements were made, in cooperation with NLR. These improvements include the addition of models for the prediction of tip noise and sound propagation effects (Boorsma & Schepers 2011).

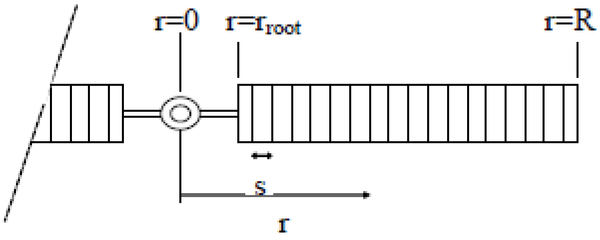

Figure 5.1: Division of rotor blades into segments (Boorsma & Schepers 2011)

The acoustic prediction tool SILANT is an executable file that works as follows. First the rotor blades are divided into *n* segments, as can be seen in Figure 5.1. The blade may be divided into a maximum of 50 elements, however usually a number of 10 to 20 elements are used. The tool requires an input file that contains all the necessary data for the acoustic analysis. This includes environmental/terrain data, rotor and blade geometry, spanwise angle of attack and velocity distributions for each element as well as some general settings such as which noise models to include. Appendix A depicts an example of such an input file. As can be seen, the file also contains information on which airfoil is located at which spanwise position. Furthermore, the SILANT folder should also contain information regarding these airfoils. This includes the profile coordinates of each airfoil as well as a boundary layer displacement thickness database. This database comprises of the boundary layer data at multiple angles of attack and various Reynolds numbers, an example of such a file is shown in Appendix B.

The database is created by using the RFOIL tool that is accompanied in the package. The boundary layer displacement thickness data that are generated by RFOIL are then rearranged into the format required for SILANT. The angle of attack and relative velocity distributions along the blade are supplied from a BEM (Blade Element Momentum) aerodynamic code, as suggested by Boorsma (Boorsma & Bulder 2010). The next section will further elaborate on the corrections and additions to the BEM model that is used.

For each of the elements, the trailing-edge and inflow noise are calculated by SILANT. For the tip element, the tip noise is added to the total. The noise generated by a segment *i* on the blade can then be calculated as follows:

$$L_{p,total}^{i} = 10\log_{10}\left(10^{(Lp)_{TBL-TE}/10} + 10^{(Lp)_{inflow}/10}\right) \tag{5.1}$$

To determine the noise generated by the entire blade, the noise radiated by each element is acoustically summed by this equation:

$$L_{p,total} = 10\log_{10}\sum_{i=1}^{n} 10^{(Lp)_{total}^{i}/10} \tag{5.2}$$

5.2. Aerodynamic model & corrections

For the computation of the relative velocity and AoA distribution of the blade a BEM model is used. The basic theory of this model is explained in section 2.3; this paragraph will touch upon the corrections that are applied to the theory in order to increase its accuracy. First, the tip/hub loss model will be described, followed by a correction when the induction factor exceeds 0.5 and the BEM model would become invalid. Then a correction to account for radial influences on the blade is outlined. Finally a method to extrapolate the aerodynamic polar generated by RFOIL is explained.

5.2.1. Tip/hub loss model

To take into account the difference between the physics of an actuator disc with infinitely many blades and an actual wind turbine or propeller with a finite number of blades, Prandtl introduced the concept of tip loss. In order to make BEM computations more realistic, Glauert showed how the tip loss effect is integrated in a simple manner into the BEM model. He corrected the induced velocity in the momentum equations by exploiting that the ratio between the average induced velocity and the induced velocity at the blade position tends to zero by the expression developed by Prandtl (Shen et al. 2005). Several root/tip corrections were developed over the years. The Prandtl-Glauert tip loss factor is given by the expressions:

$$F = \frac{\pi}{2}\cos^{-1}(\exp(-f)) \tag{5.3}$$

Where f can be either the tip or the hub loss factor.

$$f_{hub} = \frac{B(r - R_{hub})}{2r\sin\phi} \tag{5.4}$$

$$f_{tip} = \frac{B(R - r)}{2r\sin\phi} \tag{5.5}$$

$$F = F_{tip} \cdot F_{hub} \tag{5.6}$$

In the equations, B is the number of blades, r the local radius, R_{hub} the hub radius and R the blade radius. The inflow angle is represented by the parameter ϕ.

5.2.2. Glauert/Buhl correction

One of the limitations of the momentum theory is that it is no longer valid for a ≥ 0.5. In fact, the theory already starts to become invalid for induction factors of 0.4 and above. When wind turbines operate at high tip speed ratios (e.g. constant speed turbine at low speeds), the rotor enters the so-called *turbulent wake state* (a>0.5). According to momentum theory, this operating state would occur when some of the air flow in the far wake would start to propagate back upstream, which contradicts with the assumption upon which the BEM theory is based. This flow reversal is physically not possible and what happens is that flow from outside the wake starts to enter, thereby increasing the turbulence. The flow behind the rotor slows down, but the thrust on the rotor disc continues to increase. Based on experimental measurements of helicopters with large induced velocities, an empirical relationship was found by Glauert (Glauert 1926) to compensate for this effect, by applying a correction to the thrust coefficient. This relationship is also applicable to individual blade elements, not exclusively for whole rotors. Because the tip/hub loss model and the Glauert correction are strongly intertwined in certain parts of the blade, Buhl (Buhl 2005) derived a modification to this relationship that includes these corrections.

To derive the Buhl equations, the equation for thrust as a function of axial induction and the tip loss factor was used as a starting point:

$$C_T = 4aF(1-a) \tag{5.7}$$

However, as can be seen in Figure 5.2, for tip loss factors below 1, the momentum curve shifts downward and introduces a gap with the Glauert correction.

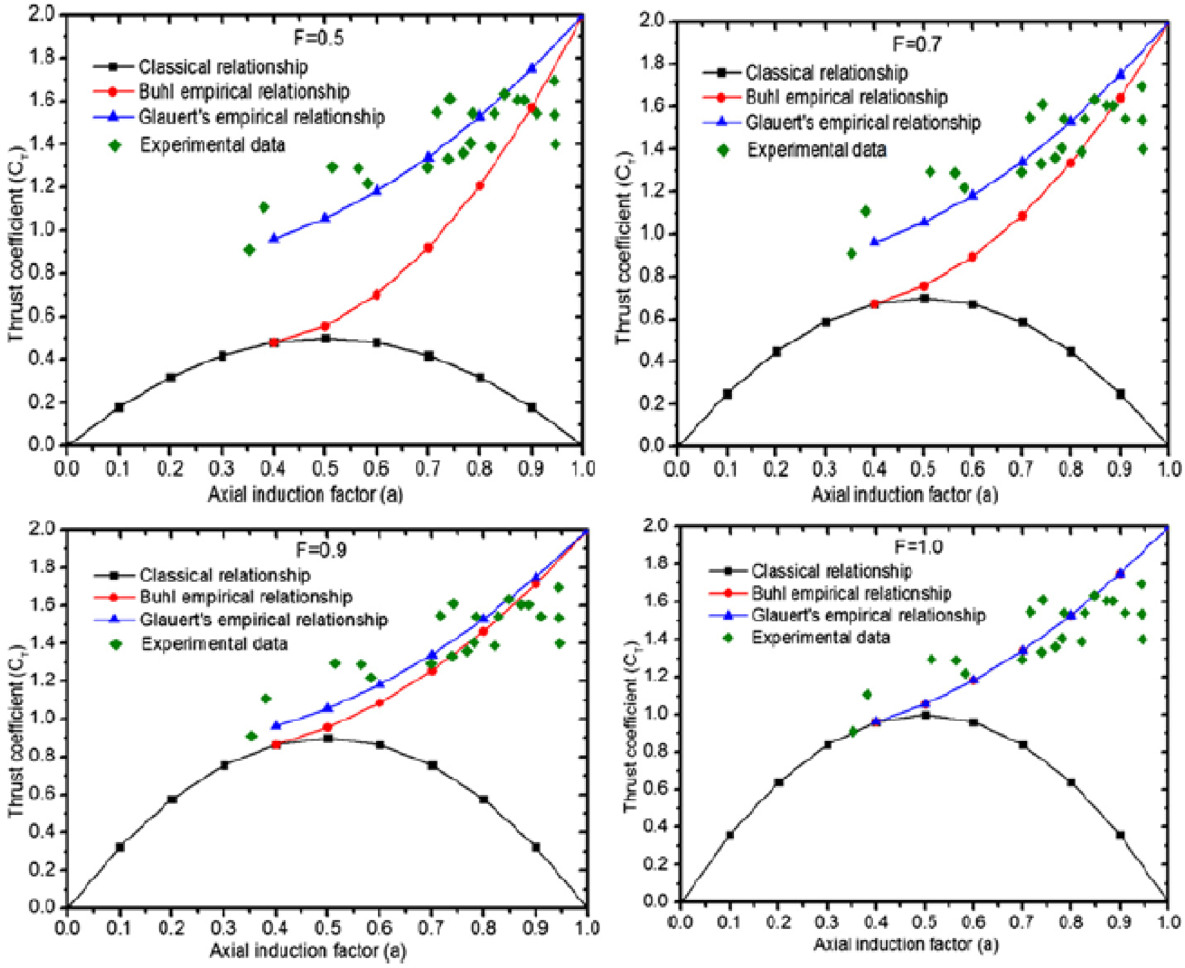

Figure 5.2: Glauert correction with and without Buhl modification for different values of F (Liu & Janajreh 2012)

This gap creates a discontinuity when a computer is used to iterate for the induction factor. This was fixed by choosing a parabola curve that has the same value and slope for a=0.4 as the classical equation with losses, and that goes through C_T=2.0 at a=1. By using algebra, the following relation was then found.

$$C_T = \frac{8}{9} + \left(4F - \frac{40}{9}\right) a + \left(\frac{50}{9} - 4F\right) a^2 \tag{5.8}$$

Or, solving for the induction factor,

$$a = \frac{18F - 20 - 3\sqrt{C_T(50 - 36F) + 12F(3F - 4)}}{36F - 50} \tag{5.9}$$

In these equations, *F* represents the tip loss factor, *a* the axial induction factor and the thrust coefficient is denoted by C_T. The method was chosen to solve the numerical problem of the instability rather than to obtain a good fit for the empirical data of Glauert. The last equation (5.9) should be applied to the BEM model when C_T>0.96F (Buhl 2005). In the Figure 5.2, the red line illustrates that the instabilities are no longer present when the Buhl correction is applied.

5.2.3. 3D Stall-Delay correction

One of the assumptions made in the BEM theory is that only axial flow is taken into account and thus radial flow is neglected. In reality, at both ends of the blade, there can be some considerable amount of spanwise flow as well. The airfoil characteristics used are typically based on 2D wind tunnel tests on airfoils. Since a direct application of these 2D measurements often results in a bad agreement between measured and calculated loads a 3D correction is applied. This significantly improves the accuracy of the BEM predictions.

The need for this 3D correction of airfoil characteristics has resulted in several models over the past years. Well known models are those of Snel, (Snel et al. 1994), Du & Selig (Du & Selig 1998), Chaviaropoulos & Hansen (Chaviaropoulos & Hansen 2000) and Lindenburg (Lindenburg 2004). The models of Snel and Lindenburg only apply a correction to the lift coefficient, whereas the other two models also include a correction for drag. Furthermore, a model was developed by Sant (Sant 2007), based on and validated against measurements on the NREL Phase VI rotor in axial flow conditions. Another commonly used method to correct the drag polar is developed by Eggers (Eggers et al. 2003) and is used in aerodynamic tools such as AirfoilPrep, by NREL. All methods have the same basic formulation, which can be found in the equations below.

$$C_{l,3D} = C_{l,2D} + f_{Cl}(C_{l,lin} - C_{l,2D}) \tag{5.10}$$

$$C_{d,3D} = C_{d,2D} + f_{Cd}\left(C_{d,2D} - C_{d,2D-min}\right) \tag{5.11}$$

The table below denotes the lift and drag correction factors for the models mentioned. Note that in the correction developed by Sant, the result is lowered by the tip/root correction factor[1].

---

[1] The tip/root correction factor developed by Sant is given by the following relation:
$F = \left(\frac{2}{\pi}\right)^2 \cos^{-1}\left[exp\left\{-18\frac{1-{}^{r}/_{R}}{{}^{r}/_{R}}\right\}\right] \cdot \cos^{-1}\left[\exp\left\{-3.8\frac{{}^{r}/_{R}-{}^{R_r}/_{R}}{{}^{R_r}/_{R}}\right\}\right]$, where *R* represents the blade radius, *r* the radius at a specific location and R_r is the hub radius.

Table 5.1: Corrections of airfoil coefficients for 3D effects for various models

Model	**f_{Cl}**	**f_{Cd}**
Snel	$3\left(\frac{c}{r}\right)^2$	0
Lindenburg	$3.1\left(\frac{\Omega r}{V_{rel}}\frac{c}{r}\right)^2$	0
Du & Selig	$\frac{1}{2\pi}\left[\frac{1.6(c/r)}{0.1267}\frac{a-\left(\frac{c}{r}\right)\frac{dR}{\Lambda r}}{b+\left(\frac{c}{r}\right)\frac{dR}{\Lambda r}}-1\right]$ With $\Lambda = \Omega R/\sqrt{V_0^2+(\Omega r)^2}$ a=b=d=1	$-\frac{1}{2\pi}\left[\frac{1.6(c/r)}{0.1267}\frac{a-\left(\frac{c}{r}\right)\frac{dR}{2\Lambda r}}{b+\left(\frac{c}{r}\right)\frac{dR}{2\Lambda r}}-1\right]$
Chaviaropoulos & Hansen	$a\left(\frac{c}{r}\right)^h \cos^n(\beta)$ With a=2.2, h=1 and n=4	$a\left(\frac{c}{r}\right)^h \cos^n(\beta)$
Sant	$K_L(\alpha)\left[1-e^{-0.003(\max(\alpha,\alpha_s)-\alpha_s)^3}\right]$ With $K_L = g(m_0 - m\alpha)e^{-a(\alpha-\alpha_s)}$ $g, n, m, a, h, n_0 n, b = P\left(\frac{c}{r}\right)$	$K_D(\alpha)\left[1-e^{-0.003(\max(\alpha,\alpha_s)-\alpha_s)^3}\right]$ $K_D = h(n_0 - n\alpha)e^{-b(\alpha-\alpha_s)}$
Eggers	0	$\Delta C_D = \Delta C_l * \frac{\sin(\alpha) - 0.12\cos(\alpha)}{\cos(\alpha) - 0.12\sin(\alpha)}$ With $\Delta C_l = C_{l,3d} - C_{l,2d}$

The corrections are implemented and are compared to both 2D and 3D measurements on the NREL phase VI wind turbine at blade locations r/R of 0.3 and 0.8. The 2D measurements that are used as a basis for the correction were measured in the Ohio State University wind tunnel on the S809 airfoil at a Reynolds number of 750,000. The results can be found in the figure below.

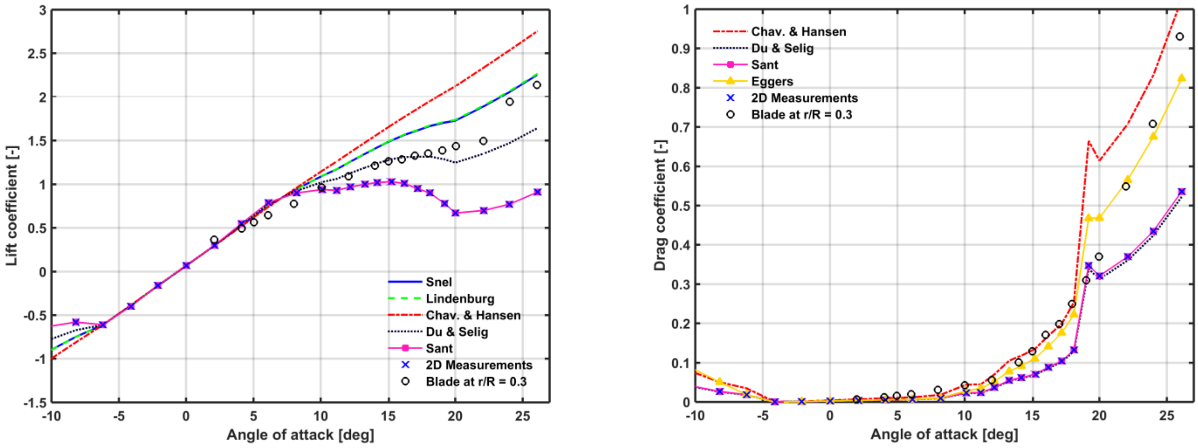

Figure 5.3: 3D corrected airfoil lift (left) and drag (right) characteristics for r/R = 30% compared to 2D measurements and measured 3D data.

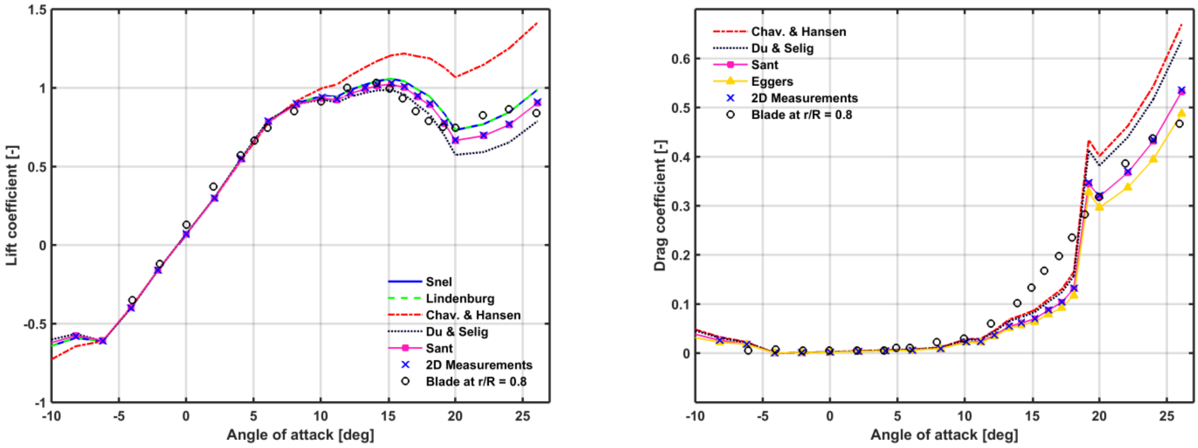

Figure 5.4: 3D corrected airfoil lift (left) and drag (right) characteristics for r/R = 80% compared to 2D measurements and measured 3D data

What can be observed from Figure 5.3 and Figure 5.4 is that the differences between 2D and 3D measurements are larger at 30% blade span position than the differences at 80%. Furthermore, as to the quality of the 3D correction models, it can be noted that the Du & Selig model is most capable of predicting the 3D lift coefficient at the two radial locations. The same can be said about the Eggers model for the drag prediction. These are therefore implemented in the BEM code that is used to compute the relative velocity and AoA distribution.

A final remark regarding the Sant 3D method, it can be seen from the figure that the difference between the 2D measurements and the correction by Sant is negligibly small. The figures from the report suggest that this should not be the case. Either the equations are implemented incorrectly into MatLab, or the report of Sant may contain a typographical error.

5.2.4. Polar extrapolation

As outlined in the previous paragraphs, the tool RFOIL is used to generate the polar data as well as boundary layer data. These data are then used to create the boundary layer database and compute the angle of attack and relative velocity distributions, which are all necessary for SILANT to predict the noise emission. A problem that can and often will occur is that RFOIL is only able to converge to solutions up to about 25 degrees angle of attack. Even then, the accuracy of the predictions is only reasonable up to $C_{l,max}$.

Especially in the root region of the blade, much higher angles are experienced by the blade. To be able to obtain polar data beyond this range, the lift and drag predictions by RFOIL are extrapolated. Viterna & Corrigan (Viterna & Corrigan 1982) and Montgomerie (Montgomerie 2004) both provide methods for lift and drag extrapolation up to high angles of attack. These methods will be described in the next section.

5.2.4.1. *Montgomerie extrapolation*

The extrapolation makes use of the fact that there exists some potential-flow-like behavior in a real airfoil between angles of -15 and 15 degrees, which can be emulated. At higher angles of attack, from 30 degrees onwards, the airfoil behaves like a basic thin plate. For intermediate angles, a transformation function *f* is used to simulate the sub-stall behavior. The total curve is an interpolation between the thin plate (s) and the potential flow curve (t), as described by the following relation:

$$C_L = f \cdot t + (1-f) \cdot s \qquad (5.12)$$

The function *f* is determined from two known points from the original C_L vs α curve. The last known point from the data should be used as point one. The second point is taken from somewhere near the middle between where the C_L curve leaves t and the last given point. The transformation function is now calculations by means of the expressions:

$$f = \frac{1}{1 + k \cdot (\Delta\alpha)^4} \tag{5.13}$$

Where

$$f_n = \frac{C_L(\alpha_n) - s(\alpha_n)}{t(\alpha_n) - s(\alpha_n)} \quad n = \{1,2\} \tag{5.14}$$

$$\Delta\alpha = \alpha_M - \alpha \tag{5.15}$$

$$k = \left(\frac{1}{f_2} - 1\right)\frac{1}{(\alpha_2 - \alpha_M)^4} \tag{5.16}$$

The point α_m is defined as the angle where the C_L curve starts to deviate from the potential flow curve *t*. The interpolation of these functions is graphically shown in Figure 5.5 below.

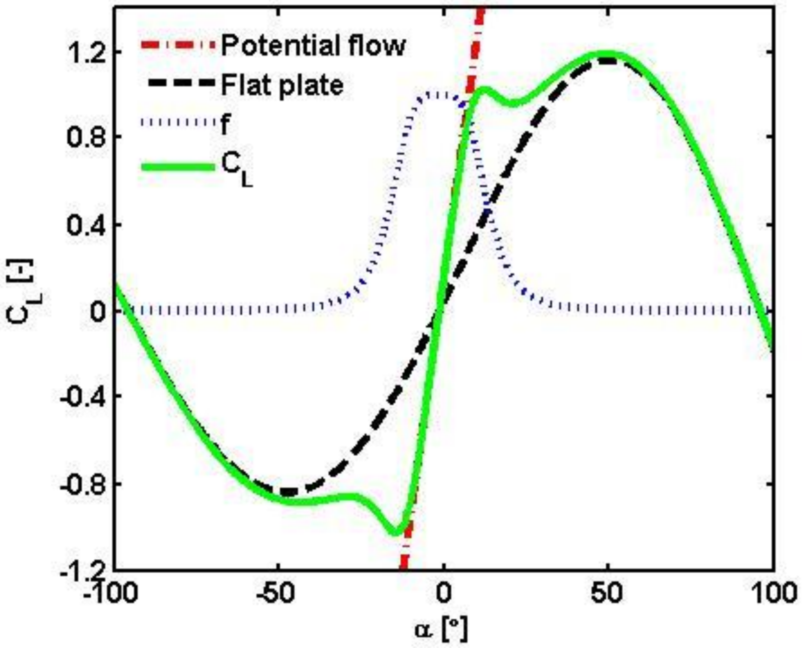

Figure 5.5: lift curve extrapolation principle according to the Montgomerie method

As can be seen, the transformation function has a value between zero and unity. It is utilized to interpolate the lift curve between the potential flow and the cambered thin plate curve. This cambered thin plate curve uses a basic flat plate curve but is modified to include camber and rounded nose effects. In the figure above this process is shown for the positive side of the lift polar, a similar method is used to construct the negative side.

The extrapolation of the drag polar is done in a comparable way. The transformation function *f* that was used for the lift curve extrapolation is applied to interpolate two functions. The first being the drag curve for a thin plate, the second is an extension of the given aerodynamic set by RFOIL. This extension is computed as follows. First the difference between the given lift polar and the lift curve for a thin plate is calculated. The deviation of the two curves is associated with an increasing loss in momentum of the flow, and thus the drag. The increase in drag is now assumed to be proportional to the increase in lift and this is used to extend the known aerodynamic set to higher angles of attack. A final important remark regarding the Montgomerie extrapolation: it is solely used to extend the RFOIL predictions to angles beyond the computed range.

In the following Figure 5.6, the Montgomerie extrapolation is shown for the DU96-W-180 airfoil and compared to measurements at high angles of attack at a Reynolds number of 700,000 (Timmer 2010). The Montgomerie extrapolation is based on RFOIL predictions, which are shown in the figure as well.

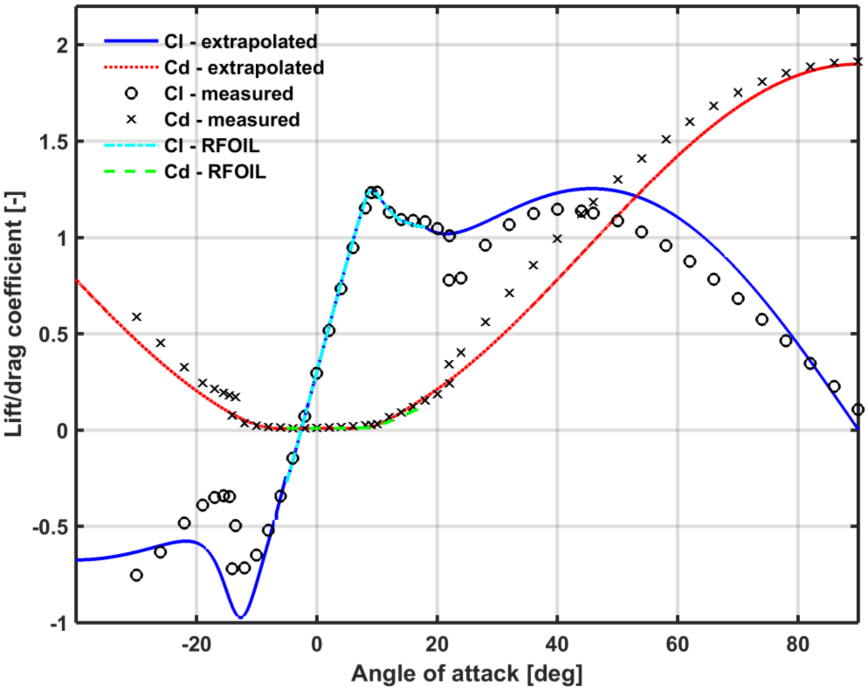

Figure 5.6: Measurements and Montgomerie extrapolation for the DU96-W-180 airfoil at RE = 700,000

The figure above shows that the airfoil predictions for both the lift and the drag curve are accurate in the RFOIL angle of attack range. The deep-stall behavior of the airfoil is not captured by the Montgomerie method. For the higher angles, the extrapolation of the lift curve slightly over predicts the wind tunnel measurements. As for the drag prediction, similar observations are made. The drag prediction by RFOIL (increased by 10%) is done reasonably well for low angles of attack. For angles higher than 20 degrees, the drag is strongly under predicted by the extrapolation. The magnitude of the drag coefficient at 90 degrees of the extrapolation matches that of the measurements.

An important note must be made regarding this example. The quality of the extrapolation is largely dependent on the (post-stall) prediction by RFOIL. In this situation the post-stall behavior is captured reasonably well. However, for other airfoils this might not be true and the drop in lift simulated by RFOIL deviates significantly from measurements. In this case the Montgomerie extrapolation will also be less accurate.

However, small to moderate deviations from the measured values are not deemed critical for the following reason. The extrapolated angles that exceed the RFOIL predicted range only occur in a small root region of the blade, a section that is both of minor aerodynamic and acoustic importance.

Thus, small differences in this section will not affect the accuracy of the total noise prediction of SILANT drastically.

Both extrapolation models are used to only extend the polar data to high angles of attack, not the boundary layer data. Currently, no method exists to execute such an extrapolation of the boundary layer parameters, nor is one used here. It is also not known how SILANT exactly computes the displacement thickness at angles beyond the RFOIL range. This is neither mentioned in the manual (Boorsma & Bulder 2010), nor user documents (Hagg 1996). It is suspected that a curve fit is used to extrapolate the boundary layer data to high angles of attack.

5.2.4.2. *Viterna-corrigan extrapolation*

Another method to extrapolate the polar data to high angles of attack is the model of Viterna & Corrigan (V&C) (Viterna & Corrigan 1982). In their research, they propose an empirical model following from measurements on a 100 kW and a 200 kW stall-controlled wind turbine. The associated pitch for constant rated power was translated into airfoil post-stall performance.

The method is widespread throughout airfoil literature and seems to have worked for the configurations that were investigated, it should be noted the method is a global one. Three-dimensional effects are included in the model, since the equations are based on matching the total maximum power of the entire rotor. These effects include the rotational effects that are dominant in the root section of the blade. As explained in section 5.2.3 these 3D effects are dependent on the local value of the rotor solidity c/r. This makes them also dependent on the blade layout.

The original Viterna equations require an initial angle of attack (α_{stall}) with the associated lift and drag coefficients as well as the blade aspect ratio (AR). The results with the Viterna equations are largely dependent on the magnitude of the initial values of C_l and C_d. The AR is of lesser importance and is only used to determine the maximum drag coefficient at 90 degrees. The equations are as follows:

$$C_{D,max} = 1.111 + 0.018 \cdot AR \quad for\ AR < 50 \tag{5.17}$$

$$C_{D,max} = 2.01 \qquad\qquad for\ AR \geq 50 \tag{5.18}$$

The AR is defined in this situation as the blade radius divided by the chord length at 75% of the span: AR = R / $c_{0.75R}$. The lift and drag coefficients can now be computed as follows:

$$C_D = C_{D,max} \sin^2 \alpha + K_1 \cos \alpha \tag{5.19}$$

With

$$K_1 = \frac{(C_{D,stall} - C_{D,max} \sin^2 \alpha_{stall})}{\cos(\alpha_{stall})} \tag{5.20}$$

And

$$C_L = \frac{1}{2} C_{D,max} \sin 2\alpha + K_2 \frac{\cos^2 \alpha}{\sin \alpha} \tag{5.21}$$

Where

$$K_2 (C_{L,stall} - C_{D,max} \sin \alpha_{stall} \cos \alpha_{stall}) \frac{\sin \alpha_{stall}}{\cos^2 \alpha_{stall}} \tag{5.22}$$

The choice of the airfoil's stall angle of attack and associated drag strongly influence the results of the extrapolation. In the original report, the equations are based on using the stall AoA at maximum C_l. However, Tangler & Kucorek suggested to replace this by using the deep stall angle instead (Tangler & Kocurek 2005). This leading-edge separation angle corresponds to the local C_l minimum just after maximum C_l. It was found that good performance prediction was achieved by applying this method.

The Viterna-Corrigan method described above is implemented into MatLab and applied to the DU96-W-180 airfoil. As suggested by Tangler & Kucorek, the deep stall angle is used as a starting point for the extrapolation. Below the point where leading edge separation is present, the wind tunnel measurements are used. The results, compared to RFOIL predictions, are shown in the figure below.

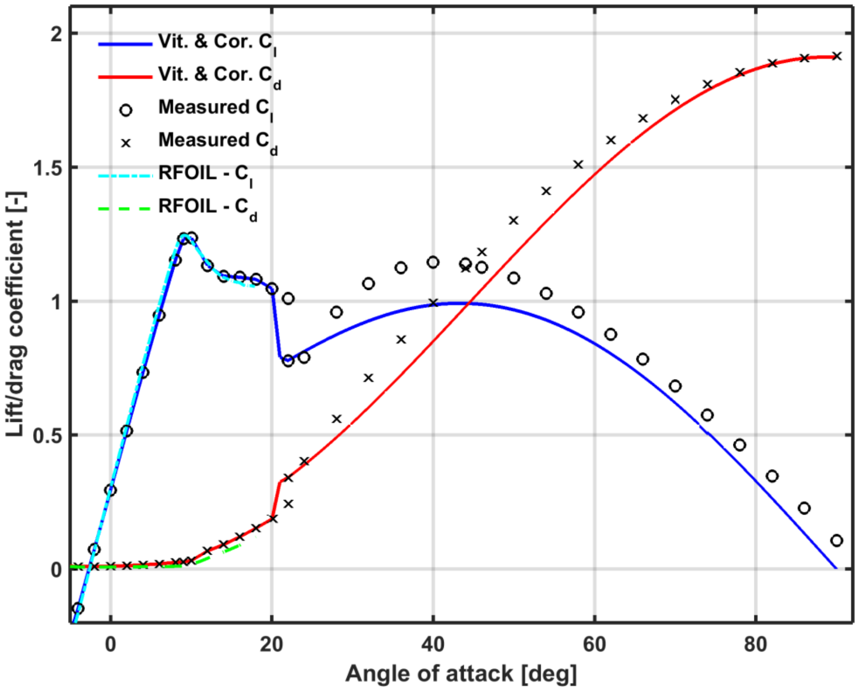

Figure 5.7: Measurements and Viterna-Corrigan extrapolation for the DU96-W-180 airfoil at RE = 700,000

The figure above shows similar results as the Montgomerie extrapolation. The deep stall point is found in the extrapolation, for the obvious reason that it is used as a starting point for the extrapolation. If the RFOIL simulation was used, which is not able to predict this point of leading edge separation, this would not be the case. Furthermore, the lift beyond this point is underpredicted. The deviations between the extrapolated drag curve and the measured one are in the same order of magnitude. $C_{d,max}$ was predicted correctly as well. However, as pointed out before, the V&C extrapolation is based upon measurement on the entire blade. This means that 3D effects are included. The wind tunnel measurements performed on the DU96-W-180 airfoil are based on a non-rotating segment and therefore experiences 2D behavior. Comparing the two is therefore difficult.

The Figure 5.6 and Figure 5.7, where the results of both post-stall prediction methods are presented, show that both algorithms provide similar results. However, due to fact that the Montgomerie method is a 2D model, and therefore other corrections can be applied to it as well, this model is selected to be implemented in the BEM code. Furthermore, in this situation the V&C performs reasonably well, because it is based upon the measured deep stall angle. However, RFOIL is rarely able to compute polar data up to this point and it is therefore not always known.

All the corrections that are used in the BEM aerodynamic model are now explained. A validation of the described model, with the corrections included, can be found in Appendix C, in order to get an idea of the accuracy of the model. The remainder of the chapter will focus on the thorough description and validation of SILANT as well as the predictions made by the program itself.

5.3. Acoustic source modeling

As mentioned in the beginning of the chapter, the noise predictions made by SILANT take into account the trailing edge noise, the inflow noise and the tip noise. The scope of this section is to describe the models upon which these noise mechanisms are based.

5.3.1. Trailing-edge noise

For the prediction of the trailing-edge noise, the most commonly used model is that of Brooks, Pope and Marcolini (BPM). This is also the model that is used in the SILANT tool. It requires the input of the boundary layer displacement thickness at the trailing edge for both the pressure and the suction side of the airfoil. This displacement thickness of the airfoil shape is calculated by RFOIL, which requires the Reynolds number and angle of attack to be known. The sound power level according to this model is calculated as follows:

$$L_W = 10\log_{10}(4\pi\delta^* M^5 s) + A(f, \alpha, U_e, \delta^*) \tag{5.23}$$

L_W : Sound Power Level
δ^* : Trailing edge boundary layer displacement thickness
U_e : Local effective incoming velocity
M : Mach number
s : Segment width
α : Angle of attack
f : Frequency
A : Spectral function

The frequency dependent function A determines the spectral shape of the noise. If the angle of attack is above stall the model switches to separation-stall mode by modifying this spectral function. A more detailed description of the model can be found in paragraph 6.1.2.

5.3.2. Inflow noise

The interaction between the airfoil and the turbulence in the oncoming flow results in inflow noise. To model this noise source, the model of Amiet and Lowson (Amiet 1975) is used, by applying the following formula.

$$L_W = 10\log_{10}\left(4\pi M^5 s L \frac{u'^2}{U_e^2} B(f, U_e, L, c)\right) + 181.3 \tag{5.24}$$

L_W : Sound Power Level
U_e : Local effective incoming velocity
M : Mach number
s : Segment width
α : Angle of attack
f : Frequency
c : Local chord
L : Turbulence length scale
u'^2 : variance of turbulent velocity fluctuations
B : Spectral function

Again, the spectral shape of the noise is determined by the function B. The turbulence characteristics are defined by the turbulence length scale and variance of velocity fluctuations. These are determined using the specified roughness length and element height (Burton et al. 2001).

5.3.3. Tip noise

The tip of the blade is subjected to turbulent flow that interacts with the trailing edge due to the formation of the tip vortex. This tip noise thus only occurs at the tip region and this noise contribution is therefore only calculated for the tip elements, again using the BPM model (Brooks et al. 1989).

$$L_W = 10\log_{10}(4\pi M^5(1+0.036\alpha)^3 l^2) + C(f, l, U_e, \alpha) \tag{5.25}$$

L_W : Sound Power Level
U_e : Local effective incoming velocity
M : Mach number
α : Angle of attack
l : Spanwise extent of separation
C : Spectral function

The function C is used to include the spectral shape of the noise. The spanwise extent of separation (l) is determined using the relation

$$\frac{l}{c} \approx 0.008\alpha \tag{5.26}$$

Where the parameter c represents the chord length of the tip section. This equation is only valid for rounded blade tips.

5.3.4. Sound propagation modeling

To determine the immission of noise at the receiver position, in addition to the sound power the sound propagation effects also have to be taken into account. These propagation effects are calculated separately at each blade element-observer combination and each source. To determine the location, orientation and velocity of each element, the tool requires the radial location, hub height, pitch, tilt and cone angle as well as azimuth position and the rotational speed. How these contributions are incorporated to obtain the sound pressure level each element receiver location can be seen in the following formula.

$$SPL = L_W + L_{DI} + L_{CA} + L_{spread} + L_{att} + L_{meteo} \tag{5.27}$$

SPL : Sound pressure level
L_W : Sound Power Level
L_{DI} : directivity
L_{CA} : convective amplification
L_{spread} : spherical spreading
L_{att} : atmospheric attenuation
L_{meteo} : refraction and ground effect

After these propagation effects have been incorporated, A-weighting can be applied to include the acoustic response of the human ear. The different contributions of the propagation model are briefly outlined in the paragraphs below.

5.3.4.1. *Directivity and convective amplification*

The sound propagation phenomena directivity and convective amplification have been treated in section 4.2. It was explained that BPM (Brooks et al. 1989) developed directivity equations for the directional attenuation of sound and they based their work upon the analytical expressions derived by Amiet (Amiet 1976). As can be seen from equation (5.27), the directivity equations (4.1) & (4.2) in section 4.2.1 are added separately. However, they are based upon the same expressions. The noise mechanisms trailing edge noise and tip noise are assumed to have high frequency directivity patterns $(\overline{D_h})$, whereas the low frequency directivity (D_l) equation described most accurately represents the inflow noise mechanism.

5.3.4.2. *Geometrical spreading*

As outlined in section 3.2, as the distance of the observer is increased relative to the source, the sound pressure level decreases. In the model, uniform spherical spreading is assumed, which results in the following equation:

$$L_{spread} = -10\log(4\pi r^2) \tag{5.28}$$

In this equation, the parameter *r* represents the source-receiver distance. This distance is taken as the direct linear line between these two points.

5.3.4.3. *Atmospheric attenuation*

As sound propagates through the atmosphere, its energy is gradually converted to heat. This is due to a number of processes such as shear viscosity, thermal conductivity, and molecular relaxation (Hubbard & Shepherd 1990). These processes reduce the acoustic energy and result in a lower sound pressure level. This process is dependent on the frequency, temperature and relative humidity and is described by the formula below.

$$L_{att} = -\alpha(f, T, H) \cdot \mathrm{r}/100 \tag{5.29}$$

α : attenuation coefficient
f : frequency
T : temperature
H : relative humidity

In the prediction tool, the temperature is fixed to 288 K and the relative humidity to 50%. Experiments show that the atmospheric absorption is most felt at the high frequencies. The unit of the attenuation is dB/100 m.

5.3.4.4. *Refraction and ground effect*

Refraction effects can occur due to wind speed and temperature gradients. This causes non-uniform sound propagation as a function of azimuth angle from the source. These effects may result in a shadow zone at sufficient distance upstream of the turbine. This phenomenon is illustrated in Figure 5.8 below.

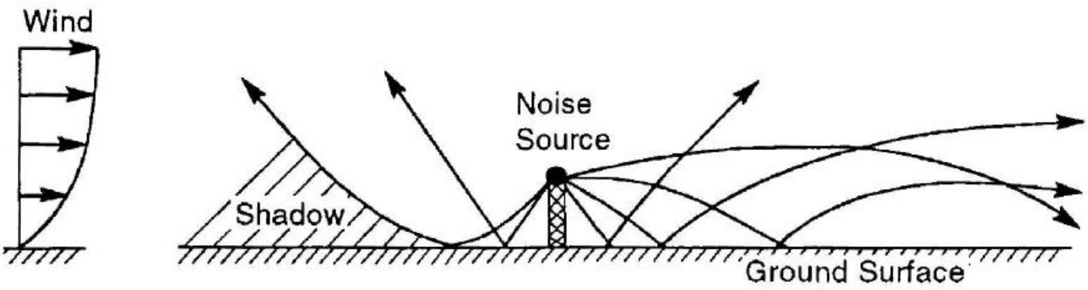

Figure 5.8: Effects of wind induced refraction (Hubbard & Shepherd 1990)

Note that in the downwind direction the wind gradient causes the sound rays to bend towards the ground, whereas in the upwind direction the rays curve upward away from the ground. For high-frequency acoustic emissions, this leads to an increased attenuation in the shadow zone upwind of the source, but little in the downwind direction (Hubbard & Shepherd 1990). The angle of incidence with respect to the ground will change due to refraction, which influences the way sound rays are absorbed or reflected by the ground. In SILANT, a relatively simple model from Van Beek (Van Beek & Van den Haspel 1989) is implemented to take these frequency dependent effects for a flat terrain with soft (grass type) ground. In this model, variations of temperature with respect to the ground are neglected.

$$\text{f<200 Hz} \qquad L_{meteo} = \begin{cases} 0 & r < 2S \\ -50\log\frac{d}{2S} & 2S < r < 5S \\ -20 & r > 5S \end{cases} \tag{5.30a}$$

$$\text{200<f<600 Hz} \qquad L_{meteo} = -25\log\left(-\frac{\alpha_i}{1.25}\right) + 2 \tag{5.30b}$$

$$\text{f>600Hz} \qquad L_{meteo} = \begin{cases} 0 & r < S \\ -75\log(d/S) & S < r < 2.5S \\ -30 & r > 2.5S \end{cases} \tag{5.30c}$$

d : horizontal distance from source to receiver
α : angle of incidence with respect to the ground
S : horizontal distance from source to shadow zone along propagation path

The shadow zone location and angle of incidence are estimated from the meteorological conditions and the source receiver geometry (Van Beek & Van den Haspel 1989).

5.3.4.5. *Doppler effect*

A noise source approaching a receiver will result in a higher observed frequency and vice versa. For example the sound of a race car will seem higher when it drives towards you compared to the sound when it drives away. This is known as the Doppler effect and it is accounted for by using eq. (5.31) below.

$$\frac{f'}{f} = 1/(1 - M \cdot \cos\theta) \tag{5.31}$$

Where *f'* represents the Doppler shifted frequency in Hz.

5.3.4.6. *Retarded time effect*

To estimate the variation in time of the noise immission it is necessary to take the time delay of the traveling sound waves into account.

$$\Delta t = r/a_{eff} \tag{5.32}$$

In the formula, the variable Δt is the time delay and a_{eff} the effective speed of sound. This effective speed of sound is taken as the speed of sound at a height above the receiver of 80% of the vertical source receiver distance, also taking into account the velocity and direction of the wind.

5.4. SILANT validation

To see whether the used acoustic program SILANT can produce realistic results, the validation of the tool is presented in this section. As stated previously, the noise sources that are taken into account are trailing edge noise (including separation-stall noise), tip noise and inflow noise. From the noise sources that are described in section 4.1 vortex-shedding noise and blunt trailing edge noise are omitted. This is most likely done due to the assumption that vortex-shedding noise is considered to be only relevant for small wind turbines, with Reynolds numbers below 1 million (Oerlemans 2011). Furthermore, it was already mentioned that the outer section of the blade makes the biggest contribution to the total noise emission. In this region, generally only airfoils with sharp trailing edges are used, in which case blunt trailing edge noise does not play a significant role.

The latter does have consequences in attempting to validate the tool. The previous assumptions imply that only the somewhat bigger wind turbines can be used and the smaller wind turbines rule out. This poses a challenge, for often blade geometric data as well as acoustic data are available for smaller wind turbines, but not for larger ones. Generally, it is difficult to find both these types of data for larger turbines, due to the confidential nature of the data.

The turbine ultimately selected for the validation was the Siemens SWT 2.3-93 m wind turbine. Blade geometry and operating data were unfortunately not available, so an approximation was used to model them. It was constructed using reverse engineering techniques by using only open information such as reports and brochures Carlén (Carlén 2005). The information used is shown in the Table 5.2 & Table 5.3 and Figure 5.9 below.

Table 5.2: Siemens SWT 2.3-93 general specifications

Siemens SWT 2.3-93 specifications			
Parameter	**Value**	**Parameter**	**Value**
No. of blades	3 [-]	**Power regulation**	Pitch
Rotor diameter	92.4 [m]	**Airfoil type**	FFA-W3-XXX/NACA63-6xx
Hub height	80 [m]	**Blade chord**	See Figure 5.9
Rated power	2300 [kW]	**Blade twist**	See Figure 5.9
Tilt angle	6 [°]	**Pitch angle**	-2 to 82 [°]
Cone angle	2 [°]	**Density**	1.225 [kg/m^3]
Rotational speed	Variable		

As far as the blade geometry is concerned, is consists of a FFA-W3-XXX series profile at the inner part of the blade, and a NACA63-6XX series airfoil at the outer sections. The assumed airfoil distribution along with the maximum thickness can be found in Table 5.3 below. For a smooth transition between the NACA and the FFA profiles a transition airfoil is assumed.

Table 5.3: Airfoil names and associated thickness

t/c	100%	36%	33%	30%	27%	24%	21%	-	18%	15%
Airfoil	cyl	w3-360	w3-332	w3-301	w3-270	w3-241	w3-211	trans	63-618	63-615
No. #	1	2	3	4	5	6	7	8	9	10

To obtain the complete picture of the blade shape for SILANT to do the acoustic analysis the chord, twist and thickness distributions were derived by Carlén (Carlén 2005) as well, and are depicted in Figure 5.9 below. The positions of the airfoils were then based upon the thickness distribution, in such a way that the relative thickness of the airfoil corresponds to the relative thickness of the blade at that location.

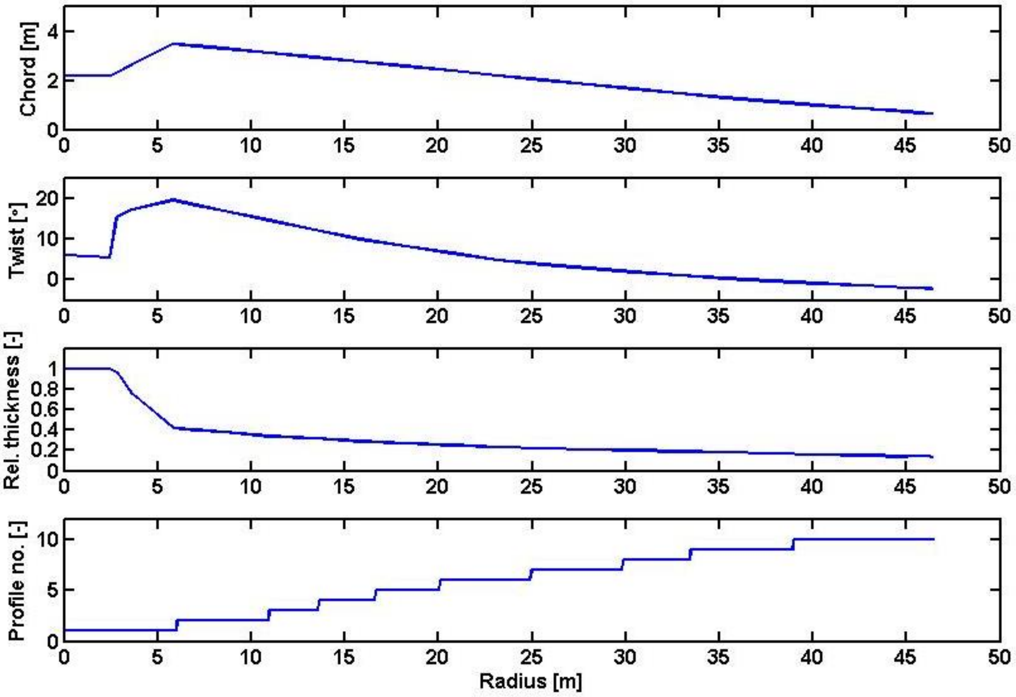

Figure 5.9: chord, twist, thickness and airfoil distribution of the Siemens blade

Next it is necessary to verify whether the estimated blade geometry/control settings of the Siemens turbine were estimated correctly. If this is not the case, any predictions made by SILANT would be meaningless. In order to verify this, the BEM model is used to calculate the power curve based on the estimated data. Then this predicted power curve is compared to the published sales power curve. The author realises this is not ideal for such a validation, and data such as the thrust coefficients at various wind speeds would provide a better insight. However since such data is not available, the power curve will suffice. In the Figure 5.10 below, a comparison of the calculated versus the published power curves can be found.

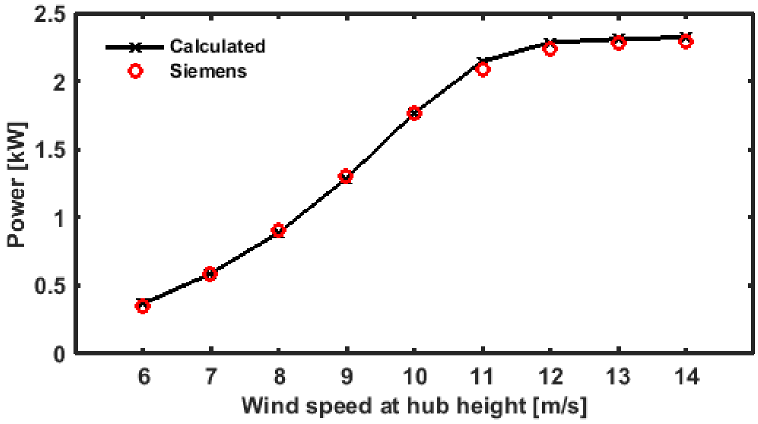

Figure 5.10: Siemens SWT 2.3-93m power curve

It can very easily be seen that the power predicted by the BEM model with the data from the report by Carlén (Carlén 2005) and the sales power curve supplied by Siemens correspond very well. This is an indication that the blade geometry and operating/control settings of the Siemens turbine were estimated correctly. To further evaluate this, the AoA distributions as well as the relative velocity distributions along the blade for the various wind speeds are shown in Figure 5.11 below.

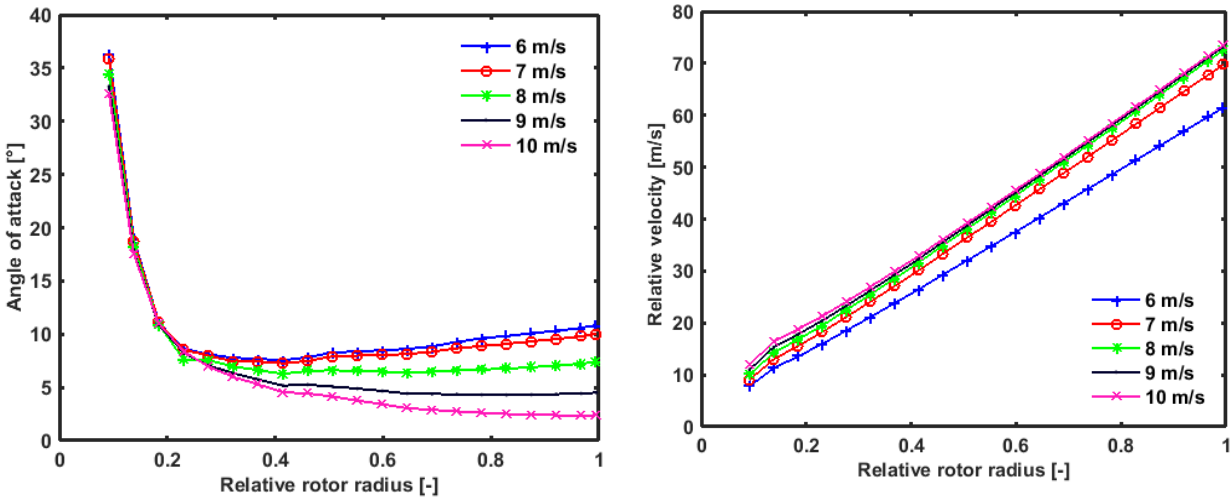

Figure 5.11: AoA (left) and V_{rel} (right) distributions along the blade span for wind speeds at reference height of 6-10 m/s

The figures show that the BEM model with corrections performs better for this pitch-regulated wind turbine. The pitching of the blades ensures the AoA remains fairly constant around α_{design} and below the stall angle. Furthermore it can be seen that the relative velocity curve shifts upward for higher wind speeds up to a certain maximum.

These data will be used as input to SILANT to compare the calculated noise output with the acoustic measurements of the Siemens turbine.

The noise measurements of the 2.3 MW Siemens wind turbine measured at the Høvsøre test site were used. The measurement data was added as an appendix for the KED wind power project Chatham Kent, Ontario. The measurements were executed by WINDTEST from 11 to 13 August 2005. All the measurements and analyses were done in accordance with the IEC 61400-11 acoustic measurement standard (IEC 61400-11 2002).

In the measurement campaign, the microphone was placed directly downwind of the turbine to enforce worst case sound propagation. It was placed at a distance of R_0=112 meter at a height of 0 m with respect to the turbine foundation. The surface roughness length was assumed to be 0.05m. This value was used to convert measured wind speeds from hub height to reference height using a standard logarithmic wind profile using the following equation.

$$V_{ref} = V_{hub}\left[\frac{\ln {}^{z_{ref}}/_{z_0}}{\ln {}^{H_{hub}}/_{z_0}}\right] \tag{5.33}$$

From the WINDTEST data, noise measurements were obtained for wind speeds between 6 and 10 m/s, at reference height. In the following figure, a plot of these measurements is shown and compared to the noise production calculated by SILANT. The combined uncertainty of the measurements is shown in the graph as well.

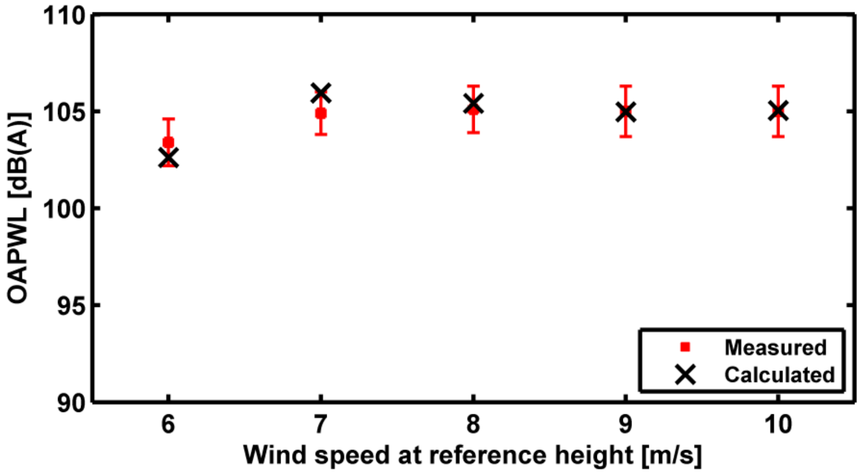

Figure 5.12: Siemens wind turbine acoustic measurements compared to SILANT prediction

When the measurements and the calculations are compared, one can see that the predicted values match the measured values nicely and within the limit. Especially at wind speeds 8 to 10 m/s. In order to identify whether the spectral shape can also be predicted accurately it is compared to these measurements as well. If this is the case, conclusions can be drawn as to the relevance of a noise source in airfoil design.

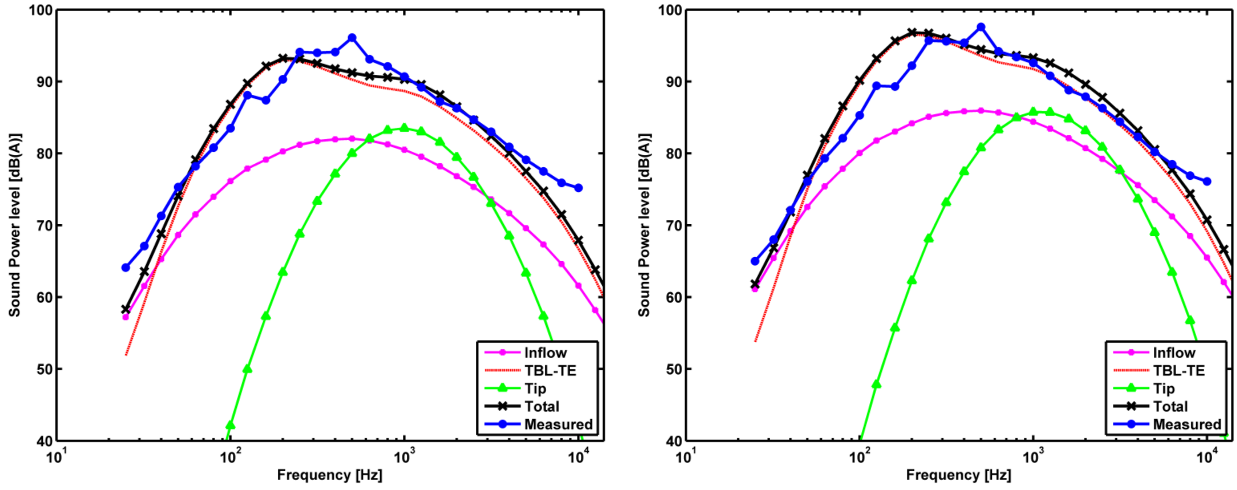

(a) V_{ref} = 6 m/s

(b) V_{ref} = 7 m/s

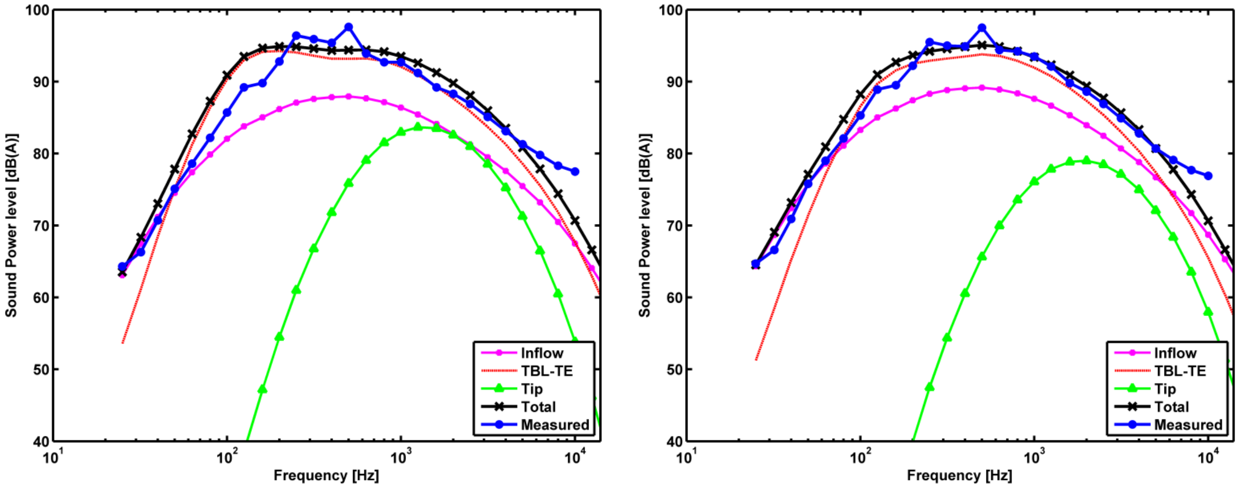

(c) V_{ref} = 8 m/s

(d) V_{ref} = 9 m/s

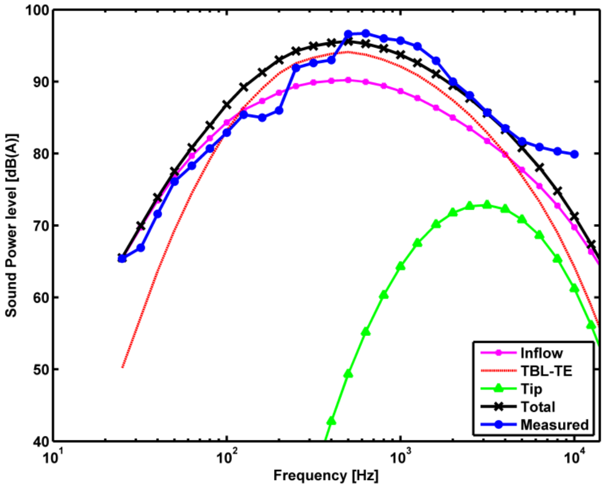

(e) V_{ref} = 10 m/s

Figure 5.13: Noise spectra for wind speeds at reference height of 6 to 10 m/s

For this 1/3 octave Sound Power Level spectrum the measured range is between 25 Hz and 10 kHz, which is also in accordance with the IEC 61400-11 standard. The results, for wind speeds at reference height between 6 and 10 m/s are shown in Figure 5.13 above.

The plots show that the SILANT is able to predict the noise spectra accurately as well, especially in the low frequency range between 30 and 80 Hz and in the region between 600 and 5000 Hz. Between 100 and 200 Hz the model overpredicts the noise level and SILANT also does not predict the peak at 500 Hz. Above 7 kHz the measured noise level is higher than the values predicted.

It can also be noted that the trailing edge noise is dominant over almost the entire spectrum for all wind speeds measured. Especially in the mid-range frequencies the sound power level is dictated by the trailing edge noise mechanism. Inflow noise plays a role at frequencies higher than 7 kHz for the higher wind speeds and at frequencies in the low frequency range. However, since the sound level in these regions is ~20 dB(A) lower than the maximum sound level, it hardly affects the overall noise level. These noise spectra furthermore confirm what can also be found in literature, that the trailing-edge noise is the most dominant noise mechanism. It also points out that in order to reduce aerodynamic noise emitted by the blades, one should focus on reducing the trailing edge noise.

Finally, given the simplifications and assumptions made in both the aerodynamic and aero-acoustic models, the predictions are in good agreement with the measurements. Due to the lack of available detailed information of the blade, the geometry of the blade is also a source of error. Combined with the fact that almost all predictions remain within the uncertainty of the measurements, one can conclude that the tool is accurate enough to draw valid conclusions from. In the remainder of the thesis, where the scope will be on the design of a tip region airfoil, the optimization shall mainly focus on minimizing the trailing edge noise.

6. Trailing-edge noise prediction models

Research has been done for several decades on the topic of aerodynamic noise, given the works of Brooks & Schinkler (Brooks & Schlinker 1983) and Ffowcs Williams & Hall (J. E. Ffowcs Williams and L. H. Hall 1970). These researches focused on the acoustics of airfoils developed for helicopters, but immediately showed great interest when applied to wind turbines, because of the similarities in operating conditions when it comes to the airfoils involved. Differences are the velocities and the direction of the flow experienced.

Despite these fundamental aero-acoustic researches, this has resulted in very few applicable engineering tools, however. The works of Brooks, Pope & Marcolini (Brooks et al. 1989), briefly discussed in the previous chapter, was one of the first to successfully make use of previous helicopter researches and later used by others in applications for wind turbines (Lowson 1993) making it one of the most used works on the subject. The model is based on detailed aero-acoustic measurements of the NACA 0012 airfoil. From these measurements, a semi-empirical prediction method was developed. Simple and direct mathematical expressions are used for computing sound pressure levels, dependent on only boundary layer parameters and flow conditions. However, this simplicity also reveals the major limitations: the empirical nature of the expressions; and the formulations to compute the boundary layer parameters are not suitable for generalization to other airfoils. These limitations make the applicability to more cambered airfoils difficult, and may result in inaccurate sound pressure levels.

Another, more recently developed, airfoil aero-acoustic model is mostly referenced to as the TNO model. It was originally presented by Parchen (Parchen 1998). The method accurately predicts the boundary layer behavior on an airfoil and its effects on the far field noise. The model is more analytical than the BPM and is derived from a combination of FW-H model mentioned in section 4.1, combined with the results of diffraction theory over a flat plate from Curle (Curle 1955). The necessary turbulent boundary layer parameters can be collected through various sources. Either a panel method such as XFOIL or RFOIL can be used, or a Computational Fluid Dynamics (CFD) code including a turbulence model can be considered.

This chapter focuses on extensively introducing these two most commonly used airfoil acoustic models. Merely trailing edge noise models will be discussed, because the previous chapter showed that this was the biggest contributor to the total noise. In the first paragraph, the BPM boundary layer equations will be outlined. In the adjoining section BPM model for the trailing edge noise will be considered, and finally the TNO model will be elaborated on.

6.1. The Brooks, Pope & Marcolini model

6.1.1. The Brooks, Pope & Marcolini boundary layer model

The semi-empirical boundary layer expressions of BPM are deduced from measurements on a NACA0012 profile at various conditions. Hot-wire probe measurements were placed in the near wake region of the sharp trailing edge of the models. From this, the integral boundary layer parameters, the displacement thickness δ^* and momentum thickness θ, were calculated from the mean velocity profiles with the boundary layer (at the near wake) thickness δ specified. For the calculations, δ was defined as the distance from the airfoil surface were the velocity reaches 99 percent of the potential flow stream velocity (Brooks et al. 1989).

First, they established expressions for the integral BL parameters normalized by the chord. This was done through a curve fit for flow conditions at zero degrees angle of attack varying only the Reynolds number in both tripped and untripped conditions to yield equations (6.1) to (6.6). Then, to include angle of attack effects on the thickness parameters, Reynolds number was kept constant and the AoA was varied (equations (6.7) to (6.14)). The approach led set of expressions shown below:

Tripped boundary layer

$$\frac{\delta_0^*}{c} = \begin{cases} 0.0601 * Re^{-0.114} & ,Re \le 0.3 \cdot 10^6 \\ 10^{3.411-1.5397*\log(Re)+0.1059*\log(Re)^2} & ,Re \le 0.3 \cdot 10^6 \end{cases} \tag{6.1}$$

$$\frac{\delta_0^*}{c} = \begin{cases} 0.0601 * Re^{-0.114} & ,Re \le 0.3 \cdot 10^6 \\ 10^{3.411-1.5397*\log(Re)+0.1059*\log(Re)^2} & ,Re \le 0.3 \cdot 10^6 \end{cases} \tag{6.2}$$

$$\frac{\theta_0}{c} = \begin{cases} 0.0723 * Re^{-0.1765} & ,Re \le 0.3 \cdot 10^6 \\ 10^{0.5578-0.7079*\log(Re)+0.0404*\log(Re)^2} & ,Re \le 0.3 \cdot 10^6 \end{cases} \tag{6.3}$$

Untripped boundary layer

$$\frac{\delta_0}{c} = 10^{1.6569-0.9045*\log(Re)+0.0596*\log(Re)^2} \tag{6.4}$$

$$\frac{\delta_0^*}{c} = 10^{3.0187-1.5397*\log(Re)+0.1059*\log(Re)^2} \tag{6.5}$$

$$\frac{\theta_0}{c} = 10^{0.2021-0.7079*\log(Re)+0.0404*\log(Re)^2} \tag{6.6}$$

Pressure side boundary layer values (valid for both tripped and untripped flow)

$$\frac{\delta_p}{\delta_0} = 10^{-0.04175\alpha_*+0.00106\alpha_*^2} \tag{6.7}$$

$$\frac{\delta_p^*}{\delta_0} = 10^{-0.0432\alpha_*+0.00113\alpha_*^2} \tag{6.8}$$

$$\frac{\theta_p}{\delta_0} = 10^{-0.04508\alpha_*+0.000873\alpha_*^2} \tag{6.9}$$

Suction side boundary layer – tripped flow

$$\frac{\delta_s}{\delta_0} = \begin{cases} 10^{0.0311\alpha_*} & ,0° \le \alpha_* \le 5° \\ 0.3468 \cdot 10^{0.1231\alpha_*} & ,5° \le \alpha_* \le 12.5° \\ 5.718 \cdot 10^{0.0258\alpha_*} & ,12.5° \le \alpha_* \le 25° \end{cases} \tag{6.10}$$

$$\frac{\delta_s^*}{\delta_0} = \begin{cases} 10^{0.0679\alpha_*} & ,0° \le \alpha_* \le 5° \\ 0.381 \cdot 10^{0.1516\alpha_*} & ,5° \le \alpha_* \le 12.5° \\ 14.296 \cdot 10^{0.0258\alpha_*} & ,12.5° \le \alpha_* \le 25° \end{cases} \tag{6.11}$$

$$\frac{\theta_s}{\delta_0} = \begin{cases} 10^{0.0559\alpha_*} & ,0° \le \alpha_* \le 5° \\ 0.6984 \cdot 10^{0.0869\alpha_*} & ,5° \le \alpha_* \le 12.5° \\ 4.0846 \cdot 10^{0.0258\alpha_*} & ,12.5° \le \alpha_* \le 25° \end{cases} \tag{6.12}$$

Suction side boundary layer values – untripped flow

$$\frac{\delta_s}{\delta_0} = \begin{cases} 10^{0.03114\alpha_*} & ,0° \leq \alpha_* \leq 7.5° \\ 0.0303 \cdot 10^{0.2336\alpha_*} & ,7.5° \leq \alpha_* \leq 12.5° \\ 12 \cdot 10^{0.0258\alpha_*} & ,12.5° \leq \alpha_* \leq 25° \end{cases} \tag{6.13}$$

$$\frac{\delta_s}{\delta_0} = \begin{cases} 10^{0.03114\alpha_*} & ,0° \leq \alpha_* \leq 7.5° \\ 0.0303 \cdot 10^{0.2336\alpha_*} & ,7.5° \leq \alpha_* \leq 12.5° \\ 12 \cdot 10^{0.0258\alpha_*} & ,12.5° \leq \alpha_* \leq 25° \end{cases} \tag{6.14}$$

In these equations, α_* represents the angle of attack, which is corrected for the influence of the wind tunnel walls. This yields the angle in free air required to give the same lift as α would give in the tunnel. The BPM boundary layer method has both advantages and disadvantages; one of the advantages is its simplicity and ease of implementation. The code can very easily be implemented and can give results at very little computational costs. However, this also exposes its major limitation. Because the input only requires the angle of attack and the Reynolds number to be known, the shape of the airfoil is not taken into account. This makes the predictions only valid for airfoils very similar to the NACA0012, and applicability in optimization cases, where highly deformed airfoils also have to be considered, is ruled out. The boundary layer equations are therefore not used for optimization purposes. They can, however, be used to verify if the BPM aero-acoustic expressions are implemented correctly, which is done in the following section.

6.1.2. Brooks, Pope & Marcolini aero-acoustic model

The first acoustic model to be considered is the Brooks, Pope and Marcolini (BPM) model. Like the boundary layer expressions, this model is also based on detailed measurements of noise from NACA0012 airfoils on various conditions. The basis of the empirical relations are the scaling relations derived by Ffowcs Williams & Hall (J. E. Ffowcs Williams and L. H. Hall 1970) for the problem of turbulence convecting at low subsonic speed U_c above a large plate and past the trailing edge into the wake. The primary result of the analysis was

$$\langle p^2 \rangle \sim \rho_0^2 v'^2 \left(\frac{U_c^3}{c_0}\right) \left(\frac{L\mathcal{L}}{r^2}\right) \cdot \bar{D} \tag{6.15}$$

These results are used in many studies related to trailing edge noise. Here, $\langle p^2 \rangle$ represents the mean-square sound pressure at the observer located at a distance r from the edge. The medium density ρ_0, v'^2 is de mean-square turbulence velocity; and c_0 is the speed of sound. The variable L is the spanwise length and $\mathcal{L}$ is a characteristic turbulence correlation scale. The last factor which is present in the equation, $\bar{D}$, is the directivity and equals unity if the observer is located normal to the surface from the trailing edge. Making the assumptions that v' ~ U_c ~ U and $\mathcal{L}$ ~ δ or δ^* leads to this expression:

$$\langle p^2 \rangle \sim \left(\frac{U_c^5}{c_0}\right) (\frac{L\delta^*}{r^2}) \cdot \bar{D} \tag{6.16}$$

The equation shows that the noise intensity grows according to the fifth power of the inflow velocity and is a function of the turbulent length scale δ_s^*. These simplifications were applied by BPM to the FW-H equations and the rest of the parameters were fit from the results obtained from the NACA0012 measurements. This resulted in an expression which consists of scaling terms and frequency dependent terms. Applying the assumptions and simplifications above leads to the following general equation for the sound pressure level:

$$SPL = 10 \cdot \log\left(\frac{\delta_p^* M^5 s D_H}{r_e^2}\right) + F(St) + K \tag{6.17}$$

Here, the term *F* contains information regarding the sound level at different frequencies of the spectrum and it defines the noise spectrum shape. It is based on the Strouhal number (=fδ/U). The parameter *K* is used for scaling the amplitude of the curve. However, during the experiments, it was found that, in contrary to what was assumed, the normalized levels, Strouhal number and spectral shape were *not* independent on airfoil size, angle of attack and inflow velocity. BPM (Brooks et al. 1989) proposed to separate the data into two groups. The first was applied to cases corresponding to zero degree angle of attack; the other was applied to cases with nonzero angle of attack. This resulted into equations for the suction side, pressure side - which belong to the first case - and a formula for angle-dependent noise, representing the second case, given by

$$SPL_p = 10\log\left(\frac{\delta_p^* M^5 s D_H}{r_e^2}\right) + A\left(\frac{St_p}{St_1}\right) + (K_1 - 3) + \Delta K_1 \tag{6.18}$$

$$SPL_s = 10\log\left(\frac{\delta_s^* M^5 s D_H}{r_e^2}\right) + A\left(\frac{St_s}{St_1}\right) + (K_1 - 3) \tag{6.19}$$

$$SPL_\alpha = 10\log\left(\frac{\delta_s^* M^5 s D_H}{r_e^2}\right) + B\left(\frac{St_s}{St_2}\right) + K_2 \tag{6.20}$$

The subscripts *p* and *s* correspond to the pressure and suction side of the airfoil, respectively. The spectral terms A and B, the scaling terms K1, K2 and ΔK1 along with the full set of equations can be found in Appendix D. To compute the total value of the TBL-TE noise the individual contributions are acoustically summed in the following way:

$$SPL_{tot} = 10\log\left(10^{\frac{SPL_p}{10}} + 10^{\frac{SPL_s}{10}} + 10^{\frac{SPL_\alpha}{10}}\right) \tag{6.21}$$

6.1.3. Implementation of the code

The original BPM code was programmed in FORTRAN by the authors, and the equations were implemented in MatLab for this optimization.

To check whether the equations were correctly implemented in MatLab, it is checked with a test case from the appendix of the BPM report. This appendix contains the input operating conditions and associated output of the code. This gives the opportunity to compare the output of the codes and check whether they are identical. The test case uses the following input data:

Table 6.1: input operating conditions for the BPM model

Airfoil	**NACA 0012**
Chord [m]	0.3048
Airfoil span [m]	0.4572
Distance [m]	1.22
Θ_e [°]	90
Φ_e [°]	90
α [°]	1.516
U [m/s]	71.3

In the simulations, a viscosity of $1.4529 \cdot 10^{-5}$ m^2/s is used. The speed of sound was set to be 340.46 m/s. These are necessary parameters to calculate the Mach and Reynolds number. The following figure presents the results of both of the codes.

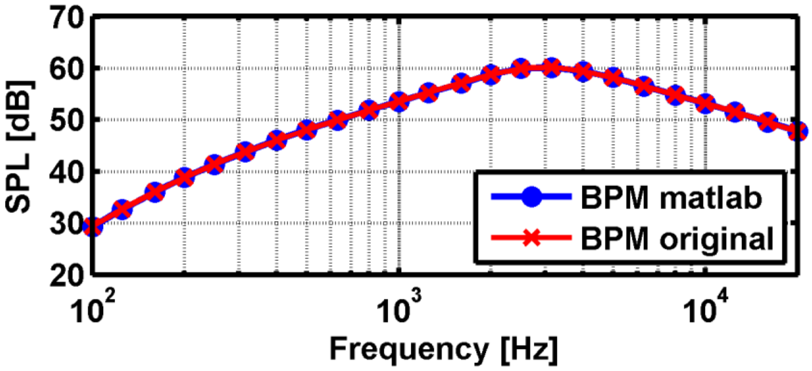

Figure 6.1: Comparison of MatLab implementation with original code

This figure shows the total noise level due to TBL-TE noise, which is the result of the three noise contributions (pressure side, suction side and angle-dependent noise) acoustically summed together. The figure leads to the conclusion that the output of the MatLab code matches the results mentioned in the BPM report very accurately. However, as stated in the previous section, the results of the BPM boundary layer code cannot be used in optimization cases. Therefore, the results will now be compared with the panel code XFOIL as boundary layer computation tool.

A tool that has the option to couple the BPM acoustic code to XFOIL is NAFNoise (NREL AirFoil Noise), a tool developed by NREL (Moriarty 2005). Furthermore, the tool has the option to select the BPM boundary layer prediction method as input as well. In the next plot a graphical comparison is made between the MatLab code, NAFNoise (both computed with XFOIL as boundary layer solver) and the original BPM data.

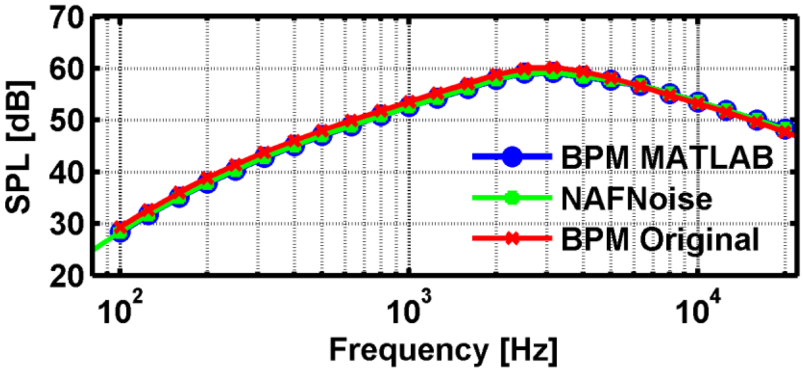

Figure 6.2: comparison between MatLab, NAFNoise and original code

This figure shows that the NAFNoise BPM predictions and the MatLab code are identical. Furthermore, they both show slightly lower results than those of the BPM report for frequencies below approximately 4 kHz. Because the deviation is only very limited, so XFOIL is able to nearly reproduce the NACA0012 results, but has the advantage that it can also deal with more deformed airfoils. The conclusion can be therefore drawn that the combination with an integral boundary layer method such as XFOIL is a very suitable replacement for the BPM boundary layer expressions. The quality of the prediction for other airfoils will be evaluated in the next chapter.

6.2. TNO model

The TNO model was originally formulated by Parchen (Parchen 1998), and is more analytical than the BPM model. It is derived from a combination of multiple models, which are combined to formulate a far field noise level expression as a function of turbulent boundary layer quantities. As discussed, these boundary layer parameters can, and will be, extracted from panel method solvers such as XFOIL and RFOIL. First, a brief explanation of the used models and equations is given.

The routine described in this section in order to compute the sound pressure level due to aerodynamic noise according to the TNO model is outlined in the report by Moriarty (Moriarty et al. 2005). The report describes the calculation process of the TNO model coupled to both a CFD and a panel method solver. Only the latter routine is outlined here.

The approach is based on the work of Blake (Blake 1986), and uses the wave-number spectrum of unsteady surface pressures to estimate the far field noise. This wave-number spectrum is assumed to be a function of the mean velocity gradient, the RMS velocity fluctuations and the integral length scale of the turbulence. Furthermore, it uses the von Kármán spectrum of turbulent fluctuations in the boundary layer on both sides of the airfoil. The farfield noise is calculated using this wave number, assuming that the finite thickness of the trailing edge is negligibly small and the diffraction is similar to that of an idealized semi-infinite flat plate. The general expression looks as follows:

$$S(\omega) = \frac{D}{4\pi R^2} \int_0^\infty \frac{\omega}{c_0 k_1} P(k_1, 0, \omega) dk_1 \qquad (6.22$$

In this equation, the term $P(k_1,k_3,\omega)$ represents the expression for the pressure fluctuation spectrum and is a function of several quantities in the boundary layer, it can be computed through this formula:

$$\begin{aligned} P(k_1, k_3, \omega) = 4\rho_0^2 \frac{k_1^2}{k_1^2 + k_3^2} \int_0^\infty L_2 \overline{u_2^2} \left(\frac{\partial U_1}{\partial x_2}\right)^2 \phi_{22}(k_1, k_3, \omega)\, \phi_m\big(\omega \\ - U_{1,c} k_1\big) e^{-2|k| x_2} dx_2 \end{aligned} \qquad (6.23$$

In this integral equation, *k* is the wave number vector, defined in an orthogonal space of (k_1, k_2, k_3). L_2 is the vertical turbulence length scale and is an estimation of the eddy size, furthermore, $\overline{u_2^2}$ is the root-mean-square values of the vertical velocity fluctuations. The vertical velocity fluctuation is described by the parameter ϕ_{22}. The change of this variable as a result of the generation and destruction of eddies during the convection over the trailing edge, at a convection speed U_1, is defined by the parameter φ_m. Finally, the term U_1 is the streamwise mean velocity. Its gradient along the vertical direction (x_2), perpendicular to the surface of the airfoil, is associated to wall shear. A visual representation of the TNO concept, along with the definition of the coordinate system, is shown in Figure 6.3.

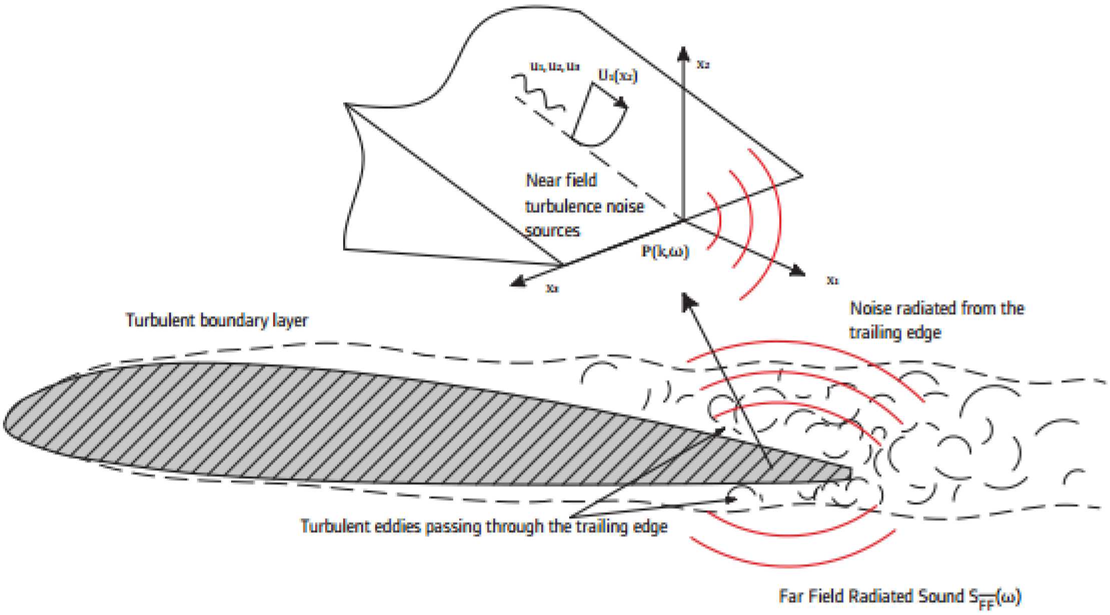

Figure 6.3: Trailing-edge noise mechanism based on the TNO model (Gasch 2014)

Now, in order to obtain the necessary information regarding the boundary layer parameters, XFOIL is used. From the tool, the variables of interest, i.e. skin friction coefficient C_f, boundary layer thickness δ, displacement thickness δ^*, and momentum thickness θ, can be extracted. Once this is done, the TNO model boundary layer properties can be computed. First, the mean velocity in the boundary layer U_1, has to be reconstructed. This is done using the Coles's law, which assumes this velocity is a linear combination of the law of the wall[1] – scaled with $y^+=u^*x_2/\nu$ – and the law of the wake[2], scaled with x_2/δ. Together they become:

$$U_1(x_2) = u^*\left(\frac{1}{\kappa}\ln\left(\frac{u^*x_2}{\nu}\right) + B + \frac{1}{2}W\left(\frac{U_0}{u^*} - \frac{1}{\kappa}\ln\left(\frac{u^*\delta}{\nu}\right) - B\right)\right) \tag{6.24}$$

Where $\kappa = 0.41$ is the Von Karman constant, $B = 5.5$ and $u^* = U_0\sqrt{C_f/2}$ being the friction velocity. This is dependent on C_f, the skin friction coefficient. Now, the wake function W can be defined as

$$W = 1 - \cos\left(\frac{\pi x_2}{\delta}\right) \tag{6.25}$$

Now that U_1 has been defined, the next term in the equation, the integral length scale L_2 of the turbulence normal to the wall will be formulated. Moriarty (Moriarty et al. 2005) used the mixing length l_m as length scales for the turbulent boundary layer.

$$l_m = 0.085\delta\tanh\left(\frac{\kappa x_2}{0.085\delta}\right) \tag{6.26}$$

Now, the integral length scale L_2 is approximated by

$$L_2 = l_m/\kappa \tag{6.27}$$

---

[1] The law of the wall states that the average velocity of a turbulent flow at a certain point is proportional to the logarithm of the distance from that point to the wall.

[2] The law of the wake defines the deviation from the logarithmic law away from the wall.

Considering a case for isotropic turbulence, the turbulence length scale can be used to estimate k_e by using the following expression

$$k_e = \frac{\sqrt{\pi}\Gamma(5/6)}{\Gamma(1/3)}\frac{1}{L_2} \approx 0.7468/\mathrm{L}_2 \tag{6.28}$$

This wave number of energy containing eddies is a necessary parameter to assess ϕ_{22}, the vertical velocity fluctuation spectrum, which is modeled by a van Karman spectrum and reads as follows:

$$\phi_{22}(k_1, k_3) = \frac{4}{9\pi k_e^2}\frac{(k_1/k_e)^2 + (k_3/k_e)^2}{[1 + (k_1/k_e)^2 + (k_1/k_e)^2]^{7/3}} \tag{6.29}$$

The other spectrum used in equation (6.23) is called the moving axis spectrum and is defined by a Gaussian distribution with the following form:

$$\phi_m(\omega - U_c k_1) = \frac{1}{\alpha_{Gauss}\sqrt{\pi}} e^{-\left[\frac{\omega - U_c k_1}{\alpha_{Gauss}}\right]^2} \tag{6.30}$$

The Gaussian constant, α_{Gauss}, is defined as a function of the eddy convection velocity, U_c, which can also be described by the boundary layer streamwise velocity, U_1.

$$\alpha_{Gauss} = 0.05\frac{c_\alpha U_1(x_2)}{L_2} \quad c_\alpha = 0.7 \tag{6.31}$$

The final quantity that has to be defined is the RMS value of the vertical velocity fluctuations, $\overline{u_2^2}$, which uses turbulent kinetic energy k_T to be calculated. Prandtl's mixing length hypothesis assumes that the turbulent viscosity v_t is related to the mixing length and the mean shear as

$$\nu_t = l_m^2\left|\frac{\partial U_1}{\partial x_2}\right| \tag{6.32}$$

Now, the turbulent kinetic energy k_T is given by:

$$k_T = \sqrt{\frac{\nu_t}{C_\mu}\left(\frac{\partial U_1}{\partial x_2}\right)^2} \tag{6.33}$$

Where C_μ=0.09. The vertical velocity fluctuations are assumed proportional to the turbulent kinetic energy as:

$$\overline{u_2^2} = \alpha_u k_T \tag{6.34}$$

Where the constant α_u is equal to 0.45 for the suction, and 0.3 pressure side, respectively. By following this procedure it is now possible to calculate all the quantities necessary to estimate the far field pressure field radiated by an airfoil according to the TNO model.

7. Validation and quality assessment of the acoustic models

The two models that have been introduced in the previous chapter will now be assessed on their ability to predict the sound level. The MatLab implementation of the BPM acoustic expressions will be used to assess the performance of this model. This way, if necessary, parameters can be varied to get a grasp of the influence they have on the sound level. The NREL tool NAFNoise is used to compute the sound level based on the TNO model. As explained, the main selection criterion is the ability of the model to properly predict the noise level. In order to check this, both models are compared with acoustic data that can be found in literature.

Though acoustic data is widely abundant in literature, the main disadvantage is that it mostly concerns acoustic data for the NACA0012 airfoil. Because the BPM model itself is based upon NACA measurements, a validation based on these measurements would be meaningless. Moreover, since the model is applied for optimization purposes, the selected model should be able to deal with other shapes than the NACA0012 as well.

Another point to note is that most of the measurements that can be found are performed at low Reynolds numbers. Since the objective of this thesis is to optimize an airfoil for a multi-MW wind turbine, the predictions made by the model should be accurate for high Reynolds numbers. Furthermore, the thickness of the considered airfoil in the measurement campaign should be in the range of a tip region airfoil (~18-21%). Ideally, the campaign also includes lift and drag polars as well as boundary layer characteristics.

A measurement campaign of the Institut für Aerodynamik und Gasdynamik (IAG) from the University of Stuttgart fulfills most of these requirements. It comprises a study to design and verify an airfoil with trailing-edge flaps for the EU UPWIND project (Lutz et al. 2011). During this study, both aerodynamic and acoustic data were acquired of the NACA 64_3-418 airfoil to serve as a reference profile for the design.

The experimental and aero-acoustic verification of the NACA airfoil, depicted in Figure 7.1 below, was done in the Laminar Wind Tunnel of the IAG. The LWT is an open return tunnel with a closed test section. The rectangular test section measures 0.73x2.73 m^2 and is 3.15 m long. First the polar measurements will be considered, the test conditions are shown in the Table 7.1 below.

Table 7.1: Measurement conditions for the IAG measurement campaign

Measurement conditions	
Airfoil	NACA 64_3-418
Reynolds number	$2.5 \cdot 10^6$
Chord length [m]	0.6
Free stream velocity [m/s]	70
Mach number [-]	0.197
Span [m]	0.73
Acoustic source-receiver distance [m]	1.0

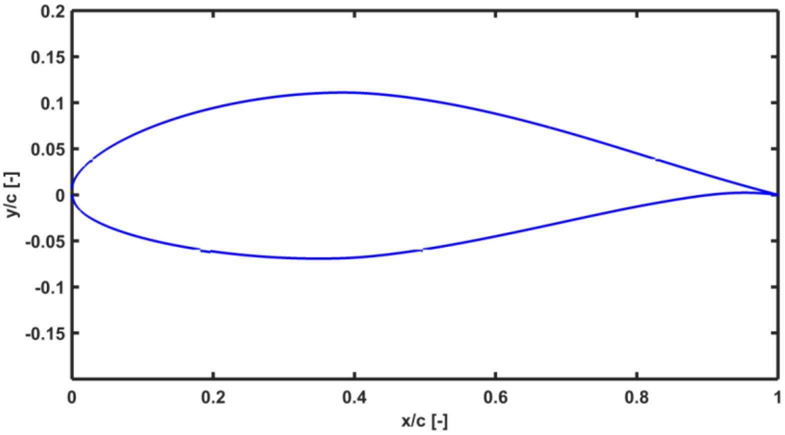

Figure 7.1: shape of the NACA 64_3–418 airfoil

7.1. Aerodynamic measurements

In order to determine the quality of the facility as well as the polar predictions made by RFOIL, the lift and drag measurements will be considered. The lift is determined by experimental integration of the pressure distribution along the opposite two tunnel walls. The difference of both averaged pressures is proportional to the lift. The drag is determined by an integrating wake rake, which is positioned approximately 0.45 chord length behind the model trailing edge. For the tests a rake with a width of 120 mm was used. During the measurements the wake rake is traversed in spanwise direction and a mean value for the drag is calculated. In the Figure 7.2 below a comparison between the RFOIL/XFOIL predictions and the measurements can be found.

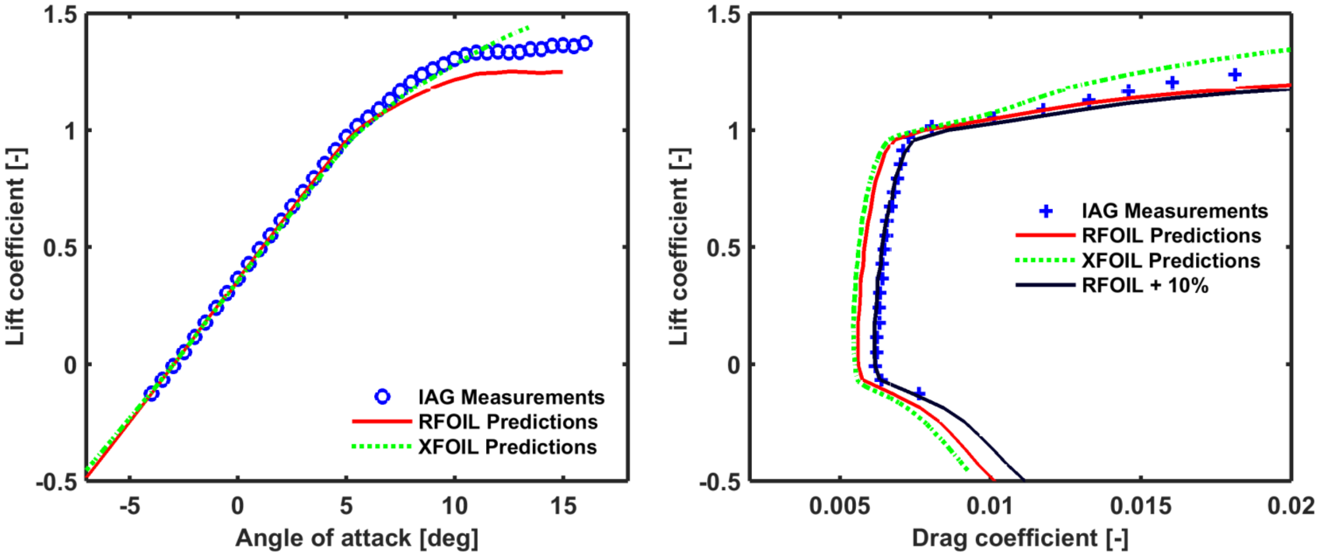

Figure 7.2: comparison of measured and predicted lift polar (left) and drag bucket (right) for untripped conditions at Re = 2.5 million and Ma = 0.197

What can be noticed from the figures is that the NACA 64_3-418 airfoil has a moderate maximum lift coefficient and a soft post-stall behavior. Furthermore, considering the RFOIL predictions, it is accurate until about 7 degrees, after that the lift coefficient starts to deviate. Especially around the maximum lift coefficient the stall behavior is under predicted. XFOIL performs better in this respect. However, the disadvantage of this tool is that XFOIL is unable to reach convergence after 11.5°, something which is an undesirable feature from an optimization perspective.

An evaluation of the drag coefficient shows that both XFOIL and RFOIL systematically under predict this quantity, even at angles below stall. This is why, as suggested by Van Rooij, a 10% drag increase is imposed upon the predictions made by RFOIL (Van Rooij 1996). The effect of this can also be seen in the figure; the calculations now correspond better with the measurements as a result of this modification.

7.2. Acoustic measurements

Unlike most aero-acoustic airfoil measurement campaigns, the LWT does not make use of an acoustic microphone array for the sound level measurements. Instead, a different approach is used to find the trailing-edge noise levels. The method is mainly used in wind tunnels with high background noise. It is based on the measurements of two hot-wire signals, allowing to derive the cross correlation of the Coherent Particle Velocity (CPV) of the emitted sound waves (Herrig et al. 2006). These velocity fluctuations are then converted to sound pressures assuming acoustic sources of monopole type located at the trailing edge. From the phase of the cross-correlation function it is possible to make a distinction between trailing-edge and background noise. The method was validated against microphone acoustic experiments performed on a NACA0012 airfoil in NLR's KAT wind tunnel and data measured at NASA. A good agreement between the measurements is found.

The acoustic measurements on the NACA 64_3-418 airfoil were performed at angles of attack between -6 and 6 degrees. The results, along with the predictions made by both the TNO and the BPM model, can be found in the figures below.

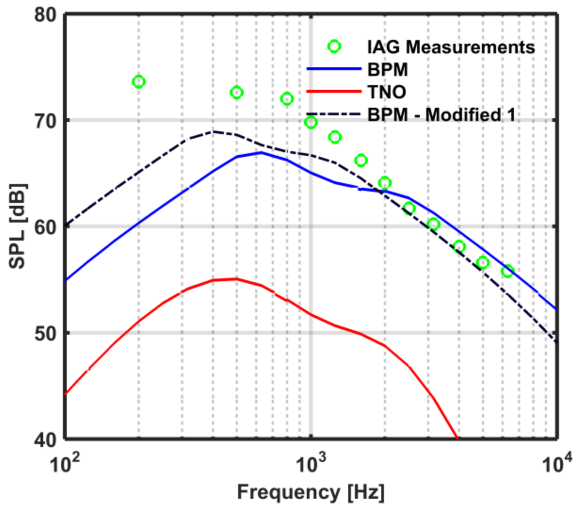

a) α = −6 degrees

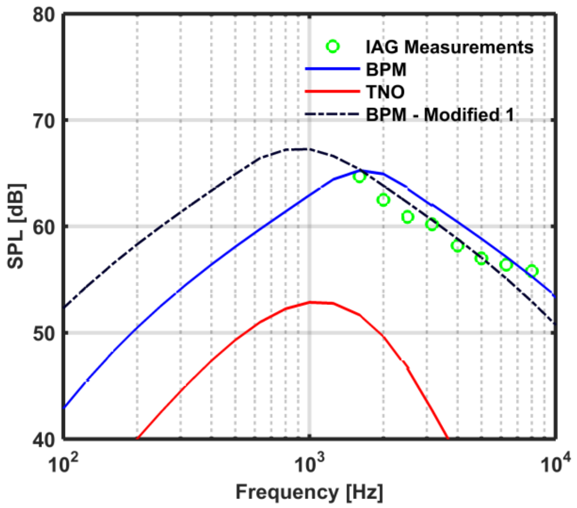

b) α = −3 degrees

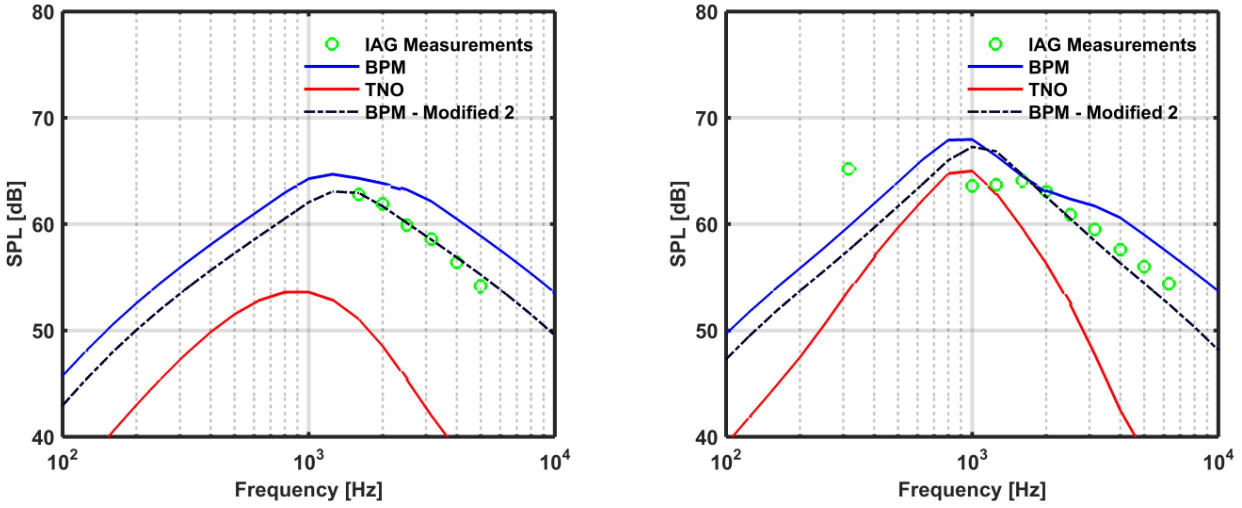

c) α = 0 degrees

d) α = 3 degrees

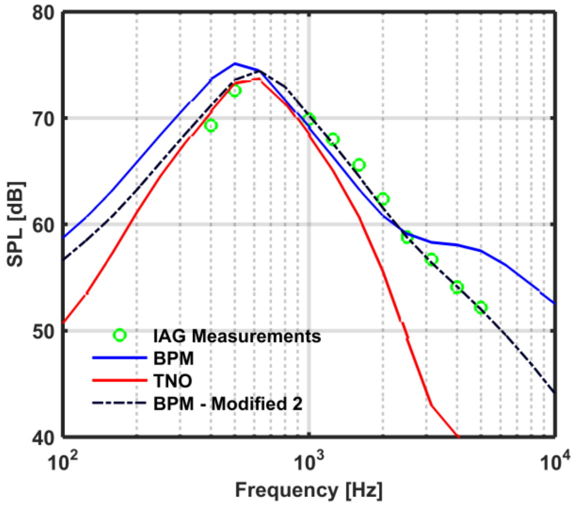

e) α = 6 degrees

Figure 7.3: comparison of acoustic measurements and predictions with different models for various angles of attack

First, the results of the unmodified versions of both the TNO and the BPM models will be assessed. What can be observed is that for negative and zero angle of attack the TNO model performs poorly and neither matches the shape nor the order of magnitude of the measurements. For positive angles this is slightly better but still not satisfactory. The order of magnitude of the predictions is better but the shape is still off. Concerning the BPM model: for an angle of minus 6 degrees the predictions, especially for the lower frequencies, do not match the IAG CPV results. For the other angles, the performance is better but the shape does not fit the measurements. In the BPM estimation the curve shows a ‘shoulder’ for high frequencies, which is not visible in the measurements.

Since both models do not present results with satisfactory accuracy, the decision is made to look for a trade-off between trailing edge noise contributions which best matches the measurements. Since the TNO model is computed by NAFNoise and provides no options to adjust any input parameters, this is exclusively done for the BPM model. The outcome is also shown in Figure 7.3 using the additions ‘modified’. The model is divided into two cases, case one comprises the negative angles, while case 2 contains zero and positive angles.

The analysis comprises of increasing/decreasing the boundary layer displacement thickness as input to the model. Furthermore, it was checked which combination of the three BPM noise contributions, $SPL_{s,}$ SPL_p and SPL_α, gives the closest match. It is found that no combination of noise contributions is able to match the predictions and measurements at minus 6 and minus 3 degrees perfectly. Ultimately, the pressure side and suction side contribution combined provides the best fit, the separation contribution is left out. Furthermore, the displacement thickness was also adjusted, in order to modify the height and frequency of the peak. The best match is found for an increase of the lower side δ^* of 50%, and a multiplication of two for the upper side.

For case 2, the same steps are followed to find the best fit for positive angles of attack. As is the case for negative angles, no combination of settings can be found such that the predictions match the measurements entirely. The configuration of noise sources that yield the best fit comprises of the separation and suction side contributions. The pressure side is responsible for the ‘shoulder’ in the BPM prediction, since this is not present in the measurements, this noise contribution is left out. Furthermore, the displacement thickness is reduced by 15%. This combination of settings yields the closest fit; both the shape of the curve and the order of measurements closely resemble each other. In Appendix E, the modified BPM acoustic model is compared to measurements done in a different measurement campaign, based on other operating conditions and two other airfoils. This is done to check whether the chosen settings are not solely applicable to this particular situation.

Ultimately, for the optimization performed in the next chapters, the BPM method with the mentioned modification is used for the acoustic model. Because both the standard BPM and the TNO model fails to deliver the desired accuracy.

8. Airfoil parameterization

In order to analyze the aerodynamic and acoustic performance of an airfoil, it is necessary to model the geometry. The model should have as few input parameters as possible but should be able to produce airfoil shapes with good accuracy.

There are several methods to represent an airfoil shape. In the thesis of Grasso (Grasso 2008), some of them are presented (Hicks-Henne functions, Legendre function, spline curves and Bézier curves) and discusses the advantages and disadvantages. A more recent method, applied by e.g. Risø, Non-Uniform Rational B-Spline (NURBS) curves.

The thesis of De Oliveira (De Oliveira 2011) contains a table were each of the well-known parameterization methods are compared. The method adopted is the Class Shape Transformation (CST) parameterization by Kulfan (Kulfan 2008). This is because it can cover most of the design space with only a few parameters very efficiently and accurately.

The CST parameterization uses a product of two functions to define the airfoil shape, a class C(x) and a shape S(x), summed with a function to construct a trailing edge thickness z(x). The basic formulation is shown below.

$$t = S(x) \cdot C(x) + z(x) \tag{8.1}$$

Each side of the airfoil has to be modeled separately, so one will define the upper and the other one will form the lower side of the airfoil. The class function defines the basic shape, and the shape function is used to perturb this function, thereby defining the design.

8.1. The class function

The class function is a simple analytical function that provides the essential properties of an airfoil. It is defined by the equation below:

$$C(x) = (1 - x)\sqrt{x} \tag{8.2}$$

This function has some useful properties that can help to generate airfoil shapes. Some of these properties of the class function are:

- The airfoil has an infinite derivative at the origin, to define the leading edge
- The airfoil has a finite curvature at the origin
- The value at the trailing edge goes to zero
- It has a single extreme in the [0,1] interval

8.2. The shape function

The shape function is multiplied by the class function and is used to perturb the class function, thereby giving it its shape. In the CST method presented by Kulfan, the shape function is a weighted sum of Bernstein polynomials. One of the useful features of these polynomials is, is that it takes a unit value over its entire domain, when all parameters are equal to one.

The Bernstein polynomials $s_{(x)}^{rN}$ are the basis for generating the shape function S(x), they are weighted by a linear combination of coefficients $b_{n.}$ the basic formulation is:

$$S(x) = \sum_{r=0}^{r=N-1} s_{(x)}^{rN} \cdot b_n \qquad \begin{cases} x \in [0,1] \subset \mathbb{R} \\ \quad b_n \in \ \mathbb{R}^n \end{cases} \tag{8.3}$$

Here, b_n is the tensor holding the linear combination coefficients. The basic functions holding the complete set of Bernstein polynomials of order N, are given as:

$$s_{(x)}^{rN} = \binom{N-1}{r} x^r (1-x)^{N-1-r} \qquad \begin{cases} r \in [0, N-1] \subset \mathbb{Z} \\ \binom{n}{r} = \dfrac{n!}{r!\,(n-r)!} \end{cases} \tag{8.4}$$

It can be seen that, although order of the polynomials is N, the highest degree is N-1. So for a polynomial order of 5, the highest power of the equations is 4. Below an example of a fifth order shape function can be found, along with the associated formulas.

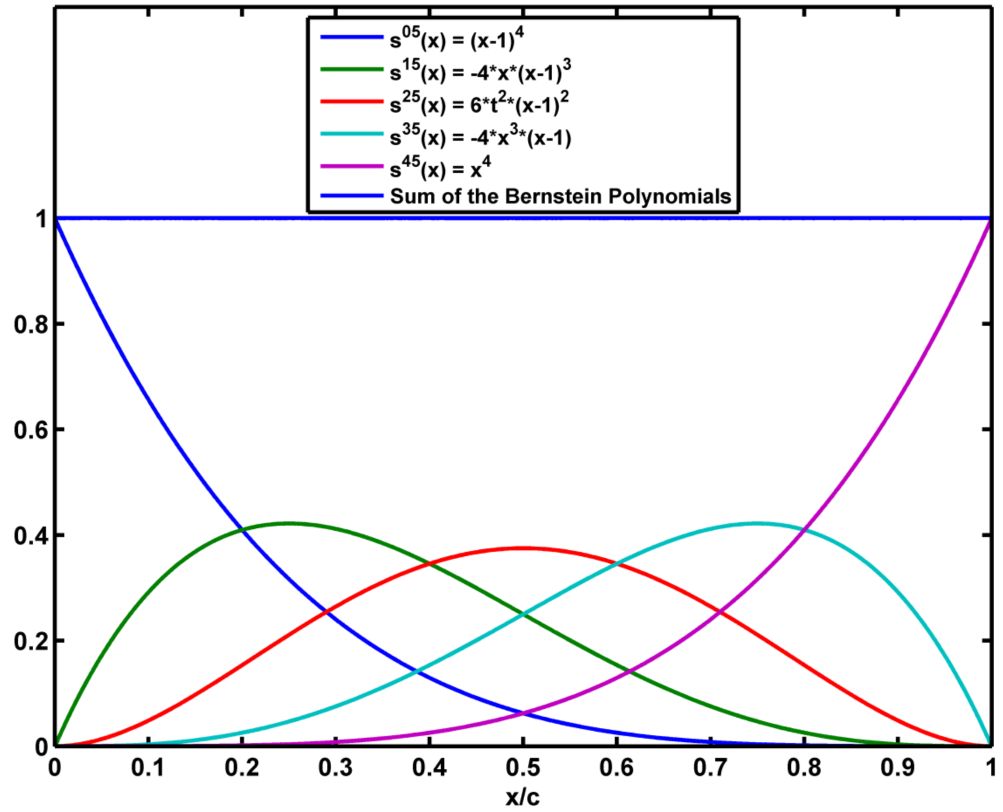

Figure 8.1: set of Bernstein polynomials of order 5 and degree 4

In the case of the figure above, the coefficients were set as unity and the sum of the polynomials are unity for all values of x.

8.3. Trailing edge thickness function

As can be seen in equation (8.1), the trailing edge thickness function is added to the production of the class function with the shape function, in order to be able to construct blunt trailing edges. Any function or constant can be used provided is satisfies these three conditions:

- It is zero at the leading edge
- Its value at the trailing edge is the trailing edge thickness on that side.
- The shape of the function introduces the least possible perturbations on the airfoil shape

8.4. Bernstein Polynomial Order

Selecting the Bernstein Polynomial Order (BPO) of the equations is a choice that directly affects the ability to (re)construct (existing) airfoil shapes. On one hand, the higher the polynomial order, the higher the accuracy. On the other hand, this also increases the computational time and thereby the simulation time as well.

In the MSc. thesis of De Oliveira (De Oliveira 2011), an analysis was made to determine a suitable BPO for optimization purposes. This sensitivity analysis was done to three existing airfoils and it seemed a BPO of 6 to 8 is sufficient for the airfoils to overlap perfectly visually. However, in order to obtain an objective measurement of performance of the CST parameterization capabilities the analysis was extended to quantify the errors. The maximum relative distance between the fitted and the original shape was now set as an objective measure. The general trend is, as one would expect, that the error decreases as the BPO increases.

The result of the analysis was that a BPO of 10 or 8 seems sufficient to cover the design space effectively, corresponding to a set of 21 parameters describing the airfoil shape, 10 for the upper side, 10 for the lower side and one for the trailing edge. To quantify the errors for multiple airfoils, a fit was performed on several shapes with a BPO-10 on the upper side and a BPO-8 on the lower one. The order of magnitude of the maximum relative error is about ~$3*10^{-4}$ and the max L/D error is about 1%.

To determine the influence of the BPO on the quality of the solutions, a small optimization was performed in the report (De Oliveira 2011). Since the shape created in a lower BPO can also be generated in a higher BPO, the optimal airfoil performance should grow monotonously with parametrization order. If this is not the case, the optimization process did not converge completely. The result of this analysis can be observed in the following Figure 8.2.

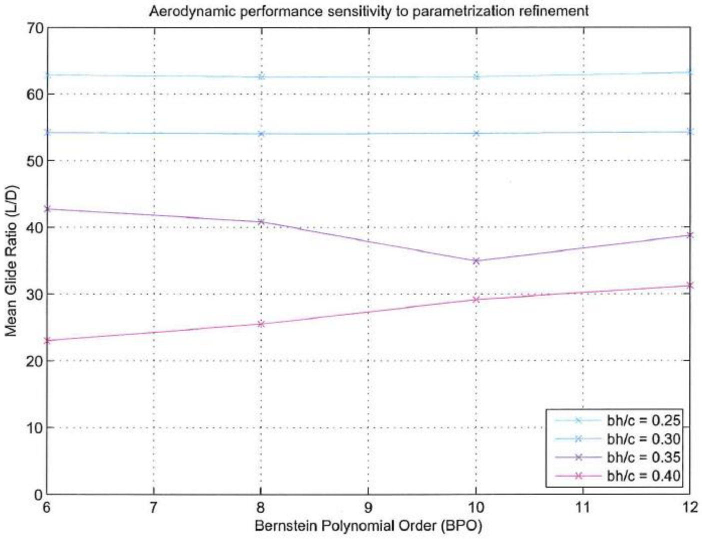

Figure 8.2: Variation of optimal aerodynamic performance to parametrization order for various building heights (De Oliveira 2011)

The figure shows that for a lower building height (below 35% thickness), the aerodynamic performance is insensitive to the BPO. The results of the design of an airfoil with a thickness smaller or equal than 30% would therefore not be increasing with a higher BPO.

Combining the statements regarding the polynomial order made above, the most suitable combination appears to be a BPO-10 to the upper, and 8 to the lower side to the CST parameterization. This is seems a good trade-off between covering the design space thoroughly and still converging towards a solution within a reasonable amount of time. However, other factors, to be eluded on in later chapters, affect the choice of the order as well.

8.1. Fitting existing airfoils

To show that the CST parameterization is an appropriate method for parameterizing airfoil shapes, it is necessary to apply a fit to some existing airfoils. The selected airfoils are the DU93-W-210, FFA-W330 and the S809 profile. Their shapes along with a BPO-8 CST approximation can be found in the figures below.

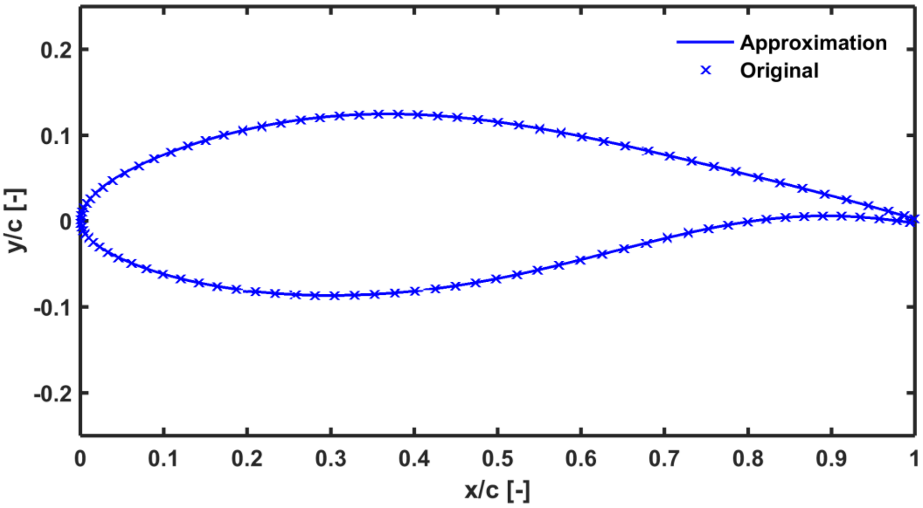

Figure 8.3: Fit of the DU93-W-210 airfoil

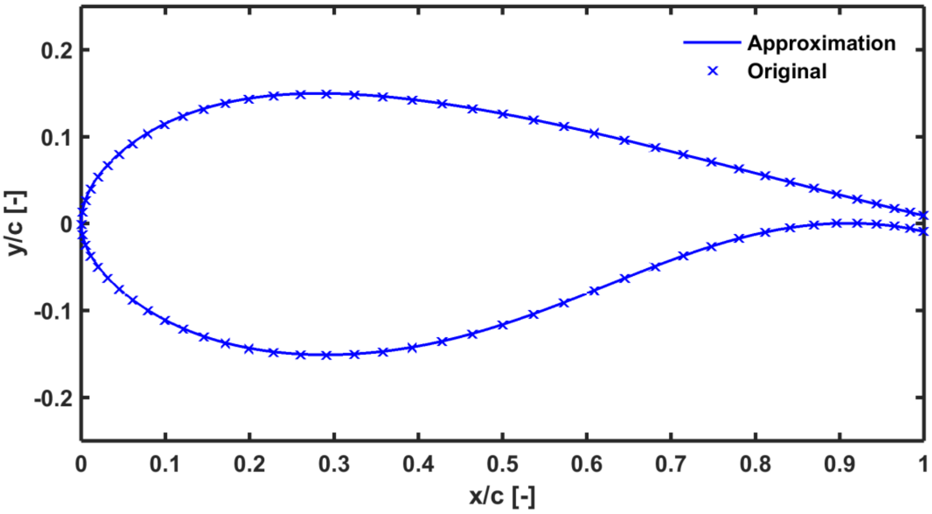

Figure 8.4: fit of the FFA-W330 airfoil

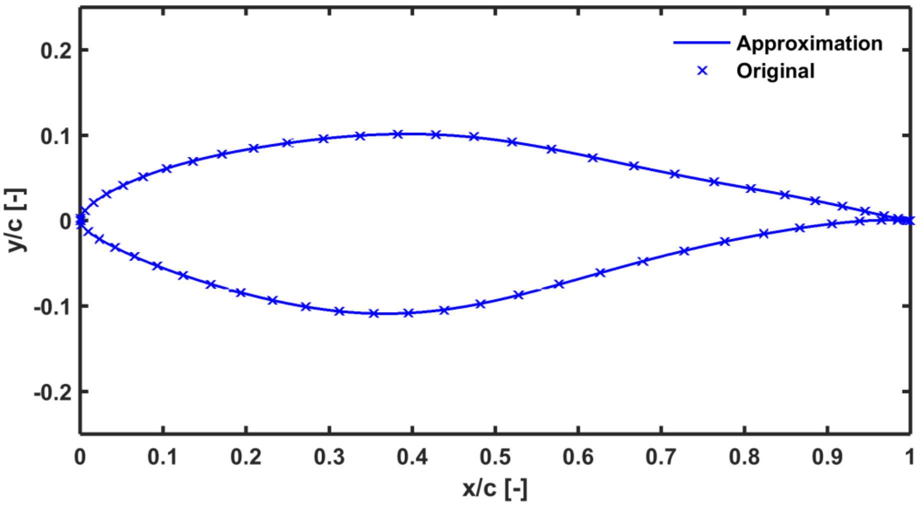

Figure 8.5: fit of the S809 airfoil

From the figures, it can be seen that the CST representation can fit the airfoils with good (visual) accuracy. Note, the figures above are merely to illustrate the capability of the CST parameterization to recreate existing airfoil shapes, not to quantify the maximum relative error. The analysis described in the previous section is used for this.

9. Optimization

To introduce the subject of optimization, first a general description will be given. An optimization procedure starts with defining a cost function (the *objective* function), which depends on a set of *design variables* and restrictions (*constraints*). In other words, the procedure is to optimize for the cost function by varying the design variables while satisfying the constraints. Generally, the cost function is composed in such a way that it can be *minimized*. The mathematical description is as follows

$$\begin{array}{lll} minimize & f(x) & \\ by\ varying & x \in \mathbb{R}^n & \\ subject\ to & g_j(x) \leq 0, & j = 1,2, \dots, M \\ & h_k(x) = 0, & k = 1,2, \dots, L \\ & x_i^L \leq x_i \leq x_i^U, & i = 1,2, \dots, N \end{array} \tag{9.1}$$

Where f(x) is the objective function for a set of *N* design variables x_i. The design variables x_i are bounded by the lower and upper boundary that set the search space, called side constraints. Furthermore, it also has to fulfill *M* inequality and *L* equality constraints, given by vectors g_j and h_k. These boundaries and constraints define the search space in which a solution to the minimization problem has to be found.

Since this research focuses on two competing objectives (noise emission versus aerodynamic performance), it requires a multi-objective optimization strategy. A simple means of formulating the objective function now is to apply the weighted-sum method. A single objective is now formed by a weighted sum of the competing objectives. By varying the weights, the emphasis can be put on either goal. The solution of a set of weightings will result in a point on the so-called *Pareto* front. The Pareto optimal set is the set of solutions that are non-dominated by any other member of the total set of feasible solutions. The Pareto front provides a set of solutions of interest to the designer and reveals tradeoffs between objectives (Zingg et al. 2008).

There are generally two main numerical optimization algorithms available, one being deterministic (gradient-based) and one being heuristic (genetic-based). Both have their advantages and disadvantages and in the following section both will be outlined shortly. Based upon this information one of the methods will be selected to perform the optimization problem addressed in this thesis.

9.1. Gradient-based algorithms

This is the most common and generally known optimization techniques. As the name suggests, as Gradient Based Algorithm (GBA) uses the gradient of the objective function to find an optimal solution. Each iteration of the optimization algorithm adjusts the values of the decision variables in such a way that they produce a lower objective function value. The adjustment is proportional to the reduction in the objective function value. Gradient-based searches are prone to converging towards local minima because they rely solely on the local values of the objective function in the search. The final solution of the method is very dependent on the initial conditions and it therefore is best used in well-behaved systems where there is one clear optimum. The method will only be usable if the problem is the number of local minima is few, otherwise the search routine could be trapped into converging towards a local optimum rather than a global one.

9.2. Genetic-based algorithms

Genetic-based algorithm (GA) is a heuristic search method, based upon the principles of natural selection and evolution. The algorithm uses the idea of survival of the fittest by Darwin to come to a solution. In nature, weak and unfit species within their environment are faced with extinction by natural selection. The strong ones have greater opportunity to pass their genes to future generations via reproduction. In the long run, species carrying the correct combination in their genes become dominant. Sometimes, during the process of evolution, random changes may occur in genes. If the changes provide additional advantages in the challenge for survival, new species evolve from the old ones. Unsuccessful ones are eliminated by natural selection.

As is the case in biology, the optimization process used the same principle and therefore has a comparable terminology: a *gene* is a design variable, an *individual* or *organism* is a candidate solution obtained from a set of design variables and a *population* consists of a group of individuals. Successive populations are called *generations*. The generic algorithm can be described as follows:

1. Generate initial population G(0)
2. While termination criteria not satisfied, continue search for t=t+1
3. Select G(t)
4. Recombine G(t)
5. Evaluate G(t)
6. Return to 2

The setting of the initial population marks the beginning of the search. The initial population is a random selection of candidates within the search space. This selection is then subjected to a series of operations, in order to generate the following generations. These operations consist of the following:

Selection: This operation selects the best n individuals (based on objective functions) which show the best performance and have a higher chance of positively contributing to the next generation. These individual will be subjected to the next step, crossover;

Crossover: process that combines the genes of both parents to generate a number of children which each inherit a part of both the genes.

Mutation: every crossover will have a small chance of introducing a mutation which serves to increase the variability of the population. This is done by randomly changing a gene of an individual within the allowed range.

Insertion: the children are now inserted to into the new population.

This process is repeated until the stopping criterion is met, this can be a specified number of generations or any other specific criterion, a schematic overview can be found in the figure below.

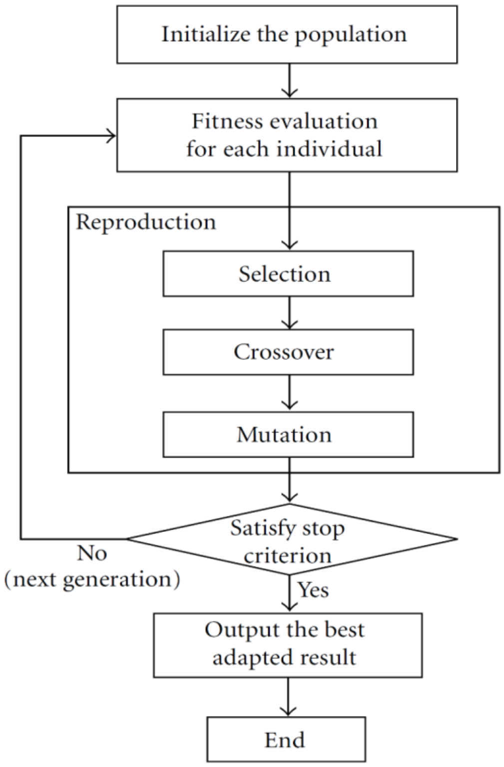

Figure 9.1: Flowchart of the GA reproduction process (Chen et al. 2009)

Although GBA are more accurate, the GA will be used for the optimization process. The main reason of this choice is the capability to explore wide, non-linear and discontinuous domains and be less sensitive to the initial configuration.

10. Optimization framework

In this section the various aspects of optimization process will be outlined. First, a general outline of the optimizer will be given. The main objects, classes and functions and their relation with respect to each other is pointed out. In the sections that follow, other important conditions that influence the outcome of the optimization will be elaborated on. These consist of the constraints that are applied, the population size and the number of generations that are used, and criteria when convergence has been reached. Then, the evaluation functions that rate the airfoils based on aerodynamic and acoustic properties are described.

10.1. General outline of the optimizer

The optimizer used in this optimization makes use of the MatLab computing environment. And the main foundation was laid by De Oliveira (De Oliveira 2011). The code uses an object-oriented data structure and relies on several MatLab toolboxes, such as the Symbolic, the Spline and Global Optimization Toolboxes.

The program consists of several objects, each with a different task within the optimization process. Below a list with the objects and the task it performs is given:

- *System context* – generates the context in which the program has to operate. It manages the file paths and directories as well as the interaction with the operating system and hardware.
- *Parameterization* – relies on the symbolic toolbox of MatLab to perform the math behind the formulation of the CST parameterization, as described in chapter 8. It also precomputes all the matrices and expressions necessary to describe and fit airfoils, which is done in other objects.
- *Shape definition* – stores and uses all information about the airfoil shape, using the two parameterization objects, one for each side of the airfoil.
- *Shape fit* – its job is to fit existing airfoils (coordinate files) using the information of the shape definition and parameterization objects into a list of Bernstein Polynomial coefficients.
- *Simulation protocol* – uses the simulation preferences and specifications to create a file command file for RFOIL.
- *Simulation worker* – actually executes the simulations in RFOIL, following the instructions by the *simulation protocol* object.
- *Cost function* – the results of the simulations are loaded into MatLab and interpreted using interpretation functions. The *cost function*'s role is to provide an interface between the optimization framework and the interpretation functions.
- *Global cost function* is used to create a multi-objective cost function from the single objective cost functions defined through the *cost function* objects. It also manages which simulation results go to which interpretation function.
- *Constraint manager* – uses the shape fit object to construct boundaries from a database of airfoils (see section 10.2).
- *Gamultiobj_manager* sets up and controls execution of the optimization algorithm.

Below, a schematic of this process can be seen.

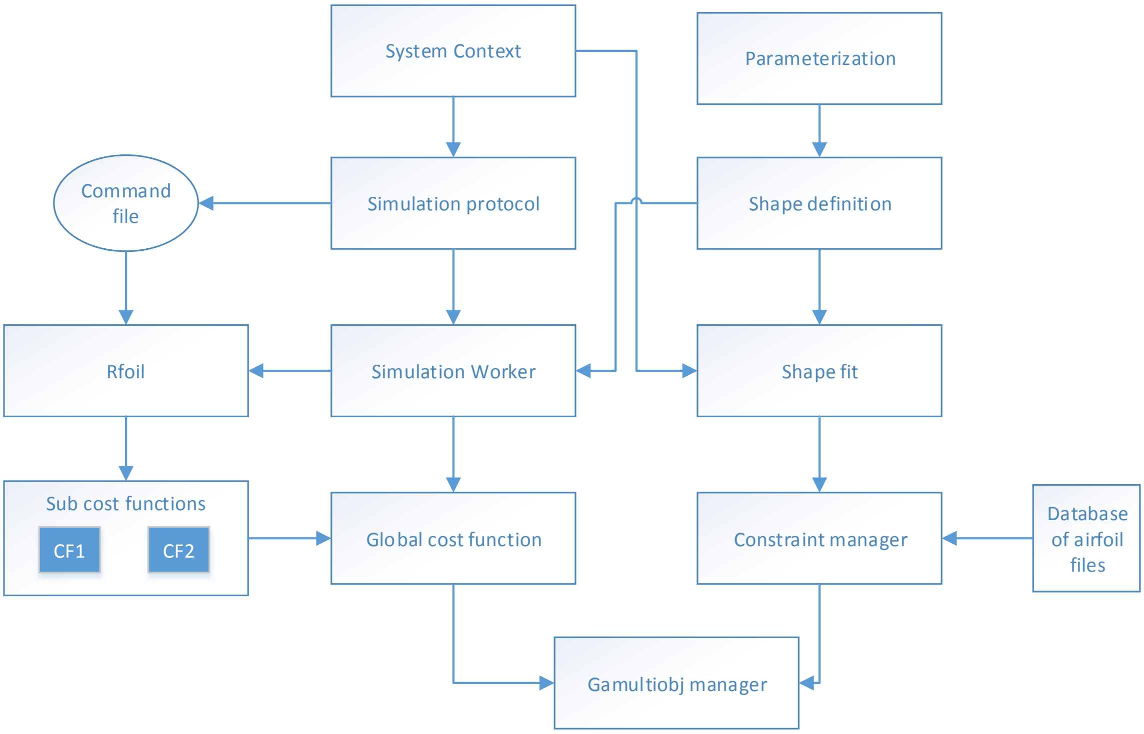

Figure 10.1: schematic of the various objects of the optimizer and their interconnections

10.2. Constraint manager

The success of an optimization lies in defining the boundaries of the design space. For the initial population, the optimizer will try to populate the design space relatively evenly with some focus on the boundaries. The challenge of defining boundaries lies in making them wide enough to encompass the global optimum and making them small enough for the optimizer to converge without stalling in reasonable time.

This so-called algorithmic stall occurs when the improvements of the next generation compared to the previous one are very limited to non-existent, even though convergence has not been reached. Although it cannot entirely be prevented, the chance of occurrence can be limited by some settings. Using a large population size as well as a high mutation rate can partially prevent it. Furthermore, the chance can be minimized by the use of distance crowding strategies.

To define the boundaries of the design space, a shape fit routine was used. In this way, a collection of existing airfoils is used to easily cover a realistic search space. This was done by fitting the database of wind turbine airfoils, by means of the shape fit routine briefly described above. The minimum and maximum boundaries were found by selecting the minimum and maximum value in each chordwise x-parameter:

$$lb_i^{ref} = \min\left(x_i^{fit}\right) \quad , \quad ub_i^{ref} = \max\left(x_i^{fit}\right) \quad , \quad i = i \dots q \tag{10.1}$$

Where the parameters lb and ub represent the lower and upper boundaries, respectively. The advantage is that this approach leads to a realistic search space but has the limitation that it only includes coordinates within the range of airfoils of the database. Airfoils that are present in the database range from thick inboard, to thinner outer region profiles. This limitation would result in the fact that it is not possible to develop airfoils that are thicker than the thickest or thinner than the thinnest. The solution to this is a strategy to extend the boundaries by a certain factor, in the following way:

1. Boundary expansion factors can be defined for three chordwise regions of the airfoil: leading edge, middle part and trailing edge. This strategy allows for quite flexible boundaries, without extending the design space too much into unfeasible regions.

2. The centroid of the existing airfoil design space is found:

$$\bar{x}_i = \frac{1}{p}\sum_{i=1}^{p} x_i^{fit} \tag{10.2}$$

3. An expansion ratio r_i is defined for each parameter by assigning it a chordwise position, given by the location of the maximum of the corresponding Bernstein Polynomial Order *n*:

$$({}^{x}/{}_{c})_i^{max} = \frac{i-1}{n-1} \tag{10.3}$$

   And interpolating the user supplied bound expansion factor in the chordwise coordinate.

4. The boundaries are expanded linearly outward from the centroid by the factor r_i in the following way:

$$ub_i^{ref} = \bar{x}_i - r_i(\bar{x}_i - r_i(\bar{x}_i - lb_i^{ref}) \tag{10.4}$$

This approach is very easy, user friendly and provides quick feasible boundaries. Within the optimizer, this all is done by the constraint manager object. The only major drawback that follows from using this approach is that the boundaries are dependent on the BPO. The boundaries are expanded more for higher order parameterizations than for lower ones. If one applies a different parametrization order to one of the airfoil sides, the expansion factors has to be changed as well.

In the Figure 10.2 below one can see how the boundaries defined by the airfoil database are extended in order to expand the design space for a BPO of 6.

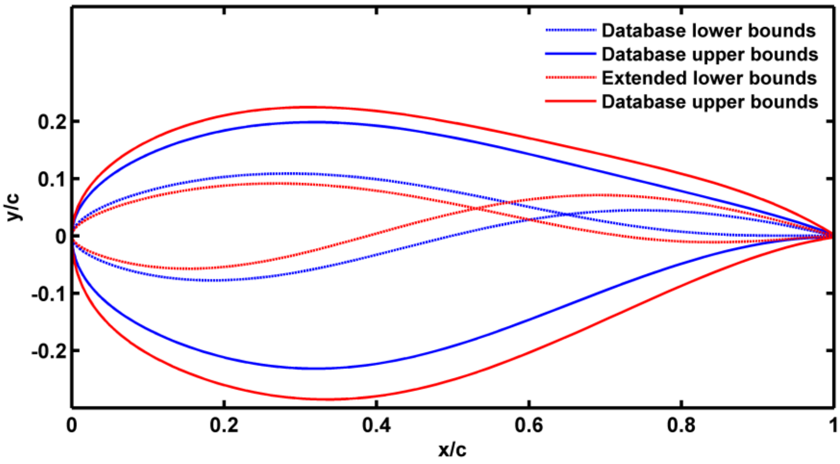

Figure 10.2: upper and lower boundaries for BPO6

In the next Figure 10.3 the shaded cyan colored area indicates the feasible region for both the upper and lower side of the airfoil. The dark blue area represents the region where both upper and lower side coordinates can be generated.

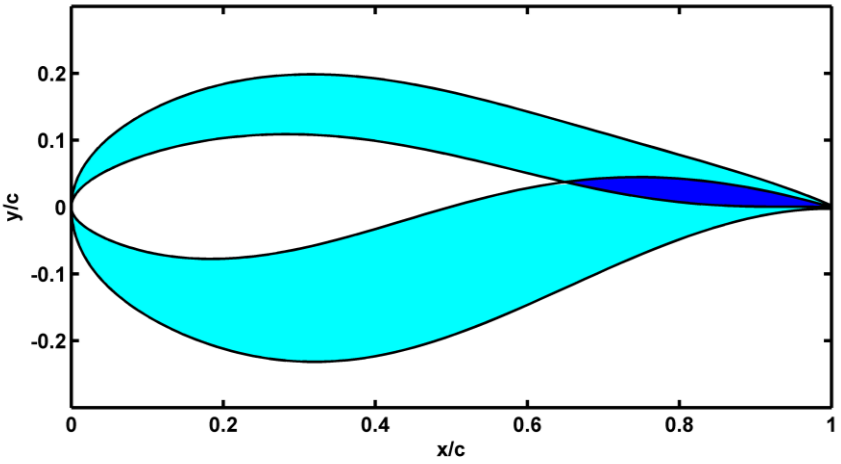

Figure 10.3: feasible regions for the upper and lower side

10.3. Population size and number of generations

The NSGA-II multi-objective solver in MatLab has two criteria that force the optimizer to stop. The optimization process finishes if either the maximum number of generations is reached or if the improvements in the non-dominated set of solutions become smaller than a certain tolerance. Whichever of the criteria is met first. The choice of these settings can have a big impact on the computational time to reach a final solution set.

Increasing the maximum number of generations will increase the chance that the final solution set has converged, but will obviously also increase the computational time spent on the optimization. Increasing the population size might reduce the number of generations required to achieve convergence, but can also lead to a very time consuming optimization. The choice of both these two settings should therefore be done carefully. Entire studies have been devoted to the subject. Researchers that have contributed to this subject are Alander (Alander 1992) and Gotshall & Rylander (Gotshall & Rylander 2008).

It turned out to be very difficult to provide a general answer to this question and it is found that each problem should be analyzed individually. In the thesis of De Oliveira (De Oliveira 2011), a general rule of thumb was established after a brief analysis to find the population size is:

$$Pop_{size} = (10n)^{m-1} \tag{10.5}$$

In this relation, *m* is the number of objectives in the optimization and *n* the number of variables. As can be seen, for optimization cases with more than one objective, the population size grows very rapidly, resulting in very high computational requirements. This optimization problem comprises of two objectives and the number of variables is two times the BPO. A BPO between 8 to10 will therefore lead to population size of approximately 160-200 individuals. A maximum number of generations of 50 will already give a good indication of where the Pareto front will be situated.

10.4. Convergence of a multi-objective optimization

Showing convergence for a multi-objective optimization problem is not a straightforward matter, for they do not result in a single solution but in a set of optimum solutions. It is also known that, for single objective optimization, the quality of the solution in the initial phases improves rapidly, whereas in later stages the improvements become incremental. This phenomenon is amplified for a multi-objective optimization.

A clear definition of the point of convergence would be beneficial, since it could be used as a stopping criterion for the optimization algorithm. One can terminate the GA search once a reasonable improvement are obtained, thus saving significant computational costs to converge to the global optimum solution. This paragraph will briefly touch upon some measures to indicate convergence. Not to include as a stopping criterion, but to establish if the set of solutions obtained in the final optimization in this thesis, has converged sufficiently.

In literature, entire studies have been devoted to the subject. Goel & Stander (Goel & Stander 2010) provide a clear insight in the most commonly used measures of convergence. In the paper, several performance metrics based on two analytical benchmark problems and two engineering problems are tested. For the two analytical problems, the analytical solution is known beforehand and it can very accurately be determined how close the solution set approaches this, for the engineering problem, this is not the case. The performance metrics assessed are:

1) **Convergence to Pareto optimal front** – to compare the sets of non-dominated solutions between various generations, the number of solutions that are dominated in each set is computed using a weak domination criterion. The smaller the number of dominated solutions, the better the convergence.

2) **Diversity**- the diversity of the Pareto front estimates how wide-spread the solutions are, one of these estimates is the spread.

3) **Stopping criterion** – these two measures are proposed criteria in the paper and compared to the other ones mentioned. The approach suggested is to keep an external archive of non-dominated solutions and update this archive after each generation. The updates consist of the removal of solutions that are dominated by the new evolved solutions and to add the new solutions that are also non-dominated with respect to the new archive. With these updates, the following steps have to be taken to compute the two criteria mentioned below. First, the archive at a generation is compared with an older generation. Then the number of solutions in the old archive that were dominated (dominated solutions) by the newer archive and the number of older archive members that are also present in the new archive (non-dominated solutions) are computed. The number of dominated solutions and non-dominated solutions are scaled by the size of the archive to be able to compare them fairly. Now the two criteria can be defined:
    a) Consolidation ratio: the scaled number of non-dominated solutions. It represents the proportion of potentially converged solutions.
    b) Improvement ratio: the scaled number of dominated solutions in the archive. This is an indication of the quality of the solutions.

In the figure below, an example can be found of development of these two ratios as a function of the number of progressed generations.

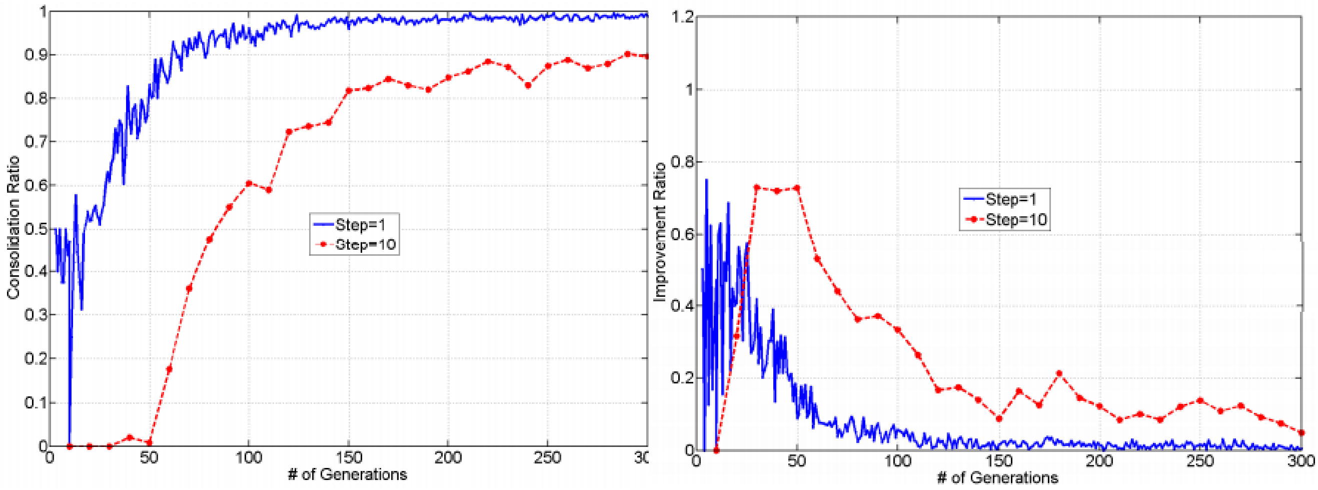

Figure 10.4: consolidation ratio (L) and improvement ratio (R); (Goel & Stander 2010)

As can be seen in both plots, the consolidation ratio tends to converge towards unity, and the improvement ratio towards a value of zero. Furthermore, in order to reduce the amount of noise the step size between two generations can be increased. This does however changes the convergence limit, which is important if one were to use it as a stopping criterion. Since the purpose of this section is to evaluate the level of convergence, this is not an issue.

10.5. Objective functions

For the aero-acoustic airfoil optimization two interpretation functions were used to obtain airfoils that perform well both aerodynamically and acoustically. The simulation protocol object generates a command file with the user's simulation preferences contained and the simulation worker instructs RFOIL to perform the calculations. These data are then evaluated by the cost functions in order to grade the performance of the airfoil. The following section will describe how the airfoil is rated on both objectives, point out why this criterion is taken and outline how this score is computed.

10.5.1. Aerodynamic cost function

The aerodynamic cost function rates the airfoil generated by the Shape definition object based on its aerodynamic properties. Desirable airfoil characteristics form a complex matrix of properties and some are in conflict with others. Before the routine the cost function applies is outlined, first the basic airfoil design goals are established.

Generally, there has been consensus in literature such as Timmer & van Rooij (Timmer & van Rooij 2003) and Bak (Bak et al. 2014) on the desirable characteristics on aerodynamic requirements. However, the means of achieving them depend on both the designer and the design method.

A high lift-drag ratio is considered to be desirable in virtually all aerodynamic airfoil design studies and is often used as the main design driver. Another aerodynamic performance related quality would be the magnitude of the C_l of maximum lift-drag ratio (the design C_l). For outboard airfoils on pitch regulated wind turbines this is relatively unimportant (Timmer & van Rooij 2003). This means that, within a certain tolerance, deviations from the desired $C_{l,des}$ are allowed. More important is the difference between the maximum lift coefficient, $C_{l,max}$, and $C_{l,des}$. This must not be too large to prevent excessive loads in case of gusts and not too small to prevent the rotor from stalling when the pitch controller cannot respond fast enough to a sudden change in wind speed. Ideally, the slope between $C_{l,des}$ and $C_{l,max}$ decreases, to avoid an unnecessary and undesirable increase in the blade loads. This would result in the upscaling of several wind turbine dimensions, which in turn results in higher turbine costs. Similar statements can be made considering the stall angle of attack and the design angle of attack: the difference in between α_{des} and α_{stall} should be sufficiently large.

To capture this desired aerodynamic behavior in an aerodynamic cost function they were converted in a set of requirements. The cost function works by computing the weighted average of this list of aerodynamic requirements. The contribution of each requirement to the cost function is computed by a penalty function. The larger the violation, i.e. the more the airfoil differs from the desired characteristics, the larger the penalty becomes. A lower penalty will therefore result in an airfoil with better aerodynamic properties.

The aerodynamic cost function consists of the following six sub-requirements:

1. L/D_{max}, the lift over drag ratio is a very commonly used measure for airfoil efficiency since c_l can be considered as the production and c_d can be viewed as the loss.
2. $C_{l,design}$, the design lift coefficient is the lift coefficient at the point where the L/D ratio is maximum. This will be the operating point of the airfoil.
3. $\Delta C_{l,max\text{-}des}$, the difference between the stall lift coefficient and the design lift coefficient.
4. $\Delta\alpha_{max\text{-}des}$, the difference between the stall angle of attack and the design angle of attack
5. $\Delta C_{l,des,clean\text{-}rough}$, the difference between the design lift coefficient in clean and in rough conditions. This is an indicator how well the airfoil behaves in rough conditions as a result of contamination by dirt and bugs.
6. $(L/D)_{max,clean}/(L/D)_{max,rough}$, the degradation of the L/D ratio as a result of surface contamination should not be too large, for this has a big impact on the airfoil efficiency.

This list of sub-requirements is transformed into functions that the evaluation function can use to compute a performance score for the airfoil. The general form of each of the penalty functions is identical: the penalty for each of the requirements is dependent on the relative deviation from the user-defined requirement. Then they are multiplied by the associated weight.

$$\mathrm{P}_1 = -\frac{\left(\frac{L}{d} - \frac{L}{d_{req}}\right)}{\frac{L}{d_{req}}} \cdot w_1 \tag{10.6a}$$

$$\mathrm{P}_2 = \left|\frac{\left(C_{l,des} - C_{l,des,req}\right)}{C_{l,des,req}}\right| \cdot w_2 \tag{10.6b}$$

$$\mathrm{P}_3 = -\frac{\left(C_{l,max} - C_{l,des}\right) - \left(C_{l,max} - C_{l,des}\right)_{req}}{\left(C_{l,max} - C_{l,des}\right)_{req}} \cdot w_3 \tag{10.6c}$$

$$\mathrm{P}_4 = -\frac{(\alpha_{stall} - \alpha_{des}) - (\alpha_{stall} - \alpha_{des})_{req}}{(\alpha_{stall} - \alpha_{des})_{req}} \cdot w_4 \tag{10.6d}$$

$$\mathrm{P}_5 = -\frac{\left(C_{l,des,clean} - C_{l,des,rough}\right) - \left(C_{l,des,clean} - C_{l,des,rough}\right)_{req}}{\left(C_{l,des,clean} - C_{l,des,rough}\right)_{req}} \cdot w_5 \tag{10.6e}$$

$$\mathrm{P}_6 = -\frac{\frac{L}{d_{clean}}}{\frac{L}{d_{rough}}} \cdot w_6 \tag{10.6f}$$

Given this list of penalty sub-functions, it must be clear that the selection of the weights of each of the criteria has a major influence on the results the optimizer converges to. The disadvantage of only using only the above approach, is that the easiest way for the optimizer to minimize the penalty is to minimize the penalty function that has the highest weight attributed to it. This is not the aim of the aerodynamic cost function; the aim is to have the highest aerodynamic efficiency (L/D) while satisfying the other constraints as well. Therefore another condition has been added:

$$if\ P_i > 0 \rightarrow P_i = c_i * P_i \quad , i = [1{,}6] \tag{10.7}$$

Where c_i represents the penalty coefficient by which the penalty score is multiplied. This will make sure all conditions are satisfied. The idea to use this approach is in accordance with the supervisor (Timmer 2014). The total cost function score is now the sum of all the individual sub-cost functions plus an additional penalty if another restriction is violated. The equation for the total cost function score becomes:

$$CF_{aero} = \sum_{i=1}^{6} P_i + P_{AOA} + P_{th} \tag{10.8}$$

In the formula, the indices 1 to 6 represent the six requirements; the residual terms are restrictions. These restrictions are related to the 1) *Angle of attack gap* and the 2) *Trailing-edge thickness violation*. Both will be outlined in section 10.5.3.

By using the above described approach it is essential that the maximum lift coefficient (and corresponding stall angle) is identified correctly. This poses a challenge, because:

- The point of maximum C_l computed on the polar may already be at an angle of attack in which major separation occurs; i.e. not always is the highest lift coefficient in the polar also the stall point.
- There can be several local lift maxima on a polar.

The method used to identify the maximum lift is the *findpeaks* function in MatLab. The function is configured in such a way that it locates a maximum of two peaks that satisfy specified conditions. These ensure that the peaks are at least 5 degrees apart from each other and both have a peak prominence[1] and width greater than a certain value. If no peak is found the stall point identified in the *aerodynamic_polar* object[2] is used. This can happen if RFOIL returns a polar with only a monotonously increasing slope, meaning it does not contain any peaks

10.5.2. Acoustic cost function

This cost function is applied to evaluate the airfoil on its acoustic properties. The function calculates the noise emitted for an airfoil using the BPM model with settings as described in section 7.2.

Before we can construct a proper evaluation function, we must first establish a suitable way to rate an airfoil on acoustic properties. Since noise is generated a various frequencies, and the human ear is not equally sensitive to each frequencies, it is not straightforward to formulate an unambiguous measure for noise. Because this is the case, Bak (Bak et al. 2009) evaluated four ways to do this. The discussed options are: 1) Maximum sound power level without A-weighting, 2) maximum SPL with

---

[1] The prominence of a peak measures how much the peak stands out due to its intrinsic height and its location relative to other peaks.

[2] This process is described in (De Oliveira 2011). In short: the maximum lift is defined as the lift coefficient at the end of the longest monotonously growing streak of the polar.

A-weighting applied, 3) Integrated SPL spectrum without A-weight and 4) Integrated SPL spectrum with A-weight.

The paper contains an analysis to observe the sensitivity of each measure to a change in angle of attack assuming both free transition and fully turbulent flow in the XFOIL computations. The result of this test was that both maximum and integrated A-weighted SPL show no unambiguous increase with an increase in angle of attack. The conclusion is therefore that either maximum or integrated SPL without A-weighting are both suitable measures for the noise. In this work, the latter is selected for the cost function.

The following information is needed to compute the SPL for a given airfoil shape:

- Environment data and operating conditions (density, flow speed, viscosity, speed of sound, etc.)
- Aerodynamic polar for a given airfoil
- Boundary layer data (Displacement thickness δ*)

The environment data are pre-defined by the user; the airfoil data, polar and boundary layer data, are varied in the optimization process. In order to be able to store the necessary boundary layer data, a routine is added to the *simulation_procotol* object. The polar computed by RFOIL is executed over the AoA range -7 to 20 degrees. The step size is set to 0.2 and the calculation takes place in several spans, for two reasons. The first is to avoid convergence into unphysical solutions, which happens e.g. when one would choose -7 degrees as starting point. The second is because RFOIL is only able to calculate and store boundary layer data for 60 operating point, otherwise the program crashes. The full routine for RFOIL to obtain the necessary data is the following:

- Compute polar and boundary layer data from 0 to 12 degrees in steps of 0.2 degrees and save the boundary layer data.
- Calculate only polar data from 12 to 20 degrees and reinitialize the boundary layer.
- Determine the polar data from 0 degrees to -7 degrees and save the results.

Once the necessary calculations for the airfoil are done, they are passed on to the acoustic evaluation function. Each time the evaluation function is accessed the following steps are taking place:

1. The results of the RFOIL simulations in clean and rough conditions are loaded into MatLab and used as input for the cost function.
2. The polar is evaluated and the design lift coefficient for the clean case is computed through the method described in the previous paragraph.
3. The corresponding design angle of attack is calculated and this, together with the displacement thickness at this angle and the environment data are used as input to the BPM model. The Overall Averaged Sound Pressure Level is now computed for both the clean and the rough case at the same angle, using the settings found in section 7.2. The sum of both noise emissions is set as the cost function score.
4. If either the polar or the profile shape violates certain constraints, a penalty is added to the cost function score.

Expression (10.9) is now used to compute the final cost function score:

$$CF_{sound} = OASPL_{clean} + OASPL_{rough} + P_{AOA} + P_{th} + P_{C_{l,des}} \tag{10.9}$$

In the formula, P_{AOA} and P_{th} are the same penalties as the ones mentioned in section 10.5.1 and $P_{Cl,des}$ represents the *design lift coefficient*-penalty. All three are described in the section that follows.

10.5.3. Other penalties

In the two cost functions used by the optimizer, several penalties were mentioned which influence the cost function score. These are related to bad and unreliable input data to the cost function, or a violation of a geometrical constraint. A brief elaboration on these penalties will be given.

10.5.3.1. *The angle of attack gap-penalty*

This penalty is applied to airfoil shapes that result in unreliable polar data produced by RFOIL. Since the cost function makes use of interpolation if certain data points in the polar are missing, the outcome can be distorted by any big gaps in the polar data. To prevent this, polars from both the clean and the rough experiments are checked for this and penalized if the gap is too large.

$$P_{AOA} = \begin{cases} 0 & \alpha_{gap} \leq \alpha_{gap,req} \\ c \cdot \alpha_{gap} & \alpha_{gap} > \alpha_{gap,req} \end{cases} \qquad (10.1$$

10.5.3.2. *The design lift coefficient-penalty*

If one aims to design an airfoil with a particular design lift coefficient, this requirement should not only be included in the aerodynamic cost function, but in the acoustic one as well. Otherwise solely the 'most aerodynamic' Pareto individuals would fulfill this constraint and the Pareto airfoils that are 'acoustically favorable' would not. Since the goal is to design an airfoil with a particular design C_l, it is set up a requirement and the penalty is therefore added to the acoustic objective function as well. Equation (10.11) shows how the penalty function is defined:

$$P_{C_{l,des}} = \begin{cases} 0 & \left(C_{l,current} - C_{l,des,req}\right)^2 \leq \varepsilon^2 \\ c \cdot \left(C_{l,current} - C_{l,des,req}\right)^2 & \left(C_{l,current} - C_{l,des,req}\right)^2 > \varepsilon^2 \end{cases} \qquad (10.1$$

Airfoils that deviate from the desired value by only a very small amount are also feasible solutions. Therefore, a tolerance margin ε, where no penalty is applied, is included in the expressions.

10.5.3.3. *The trailing edge thickness-penalty*

To prevent the airfoil shape to have an unrealistic (trailing edge) shape, the thickness distribution of the evaluated airfoil is compared to a reference thickness distribution. The idea of applying such a penalty function is suggested in correspondence with the supervisor (Oliveira 2014). The penalty is proportional to the square of the violated area and the reference thickness distribution selected is the NACA0006. In the figures below an example of how this works is shown for one of the generated airfoils.

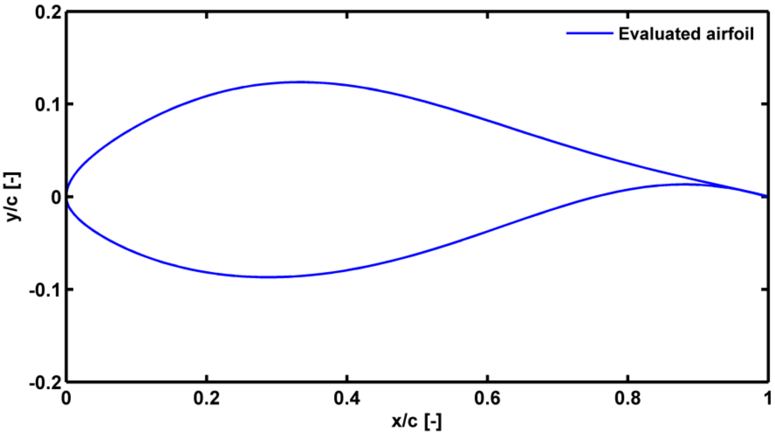

Figure 10.5: Generated airfoil by the optimizer; notice the unfeasibly thin trailing edge

It is clear from the figure above that the airfoil itself remains within the boundaries set up by the optimizer and is a feasible possible candidate. However, to avoid allowing the optimizer to converge towards shapes that are in reality not manufacturable, the solution graphically shown in the plot below was used.

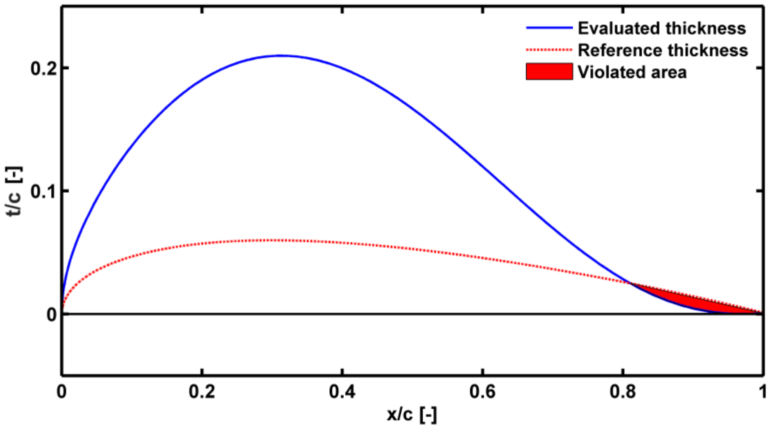

Figure 10.6: Illustration of thickness distribution violation

The thickness in this function is defined as the difference between the upper and the lower curve at each chordwise position. The blue curve represents the thickness distribution from the profile evaluated in Figure 10.6 the red dotted line is the thickness distribution of the NACA0006 airfoil. This is assumed to be the lower limit considering the minimum trailing edge thickness. The shaded red area is the total area where the TE thickness of the generated profile is thinner than that of the reference one. The penalty function is now the following:

$$P_{th} = C_1 \cdot A_{violated}^2 \tag{10.1}$$

11. Optimization case study

In this chapter the actual optimization will be described. The first sections will outline the applied settings, constraints and input parameters for the design of the aero-acoustic airfoil optimization.

In the case study an attempt will be made to design a low noise, aerodynamically high quality airfoil for the outboard section of a multi-MW wind turbine. Since the current trend is to use thicker airfoils in the tip region of the blade than in the past, the goal will be to design a 21% airfoil for a Reynolds number of 6 million. The optimization case study will provide (further) insight in the relationship between aerodynamics and aeroacoustics. Moreover, it can be seen an initial attempt to design aerodynamically usable, silent airfoils. Ideally general guidelines can be derived from the results and might be used in future airfoil design studies.

In the next sections the design criteria and for such an airfoil are outlined and how this translates into general optimizer and e.g. objective function settings.

11.1. Aerodynamic settings

In the previous chapter, some general design criteria have been established that an engineer has to take into account when designing an airfoil. Furthermore, the aerodynamic cost function is set up in such a way, that it can deal with any kind of aerodynamic airfoil optimization. Not only the one that will be considered in this case study, but airfoils with different (aerodynamic) requirements as well.

In section 10.5.1 the most important aerodynamic requirements for an airfoil located at the outboard part of a wind turbine blade have been outlined. These general requirements now have to be specified for this particular case. The characteristics listed in Table 11.1are deemed desirable. These were established in consultation with the supervisor (Timmer 2014).

Table 11.1: Clean condition airfoil characteristics

Reynolds number	$6 \cdot 10^6$
Thickness	21%
Design lift coefficient $C_{l,des}$	1.15
$L/D\|_{max}$	>165
$C_{l,max}$ - $C_{l,des}$	< 0.4
$\alpha_{cl,max}$ - $\alpha_{cl,des}$	>4°

So, rather than to optimize for a design angle of attack, the objective is to aim for a $C_{l,des}$ of ~1.15 for an airfoil of 21% thick. These design goals should also be reflected in the weighting coefficients, i.e. by imposing a large penalty if an airfoil deviates too much from the desired lift coefficient. Furthermore, the table denotes that the difference between the maximum C_l and the design C_l should be smaller than 0.4 and the difference between the associated angles larger than 4 degrees (Brondsted & Nijssen 2013).

The wind turbine does not only operate in clean conditions, but will experience some accumulation of dirt or bugs, so rough conditions must be evaluated as well. In the RFOIL simulations, the rough case is represented by imposing transition at chordwise positions of 5% at the suction side and 10% at the pressure side. The requirement for this case is translated in the following:

$$C_{l,des,clean} - C_{l,des,rough} < 0.07 \tag{11.1}$$

A visual representation of the requirements for the airfoil in clean conditions is illustrated in the sketch below.

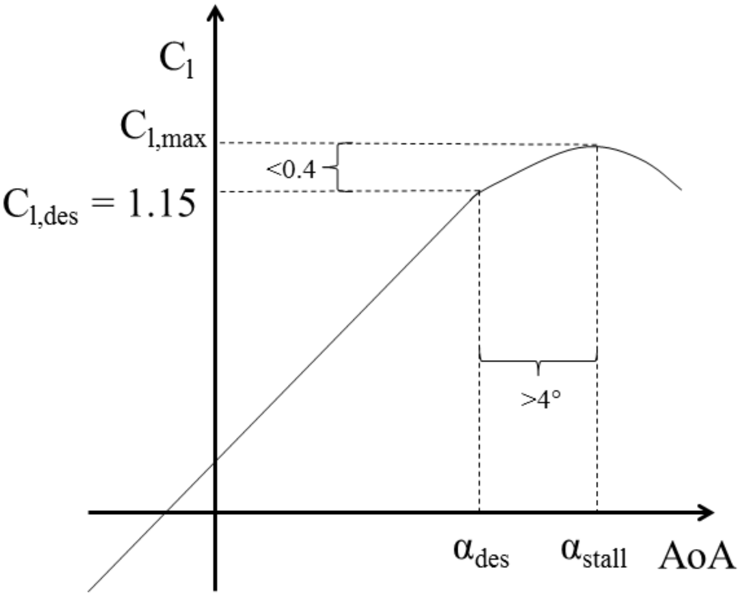

Figure 11.1: visual representation of the airfoil in clean conditions

This figure only shows the main criteria for clean conditions. The more requirements a generated shape satisfies, the better it performs from an aerodynamic standpoint. In addition to the criterion shown in equation (11.1), the optimizer also strives to minimize the $L/D|_{max}$ degradation in rough conditions compared to the clean one. The figure also depicts a lower slope after the design angle of attack. This is a desirable feature as well and ensures that a sudden increase in AoA beyond the α_{des} in case of a gust does not result in a significant increase in loads. To a certain extent, this is included in the aerodynamic cost function. The combination of $C_{l,max}$-$C_{l,des} < 0.4$ and $\alpha_{stall} - \alpha_{des} > 4°$ ensures that the stall point is not to close to the operating point. However, the sudden change in slope that is shown in the figure is not incorporated in the evaluation function.

As mentioned in section 7.1, the drag prediction computed by RFOIL in this case is underestimated by ~10%. According to Timmer (Timmer 2014), this underprediction is dependent on the airfoil thickness. For a 21% thick airfoil, this underprediction is more severe and amounts to ~12%. This obviously has an effect on the height of $L/D|_{max}$. Therefore the RFOIL drag output is increased by 12% to take this into account.

11.2. Operational and environmental settings

For the acoustic part of the optimization some parameters and conditions have to be set up as well. As described in section 10.5.2, these settings consist mostly on environmental conditions and blade/airfoil operating conditions. These are listed in Table 11.2

Table 11.2: Environmental and operating conditions for the acoustic cost function

Density [kg/m^3]	1.225
Kinematic viscosity [m^2/s]	$1.46 \cdot 10^{-5}$
Speed of sound [m/s]	340
Reynolds number [-]	$6 \cdot 10^6$
Mach number [-]	0.25
U_{eff} [m/s]	85

The operating conditions are typical values for a wind turbine placed at a temperature of approximately 20°C and at standard pressure. By applying these values, the chord length of the airfoil is fixed at a length of 1.0 m. The acoustic assumptions, related to directivity of sound and the observer position, can be found in the table below.

Table 11.3: source receiver conditions for the optimization

Segment width [m]	1.0
Θ [°]	90
ϕ [°]	90
Distance [m]	1.0

It can be concluded from this table that the 'observer' is located right in front of the airfoil at a distance of 1 meter. The directivity function in this situation therefore amounts to unity. The width of the airfoil segment is one meter as well ('blade' span). This is, evidently, not a realistic value for a wind turbine blade, but for the purpose of the optimization it will suffice. If a different value would be applied, this should not influence the result of the optimization. It would merely affect the absolute value of the cost function score, not the relative.

11.3. Optimizer settings

In the previous chapter, a basic description was given of the applied multi-objective optimization algorithm. This section will contain the optimizer settings that are used in the final optimization case in order to reach convergence. The subjects listed below will be touched upon:

1. Optimizer settings
2. Initial population used
3. Boundaries & constraints

11.3.1. Optimizer settings

Finding the right settings for the optimizer is essential to obtain the right results. This can be concluded from chapter 10, where the various aspects of the genetic algorithm optimizer were introduced and explained. In Table 11.4, an overview is given of the parameters as applied in the optimization.

Table 11.4: Optimizer settings applied to final optimization case

BPO_{upper}	8
BPO_{lower}	8
Max. nr. of generation	51
Population size	200
Crossover fraction	0.8
Pareto fraction	0.2
Mutation rate	0.03
Distance measure space	genotype

The Bernstein Polynomial Order was eventually set as 8 at both the upper and the lower side, which is reasonable but not ideal. This is done for two main reasons, the first being the rate of convergence. During the process, it was found that convergence for higher BPOs is more time consuming than for lower, for only marginally better results. The second reason for this is that one of the linear inequality constraints the optimizer is subjected to, requires an equal BPO at the upper and the lower side of the airfoil.

As for the population size and the maximum number of generations, these were set up generously, to make sure the optimization reaches convergence. The combination of the population size and the Pareto fraction was necessary to obtain a clear Pareto front. To maintain diversity in each generation, the distance measure space was set to genotype.

11.3.2. Initial population

The initial population can be supplied with a number of reference individuals to give the optimization process an initial boost. This way, it does not have to start from point zero but already has some reasonably performing individuals. The time necessary to finish an optimization run can be reduced in this way. However, if the number of injected airfoils in the initial population is too large, there is a risk of losing diversity and thereby one of the key assets of the genetic algorithm. On the other hand, the rate of convergence is lower is the number of injected candidates is too small. The optimization will then take longer.

The number of reference airfoils used in this case study amount to 15 candidates, a reasonable amount. They consist of a mix of both existing airfoils and the results of some earlier optimization test runs. They comprise of solely 21% thick airfoils. The airfoils that are amongst the existing ones are the following: DU93-W-210, FFA-W3-211, NACA2421, NACA4421, NACA23021, NACA63$_4$-421 and the S809 airfoil.

These existing airfoils are generally not used as tip region airfoils, but mostly in the transition region from the mid-section towards the outer one. Therefore, they might not perform as expected from an outer section airfoil from an aerodynamic point of view. However, they do provide some general direction for the optimizer in generating appropriate shapes. They also add some diversity to the initial population.

As for the non-existing airfoils, they are some of the Pareto individuals of a 50 generation test run with a population size of 200 under approximately the same conditions.

11.3.3. Boundaries & constraints

This paragraph will present the feasible region for the *shape definition* object of the optimizer to generate airfoils as possible solutions. These limits where established by the *constraint manager* object from an airfoil database as described in section 10.2 The boundaries used in the present case study can be found in the graph below.

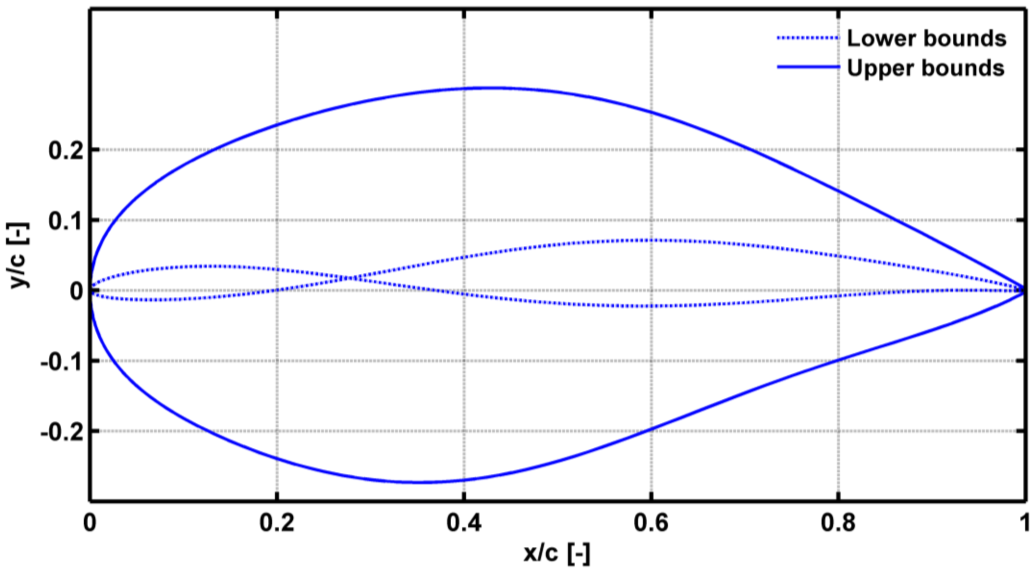

Figure 11.2: airfoil boundaries for the case study

Several things can be noticed from the figure above. Namely, the boundaries are set up very wide, so the design space is consequently equally large. This increases the chance that a shape can be found that will satisfy the requirements of the designer. Furthermore, it can be observed that also profiles can be generated that do not have the required maximum thickness of 21%. If such a candidate is produced, the maximum of the individual is normalized to unity and it is multiplied by the desired thickness of 21%. This will ensure that every candidate has the specified thickness. Note, the maximum thickness is defined as the maximum difference between the upper and the lower side measured at each chordwise position.

In addition to the boundaries sed above, the optimizer also has the possibility to apply some linear (in)equality constraints. For the optimizer to run stable and not crash in (mainly) the beginning of an optimization it was necessary to make use of this possibility. The constraints are listed below:

$$c_{8,up} \geq 0.2$$

$$c_{8,up} \leq 0.25$$

$$c_{TE,up} - c_{TE,low} \geq 0$$

The upper two constraints have the following consequences: the upper side of the airfoil at the trailing edge has an angle between a minimum of 0.2 and a maximum of 0.25 radians (approximately 11.5 and 14.3 degrees). These constraints are necessary because the optimizer otherwise creates shapes that RFOIL has trouble reaching convergence resulting in a crash. The last constraint forces the trailing-edge thickness of the airfoil to be positive; this is applied for the obvious reason that, in reality, a negative thickness is not possible.

12. Optimization results and analysis

This chapter will discuss the results of the case study described in the previous chapter. The first paragraph will address the matter of convergence of the optimization. In the section that follows, the Pareto front will be shown and analyzed whether the optimizer has produced feasible airfoils. Evidently, the quality of the obtained results will be assessed as well, and how they compare with expectations.

First, a brief summary of some properties of the final optimization is given; they are presented in the table below.

Table 12.1: summary of optimization settings

Population size	200
Number of generations	51
Function calls	10,400
Simulation time	14 hrs 3 min

The optimization was performed on a Windows 7 64-bit operating system installed on an Intel CORE i7 @ 3.4 GHz 12 core processor and 32 GB of RAM.

12.1.1. Convergence

The stopping criteria of the NSGA-II algorithm are a convergence tolerance of 10^{-4} or the maximum number of generations, whichever of the two occurs first. In general, since a large population is considered, the second criterion is met first. In this section the level of convergence of the optimization case is assessed and it is evaluated whether the optimizer has converged sufficiently to yield results that are satisfactory. In section 10.4, it was pointed out that convergence of a multi-objective optimization is not a straightforward matter and several examples of convergence criteria were presented. In this section, some of these will be used to give an indication.

The first measure to illustrate the convergence of the optimizer is to have a look at the phenotype space after each 10 generations. This will give an idea whether the solutions in each generation are still improving. If the cost function scores between two generations are very close together, it indicates that the optimizer has approached or even reached convergence. A graphical representation of this development of the cost function scores is illustrated in the figures below.

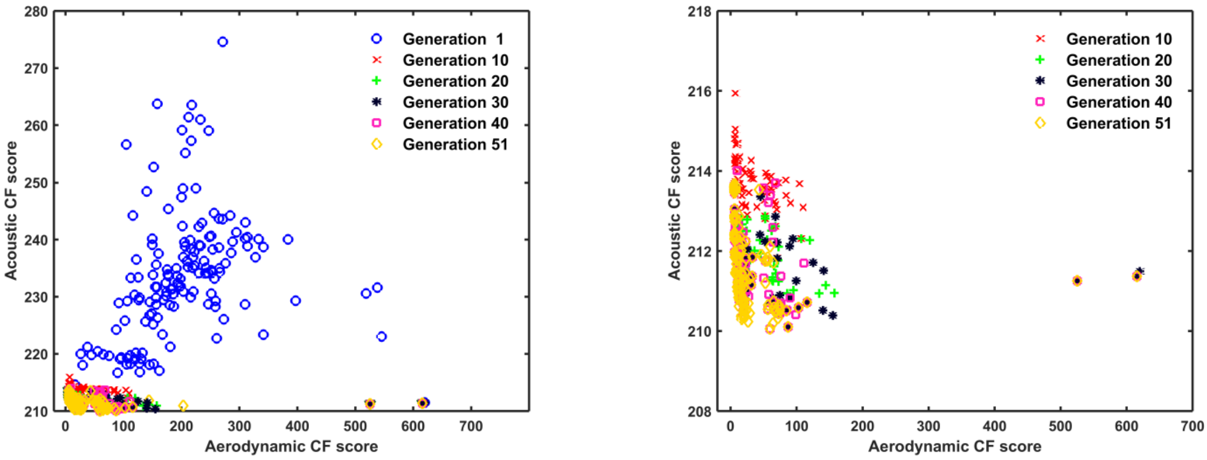

Figure 12.1: development of the cost function scores, left: generations 1-51, right: generations 10-51

The plots above confirms that the optimizer is indeed converging, since the cost function scores of the individuals decrease as the number of generations increases; the points move towards the origin of the graph. Moreover, the scores become more clustered, an indication that the progression of the scores will come to a halt and cease to improve. This shows that the optimization is not very far from convergence. Another measure to substantiate this observation is to have a look at the average distance between individuals. This is computed by quasi-randomly selecting 50 pairs of individuals from the population and finding the average distance between each pair. Figure 12.2 shows how the average distance varies over the course of the optimization.

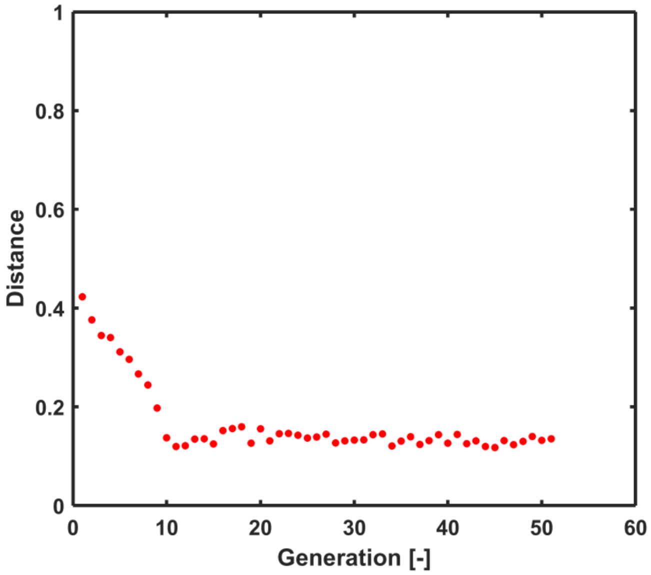

Figure 12.2: average distance between individuals per generation

The plot shows that the average distance between the individuals decreases in the first generations, and becomes stable after approximately 10 generations. It verifies the presumption that the optimizer is indeed converging. It also suggests that after 10 generations, the quality of the results barely improve. However, Figure 12.1 shows otherwise: the phenotype space still moves towards the origin.

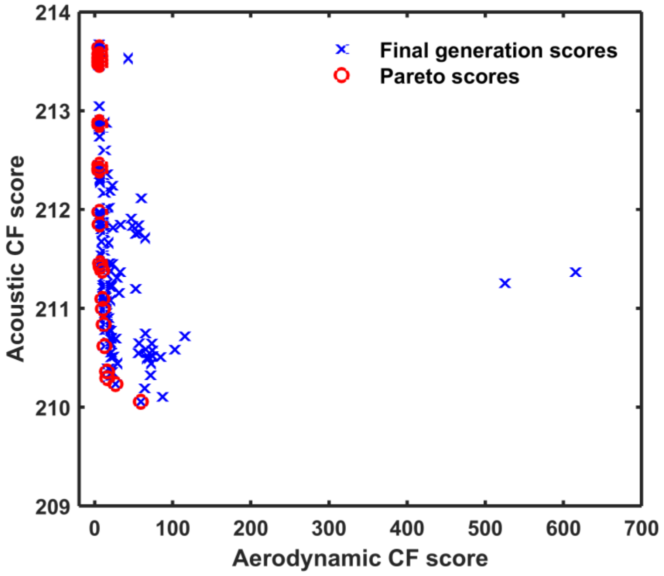

Figure 12.3: Phenotype space of the final generation

To further evaluate the matter of convergence, a glance at the scores of the final generation will now be cast. In the graph Figure 12.3 above, these scores are shown. The markers that are highlighted by the red circles are the individuals that appear in the Pareto front. It can be seen that the individuals are highly clustered together; especially along the vertical axis, the acoustic evaluation, the Pareto front is well defined. The spread in the aerodynamic results appears to be very limited. Whether this is the case, or whether the graph is deceiving due to the scale of the y-axis, will be investigated in the next section, where the Pareto front will be thoroughly examined.

12.1.2. Pareto-front

In this paragraph, the non-dominated solutions obtained from the optimization case will be evaluated. This set of solutions can be found in Figure 12.4 and Figure 12.5. The left is the entire set of non-inferior solutions, whereas in the right figure the utmost right solutions are excluded to focus on the airfoils that perform better aerodynamically. As explained, each of the points represents the score a geometry delivers based on both objective functions. This geometry is composed of a combination of Bernstein Polynomial coefficients that together form the shape.

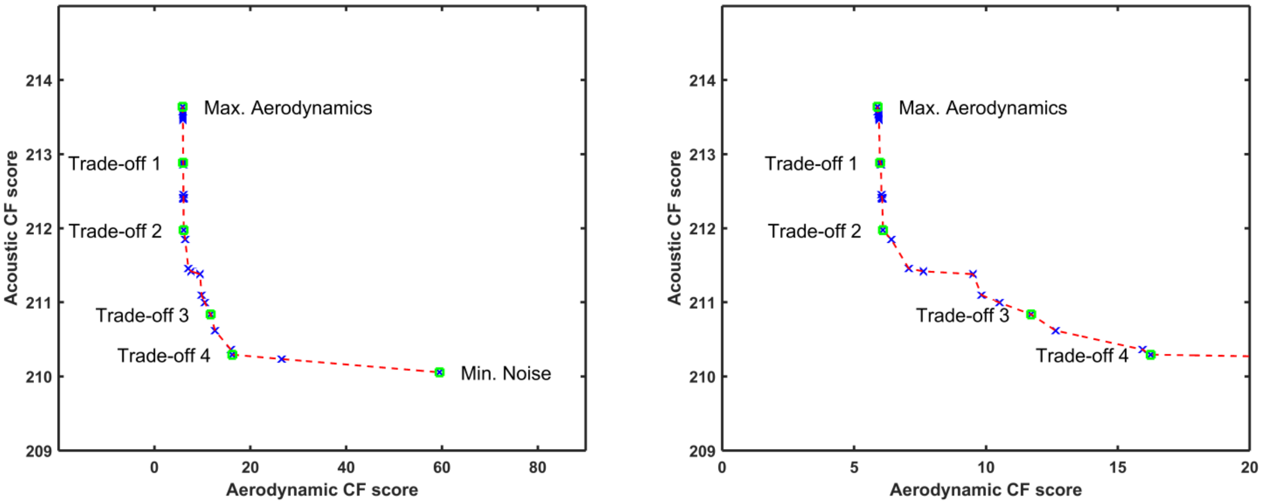

Figure 12.4: Pareto front of the optimization (left) and a close-up (right)

Several remarks can be made about the Pareto front; the first is that the Pareto front is not very well-defined. Ideally, the non-dominated set of solutions should consist of more points to describe the shape of the curve properly. As pointed out in section 11.3.1, the Pareto fraction was set at 0.2. Along with a population size of 200, this should therefore result in 40 Pareto solutions, a reasonable number for a proper Pareto curve. Though this is the case, some of the cost function scores appear twice (not only in phenotype space, but in genotype space as well). This results in 29 unique solutions, instead of the presumed 40. A plausible explanation could be that the NSGA-II optimizer forces a Pareto set of 40 individuals, even if there are less non-dominated solutions than 40.

Moreover, the front does not appear to be very evenly distributed. The acoustic part of the solution set seems reasonably explored, given the number of points along the vertical axis of the graph. The aerodynamically favorable solutions do not seem to be distributed as nicely, given the sudden gap in the scores of the aerodynamic cost function. This can be a combination of two reasons. The most important one is due to the way the cost function is set up, as discussed in section 10.5.1. The score remains low if the generated profile fulfills all requirements. However, if one of the requirements is violated, the penalty – and thereby also the score - immediately increases severely. The degree to which this happens depends on which requirement is violated.

Another explanation is that the exploration of the aerodynamic part of the spectrum still is not complete and the optimizer is in need of more generations to accomplish this task. This, however, is a very time consuming process. Since, although being a double-objective optimization in strict sense, the aerodynamic cost function is evaluated on multiple sub-requirements, the full exploration of the ‘aerodynamic spectrum’ is too computationally intensive to perform.

The figure also shows that the difference between the acoustically best and worst performing airfoils is very small. The best performing shape has a score of a little over 210, while the worst one scores a little below 214.

To be able to understand the reasons for the observations discussed above, it is necessary to have a more in depth look at some profiles. This is why 6 airfoils of the Pareto front were selected to be evaluated more thoroughly; they are shown in Figure 12.4.The aerodynamically best performing profile is named MaxAero, the acoustically best profile is denoted as MinNoise, the intermediate ones are trade-off (TO) solutions. These four trade-offs are ranked from aerodynamically best to worst performing. This assessment is done in the section that follows.

12.1.3. Assessment of the results

In this section, the six cases mentioned in the previous paragraph are evaluated in detail. First, the difference in each of the shapes is considered. Then, it is viewed how they perform both aerodynamically and acoustically by having a look at e.g. their respective polars.

12.1.3.1. *Geometry analysis*

Below a picture can be found of each of the airfoil shapes of the six individuals considered.

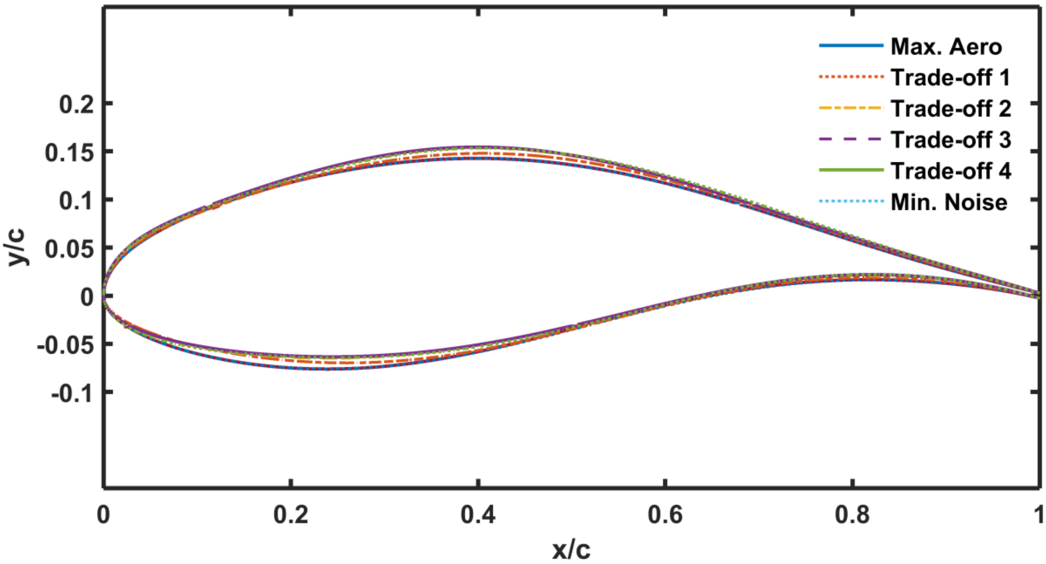

Figure 12.5: shapes of the six selected airfoils

What immediately stands out is that the profiles look similar to each other; only minor differences can be observed. Considering the small difference between the minimum and maximum values in the Pareto front of the previous section, this is to be expected. The difference between the most extreme cases, maximum aerodynamics and minimum noise, is insignificant.

What can also be observed about the shapes is the high degree of camber in all of the profiles. Below, a table can be found that denotes the most important geometrical parameters of the shapes.

Table 12.2: geometric parameters of the selected cases

Airfoil	Max. thickness [%]	Location [%]	Max. camber [%]	Location [%]	TE thickness [%]
Max. Aero	21.0	31.5	5.36	58.8	0.51
Trade-off 1	21.0	31.5	5.31	58.8	0.51
Trade-off 2	21.0	33.9	5.53	58.8	0.52
Trade-off 3	21.0	33.9	5.81	56.0	0.54
Trade-off 4	21.0	33.9	5.82	56.0	0.55
Min. Noise	21.0	35.0	5.83	57.4	0.55

Note that the maximum thickness of each of the profile is equal to 21%, as is the case for all profiles generated. Recall that, as pointed out in section 11.3.3, the shapes produced are forced to have a maximum thickness equal to the desired thickness. And this maximum thickness was defined as the maximum difference between the upper and the lower side measured at each chordwise position. The location of this maximum thickness is roughly between 31-35%, as is the case in most airfoils that are applied in real wind turbines. For the airfoil to be geometrically compatible with the neighboring one, it is important that the maximum thickness is located at approximately the same chord wise location.

The other most notable thing from the table is the high degree of camber. Generally, for a tip region airfoil, the maximum camber witnessed remains lower than 4%. For the airfoil to be compatible with other existing airfoils that are situated more towards the root, it is desired that their respective maximum cambers are close to each other. For these solutions this is unlikely to be the case. Such a constraint was not incorporated in the optimization process so it is not surprising that they might not match. The consequence of the maximum camber is discussed in the next section.

From a structural perspective, it can be noted from the figure that there might be some issues with integrating a beam in the construction process. This makes it difficult to manufacture and raises the costs of the blades. However, it is not surprising that the optimizer generates these shapes, since structural considerations were not taken into account.

The final point to mention regarding the geometrical properties is related to the shape and thickness of the trailing edge. The trailing edge thickness of each of the cases is in the range of 0.5%, almost negligibly small. From a manufacturing point of view, a small positive value is required; otherwise the shape cannot be produced. The figure also shows that the trailing edge thickness penalty function introduced in section 10.5.3 serves its purpose nicely since no negative thickness or unrealistically thin trailing edges are present.

Another point to note regarding the trailing edge thickness penalty function is the following. The negative side of applying this method is that airfoils that have a thickness at the trailing edge that is approximately constant, i.e. has a rectangular shape, are also penalized. An extreme case of such an airfoil that is penalized is shown in the Figure 12.6 below. The figure shows the evaluated individual by the optimizer, which has a thin trailing edge from 75% chord location onwards. Furthermore, the mean camber line of the profile is shown. Finally, the NACA0006 profile is displayed, where the camber line of the both airfoils coincide. This way, it can be seen which sections of the evaluated airfoil violated the thickness constraint. Figure 12.7 zooms in on the trailing edge section of the same airfoil.

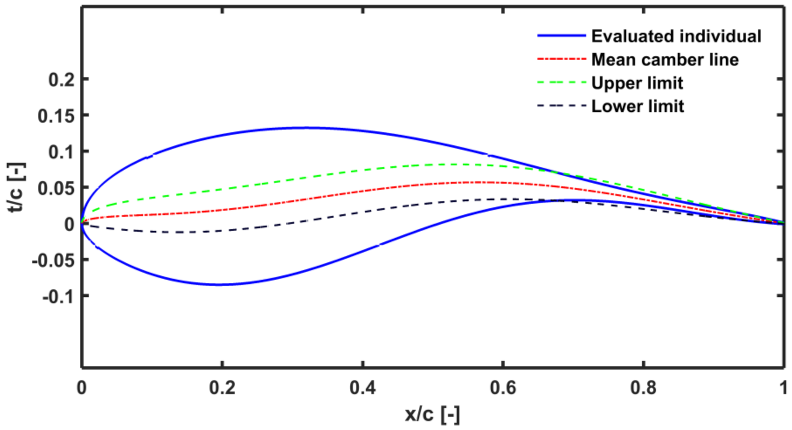

Figure 12.6: example of a penalized airfoil candidate

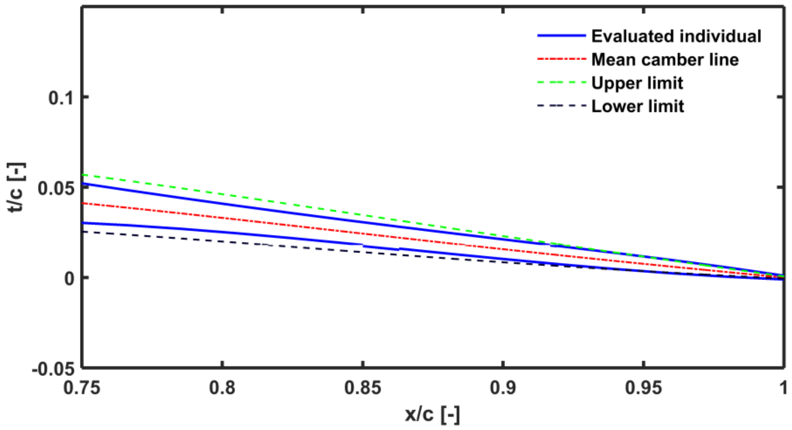

Figure 12.7: trailing edge of the penalized airfoil candidate

The consequence of using the penalty function in this way is that these types of profiles are disadvantaged compared to other profiles, while they might contribute valuable solutions. A better approach for the trailing edge thickness function would have been to manually specify a minimum thickness distribution manually for the final 25% of the chord.

12.1.3.2. *Aerodynamic and -acoustic analysis*

In the remainder of the chapter, the focus of the analysis will be on both the acoustic and the aerodynamic properties of the selected airfoils. This is done in various ways. First, the requirements defined for the objective functions in section 11.1 are compared with the results of each of the selected airfoils. Below, table can be found with the properties of the selected airfoils. The cells that are shaded green meet the associated requirements; the cells that are colored red do not. The upper region of the table shows the aerodynamic characteristics, the lower part the acoustic. At the bottom of each region the cost function (CF) score is mentioned as well. This will provide an insight in the composition of a score that has been awarded to a profile.

Table 12.3: properties of the six selected airfoils

	Req.	**MaxAero**	**TO1**	**TO2**	**TO3**	**TO4**	**MinNoise**
Parameter	**Aerodynamic properties**						
Cl_{des} [-]	**~1.15**	1.164	1.141	1.145	1.1484	1.142	1.114
$L/D\|_{max}$ [-]	**>165**	165.3	165.0	165.0	162.5	160.4	160.0
$C_{l,max}$-$C_{l,des}$ [-]	**<0.4**	0.35	0.37	0.31	0.33	0.35	0.34
α_{stall}-α_{des} [°]	**>4**	6.0	6.0	5.2	4.2	4.2	5.0
$C_{l,des,clean}$-$C_{l,des,rough}$ [-]	**<0.07**	0.067	0.066	0.069	0.066	0.066	0.068
$L/D\|_{max,rough}$ (% deterioration)	**-**	75.9 (-54.1%)	75.2 (-54.4%)	75.1 (-54.5%)	75.2 (-53.7%)	75.2 (-53.1%)	73.3 (-54.1%)
CF_{aero} score		**5.89**	**5.98**	**6.10**	**11.71**	**16.25**	**59.50**
	Acoustic properties						
SPL_{clean}	**-**	104.4	104.0	103.6	103.1	102.9	102.7
SPL_{rough}	**-**	109.3	108.9	108.4	107.8	107.4	107.4
SPL_{total}	**-**	213.6	212.9	212.0	210.8	210.3	210.0
CF_{sound} score		**213.6**	**212.9**	**212.0**	**210.8**	**210.3**	**210.1**

As can be seen in the table above, MaxAero, TO1and 2 are the only three airfoils of the selected ones that meet all of the aerodynamic sub-requirements defined in the cost function. This can also be seen in the cost function score: the difference between them is only very marginal. The other three do violate one or more constraints, and their CF scores increases rapidly.

Especially the MinNoise case, which violates two requirements, has an enormous increase in score compared to the others. This is mainly attributed to the violation of the design lift coefficient requirement. As mentioned in 11.1, the goal is to develop an airfoil with a design lift coefficient of 1.15 and therefore a violation of this requirement is severely punished; hence the large CF_{aero} score. However, its deviation is well beyond the defined tolerance and should not be present in the Pareto front. So this particular case also reveals a flaw in the definition of the acoustic evaluation function.

This presumption is confirmed by looking at the acoustic properties of the same case. It can be observed that the difference between the SPL_{total} (which is equal to the cost function score if no penalties are applied) and the CF_{sound} score is very small or even negligible (if rounding errors are taken into account). From this, it can be deduced that apparently no penalty is applied to the score, while this should have been the case. The design lift coefficient penalty function should have been implemented in such a way that the airfoil is punished (more) severely if it is outside the imposed limit. This would result in a Pareto front that only contains airfoils that meet the $C_{l,des}$ requirement.

The table above does not provide all the necessary information for a full evaluation of the aerodynamic performance of the airfoils. In order to expand the assessment the aerodynamic polars of the cases considered are looked at into more detail. The figures show the drag bucket as well as the lift coefficient versus angle of attack for both the clean and rough conditions. The maximum glide ratio for the clean condition, as well as the glide ratio for the corresponding AoA in rough conditions is depicted as well. Moreover, both the design and stall AoA, identified by the method outlined in section 10.5.1, are illustrated.

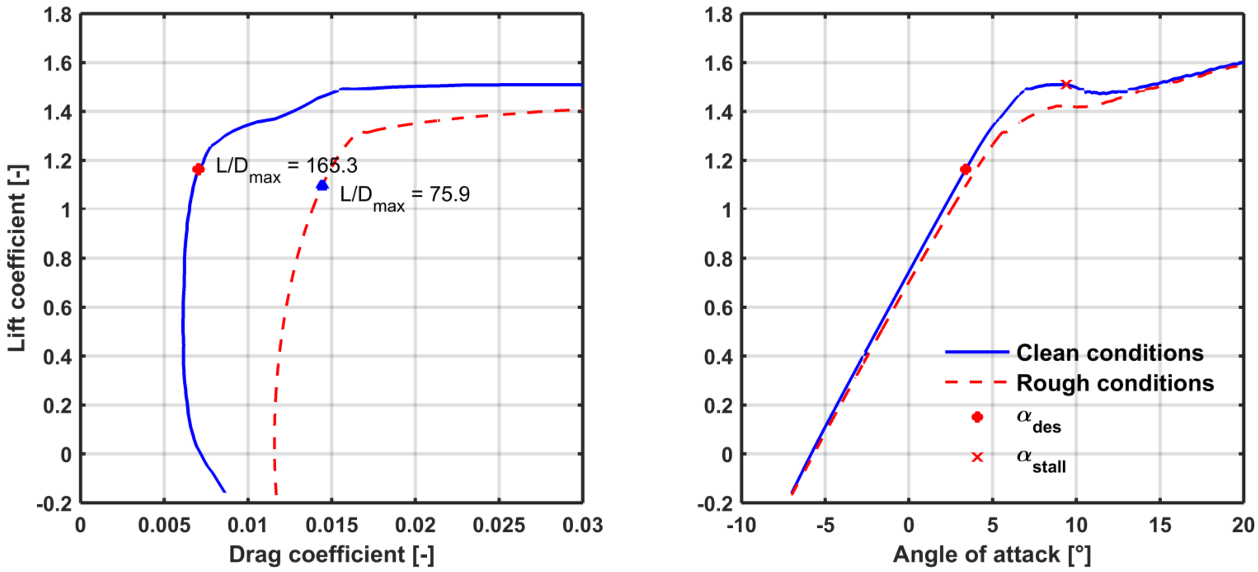

a) Drag bucket (left) and lift curve (right) for case MaxAero

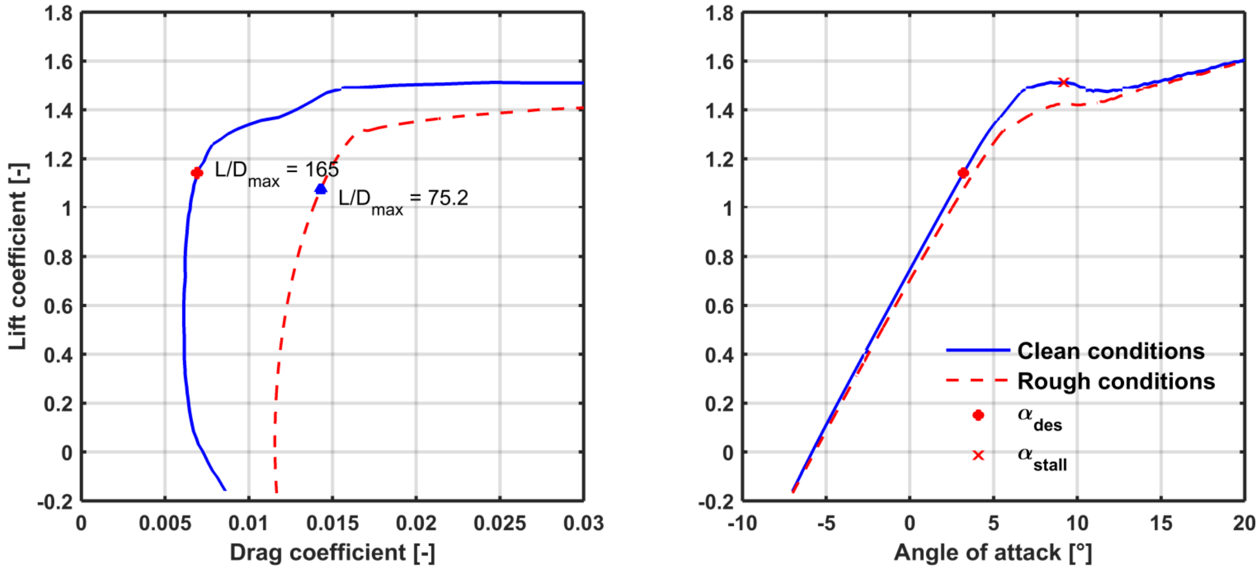

b) Drag bucket (left) and lift curve (right) for case TO1

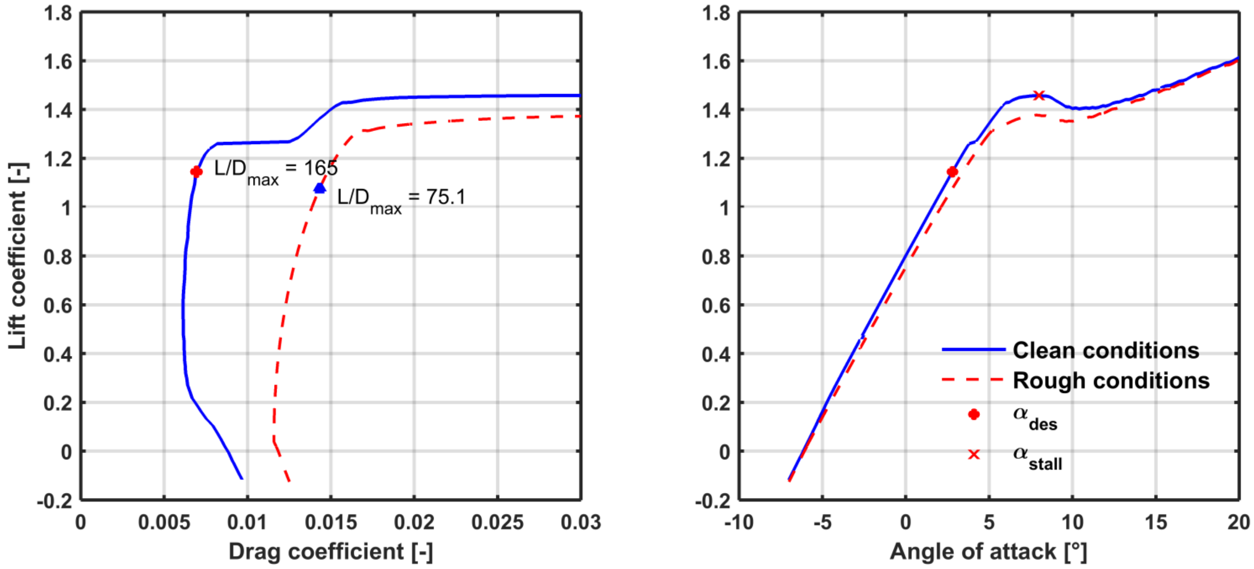

c) Drag bucket (left) and lift curve (right) for case TO2

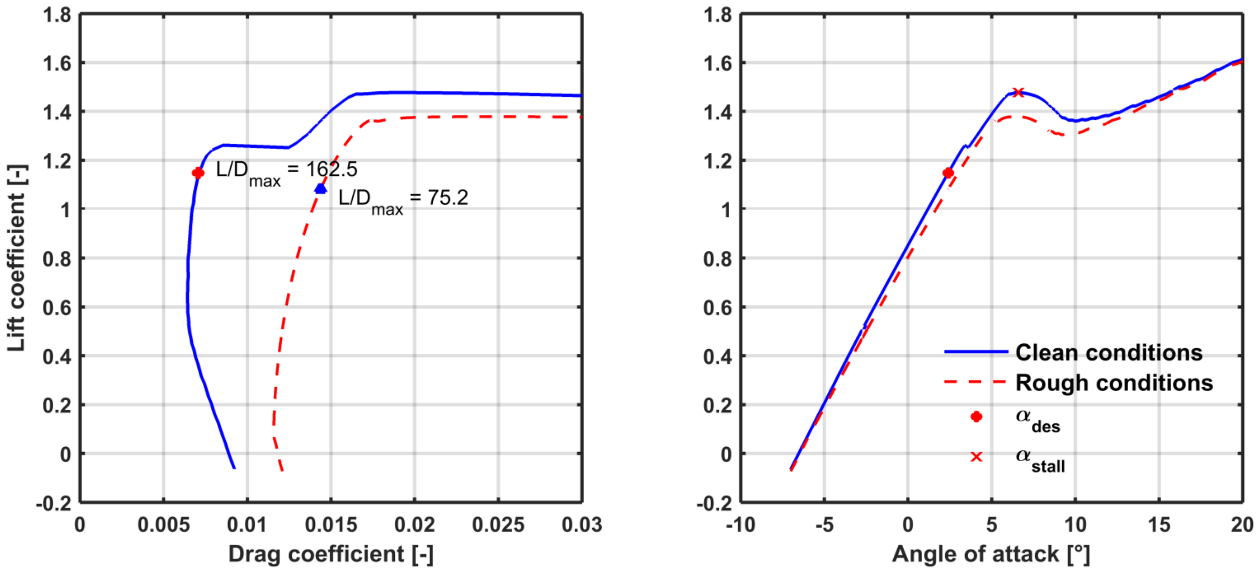

d) Drag bucket (left) and lift curve (right) for case TO3

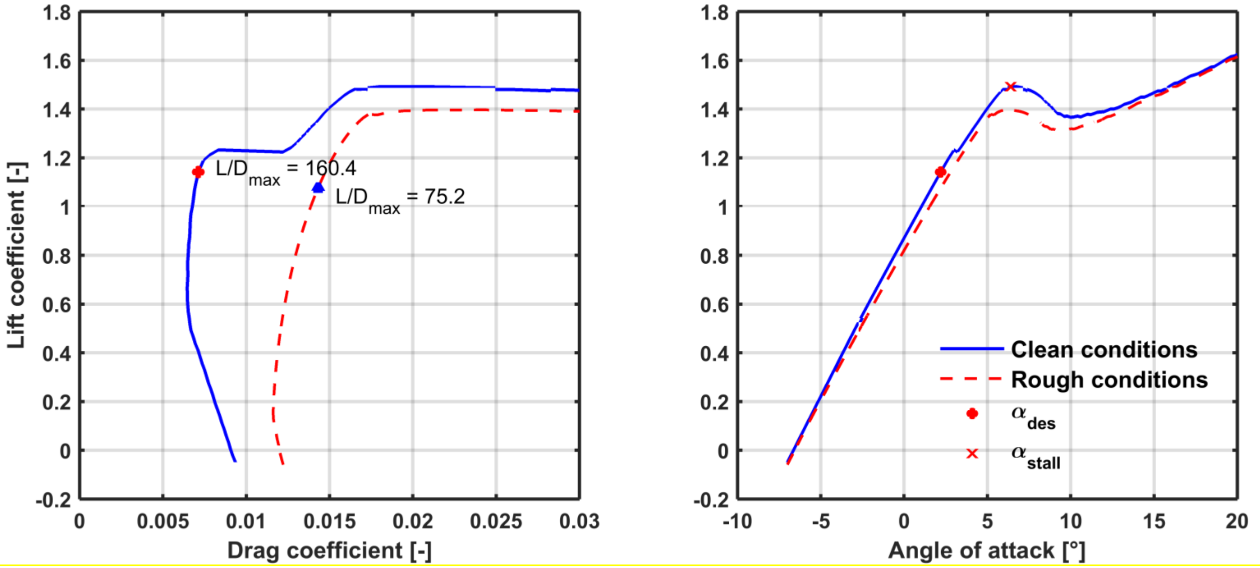

e) Drag bucket (left) and lift curve (right) for case TO4

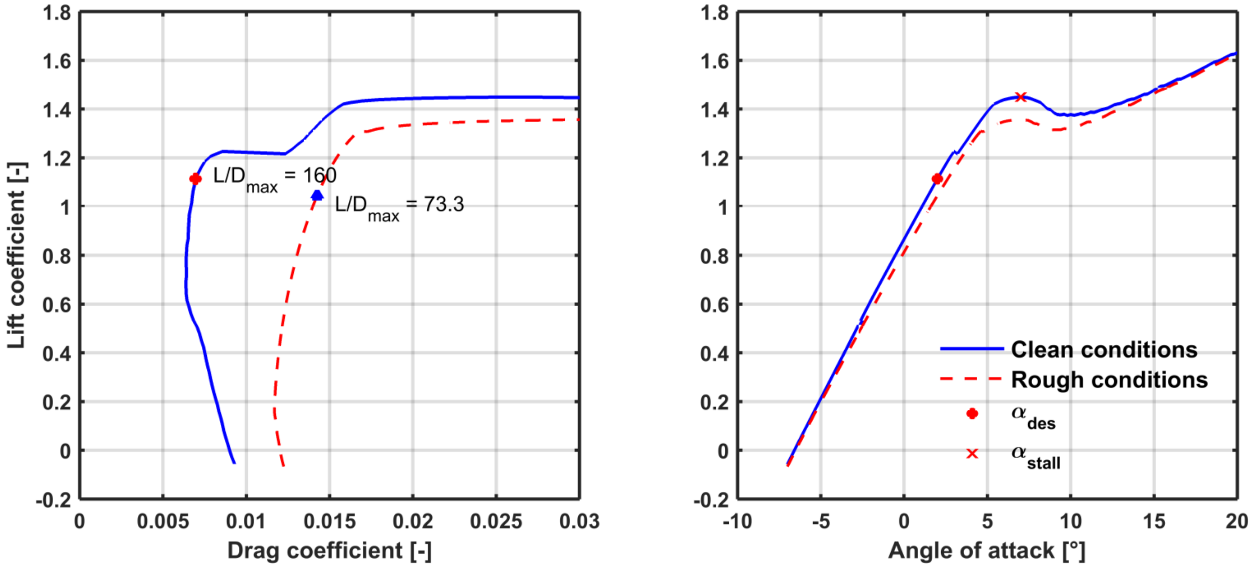

f) Drag bucket (left) and lift curve (right) for case MinNoise

Figure 12.8: Aerodynamic polar for the selected Pareto cases

First, it is good to note that the method of identification of the stall and design angle of attack is working properly. As stated before, especially the (automatic) identification of the design AoA is a difficult matter in airfoil optimization problems, and it is major importance because of the way the (aerodynamic) cost function is set up.

Furthermore, the optimizer produces polars that look quite nice, especially the MaxAero case. The lift curve of this profile satisfies the important criteria for a good aerodynamic profile. Moreover, the stall behavior is not too harsh, even though a requirement that takes this into account was not included in the cost function. The maximum glide ratio requirement is achieved as well, despite the 12% drag increase that was included to account for the underprediction of by RFOIL. Comparing the L/D_{max} at the same (design) angle of attack in clean and rough conditions, the plot shows that the drop is significant. However, this is found for all the airfoils considered, and a drop of ~55% is not uncommon in tip region airfoils.

Proceeding towards the ‘less aerodynamic’ shapes, it can be observed that the lift polars do not differ significantly from each other. It does on the other hand, show a slight irregularity around a lift coefficient of 1.2~1.3. This irregularity in the lift polar is much more outspoken in the drag bucket and is reflected by bump at a lift coefficient of approximately 1.23. At this level, the lift coefficient remains fairly constant, while the drag increases rapidly. Since the bump in the bucket is only present in the figures c-f, this leads to the conclusion that their drag polars must differ.

Something that is worth mentioning as well is the low design angle of attack in each of the cases, somewhere around 2-3 degrees. This can be explained by the high camber that is displayed by the airfoil. The high camber results in two main consequences:

- The lift curve shifts upward to higher lift values at the same angle of attack, the lift at zero degrees also becomes higher.
- The low-drag bucket shifts along the y-axis while the minimum drag coefficient remains more or less constant.

Given these two statements, and the fact that the optimizer is balancing between two goals, aerodynamic behavior versus acoustic, the high level of camber can be explained by the following reasoning. Since the airfoil is designed to have a design lift coefficient of 1.15 the aerodynamic cost function can only be favorable if this criterion is satisfied within a small margin. Furthermore, the acoustic cost function is computed by calculating the sound pressure level at the design angle of attack, which is obviously directly related to $C_{l,des}$. The turbulent boundary layer – trailing edge noise using the BPM model is explained in section 6.1.2. It outlines that the TE noise is dependent on the boundary layer displacement thickness δ^*, the Mach number, section width, directivity of the source and position of the receiver. Of these parameters, all but the displacement thickness remains constant. The optimizer is therefore searching for a profile that minimizes the displacement thickness at the design lift coefficient/angle of attack. Since an increase in camber results in a higher lift coefficient at the same angle of attack while the minimum drag remains (fairly) constant, the maximum L/D is targeted the occur at a low angle of attack.

In order to verify the reasoning above, the noise spectra for the clean conditions of each of the cases are shown in the figure below. As is the case for the aerodynamic polars, these are also shown from maxAero to MinNoise, or from ‘noisiest’ to least noisy. The figures also denote δ^* for both the suction and the pressure side, as computed by RFOIL, as well the calculated α_{des}. This is done to illustrate the effect this has on the noise level.

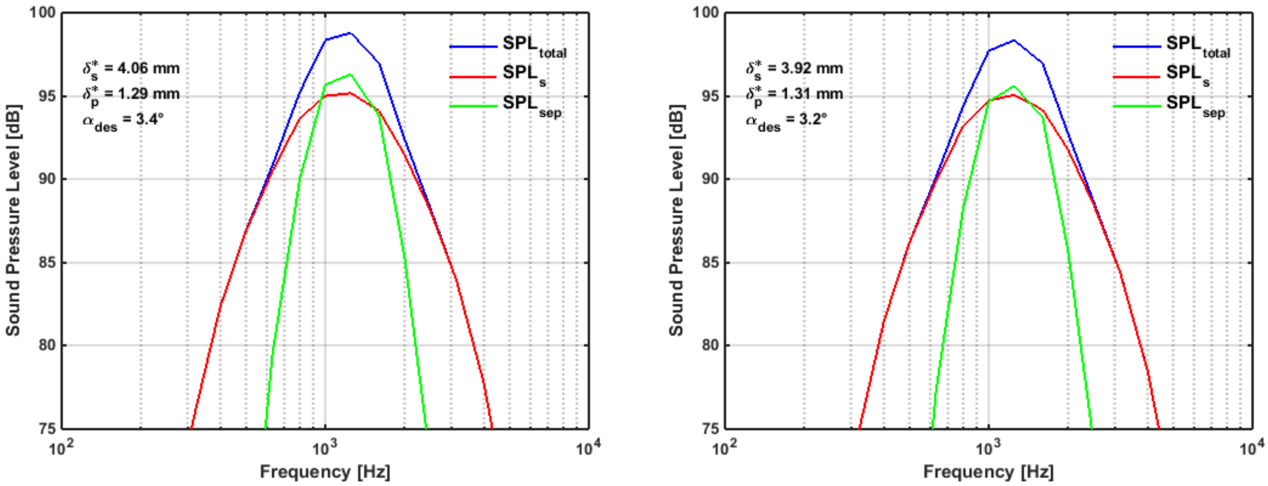

a) Noise spectrum MaxAero

b) Noise spectrum TO1

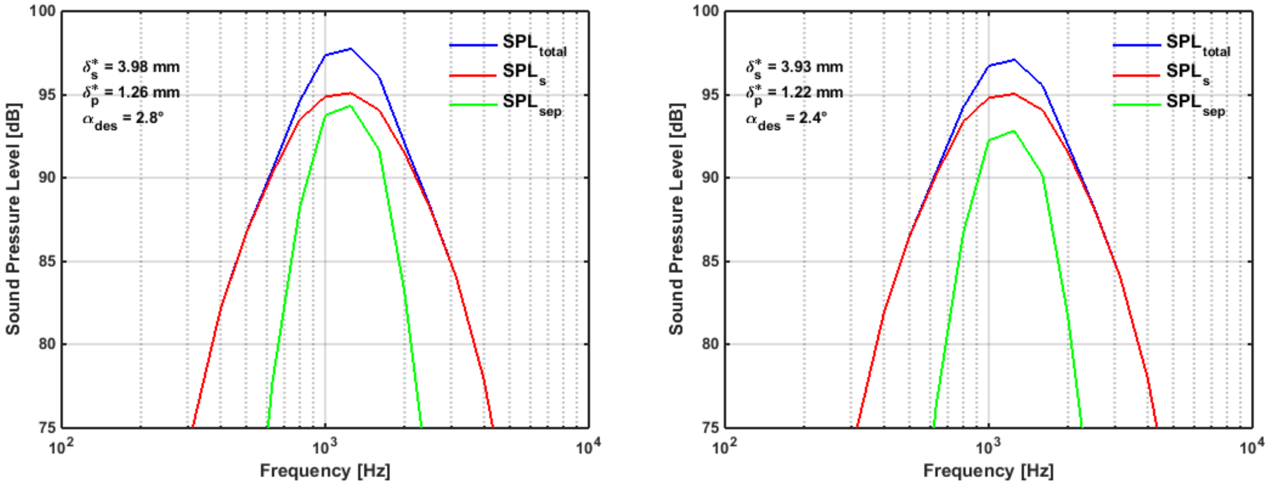

c) Noise spectrum TO2

d) Noise spectrum TO3

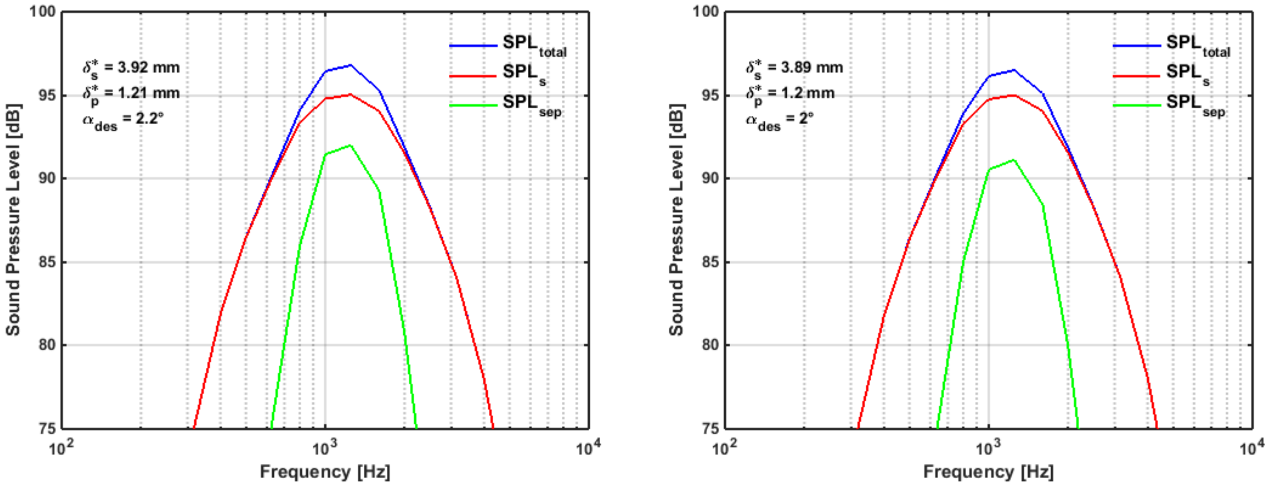

e) Noise spectrum TO4

f) Noise spectrum MinNoise

Figure 12.9: Noise spectra for each of the selected cases

The plots in Figure 12.9 show that the noise spectra of the various cases are very similar to each other. The suction side noise contribution, denoted by SPL_s, is (almost) identical in each of the plots. This can be explained by the small differences between the displacement thicknesses computed by RFOIL for the profiles. The deviations in the total noise spectrum can therefore be attributed to the SPL_{sep} contribution, depicted by the green curve. Of the two mechanisms, this is the only one that differs for each of the shapes. Since this is an angle dependent source term, and the total SPL is computed at the design angle of attack, the SPL_{sep} noise decreases as α_{des} decreases. This is confirmed by examining the design angles of the individual cases, it ranges from 3.4 degrees for the noisiest profile, to 2 degrees for the most silent one. These figures therefore verify the explanation for the highly cambered profiles.

To conclude the evaluation of the results, a brief glance at the pressure distribution is cast, to further investigate the results of the optimization. The figure below shows the pressure distribution for the MaxAero and MinNoise Pareto cases at three different angles, namely zero, three and six degrees. The figure also displays the boundary layer transition location as calculated by RFOIL; to demonstrate the effect it has on the noise emission and to further illustrate the differences between the two most extreme solutions. Below the figure, the shapes of the two considered cases are shown again, to be able to easily connect points on the pressure distribution to locations on the airfoil.

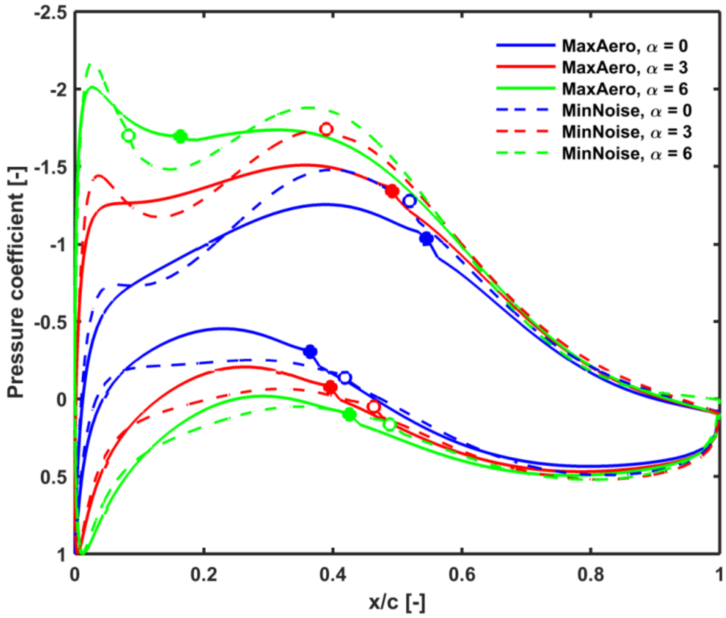

Figure 12.10: chordwise pressure coefficient distribution for MaxAero and MinNoise for three angles of attack

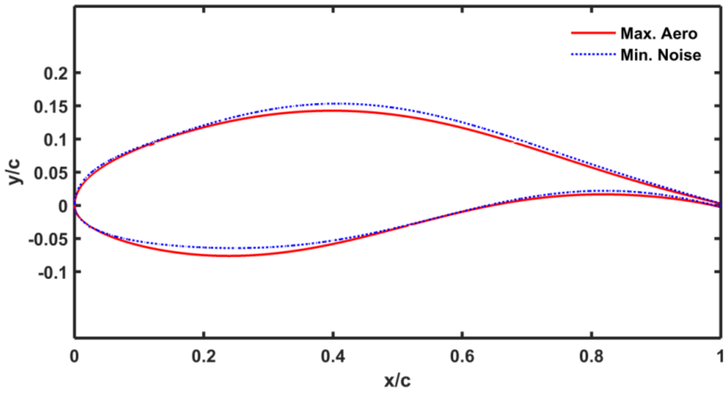

Figure 12.11: shapes of the two most extreme solutions: MaxAero and MinNoise

In the Figure 12.10 shown above the MinNoise airfoil is represented by a dashed line. As is usually the case when plotting the pressure versus the chord location, the y-axis is reversed in order to have a negative pressure at the top and a lower pressure at the bottom. This way, the top region of the graph corresponds to the upper section (suction side) of the airfoil, as is the case for the lower half.

First, the MaxAero pressure distribution will be considered. The blue line at zero degrees is well in the low-drag region of the Cl-Cd curve. The airfoil has a favorable pressure gradient along the upper surface to about 35%, the pressure distribution then flattens. Behind this point, the pressure has a negative gradient, thus stimulating the transition from laminar to turbulent flow. Then, at a chordwise position of 55% a laminar separation bubble is found and the transition takes place. After the transition, a region of almost linear pressure recovery until approximately 80% of the chord. As the angle of attack increases, it can be seen that the transition location of the upper surface moves further towards the leading edge, whereas the opposite applies to the bottom surface. Especially at six degrees, the transition point on the suction side rapidly translates to the LE, due to the development of the suction peak.

It is now interesting to compare the pressure distribution of MaxAero to the other extreme case of the Pareto front, MinNoise. It can be observed that the chordwise development of the pressure of MinNoise has a very different pattern than that of the MaxAero case, particularly in the first 60%. The suction peak already starts to develop at zero degrees and at higher angles the minimum pressure remains more dominant than the MaxAero one. The transition locations of MinNoise, indicated by the unfilled markers on the curve, are always located at an earlier chordwise position, at the same angle. An additional thing to note regarding the pressure distribution of airfoil: the boundary layer at the trailing edge is already showing signs of separation. In general, this is not desirable if the objective is to minimize noise. Considering it is the MinNoise case makes it all the more remarkable.

This can be explained by the fact that the acoustic cost function aims to minimize TBL-TE noise at a single angle of attack, α_{des}, in both clean and rough conditions. Therefore MinNoise will have a pressure distribution that is focused on minimizing the boundary layer displacement thickness at this angle, which amounts to 2 degrees. Since this angle of 6 degrees is out of the scope of the objective function, it is not taken into account in the cost function score.

All in all, the multi-objective optimization described in detail in this work generates airfoil results that would be usable in practice. If the aim is to minimize noise levels as much as possible, a geometry closer to MinNoise should be chosen. For a more aerodynamic profile, the shape should be closer to the other end of the Pareto spectrum, the MaxAero case. Although the shapes produced are usable from a manufacturing (though it would be difficult) and aerodynamic perspective, ideally the diversity between the Pareto individuals should be larger. This would provide a better understanding on the relation and trade-off between aerodynamics and acoustics.

13. Conclusions

This chapter concludes the presentation of the work developed in this thesis. First a summary is given of what is achieved during the course of the thesis, followed by some interesting suggestions in the opinion of the author, for future research on the topic.

13.1. Achievements

In the work developed for this thesis, a wind turbine aerodynamic and aero-acoustic airfoil optimizer was successfully developed. The tool developed, based on the work of De Oliveira (De Oliveira 2011), is flexible, with numerous settings that can be changed by the user, and robust.

Furthermore, to gain a better insight on the generation of aerodynamic noise on a rotor level, including the identification of the most dominant noise source, the SILANT acoustic prediction tool was successfully employed. The application of the tool was accompanied with the integration and validation of an aerodynamic BEM model, with appropriate extensions and corrections. The SILANT validation also shows that noise on a rotor level can be predicted with reasonable accuracy. Therefore, valid conclusions can be drawn on the most dominant noise source. In this respect, it is found that the airfoil optimization should focus on reducing the trailing edge noise.

Another accomplishment made in this thesis is the simple but effective method of identifying the design/stall angle of attack/lift coefficient. This is a difficult task to perform in optimization problems, but an important one as well. The operation of the aerodynamic objective function is dependent on the proper localization of these points.

The work also presents a thorough description, validation and quality assessment of two well-known and often used aero-acoustic prediction tools. The quality assessment of the BPM and the TNO model against measurements in the IAG wind tunnel showed that they both failed to accurately predict the noise level. It was decided to use a modified version of the BPM model.

Eventually, the modified model was successfully implemented into the optimization framework. The aerodynamic cost function works by minimizing a penalty function. The larger the violation of the requirement, i.e. the more the airfoil deviates from the desired characteristics, the larger the penalty becomes. The acoustic performance was based on the unweighted overall average sound power level at the design lift coefficient, in both clean and rough conditions. The results showed that the difference between the shapes of Pareto individuals was only marginal. This was also reflected the Pareto curve, the difference between the noisiest and the most silent profile was less than 2 dB. A comparison of the aerodynamic polars showed the same thing, the deviation between them was only limited. The optimizer *was* successful in designing several airfoils that met all the aerodynamic requirements.

13.2. Recommendations & future work

This section will outline some suggestions for future research, to further increase the knowledge level on the topic of this work.

Further attempts should be made regarding the quality of the noise models. The current models are not able to accurately predict the noise emission for all airfoil shapes. This is obviously of major importance in airfoil design. The quality of the end product is determined by the quality of the prediction model.

A recommendation for the continuation of the present work with the developed optimizer would be to tweak both cost functions. The acoustic cost function could benefit if off-design angles of attack would be included as well. Similar recommendations for the aerodynamic cost functions apply. A close look to the performance in rough conditions could be given. These suggestions would most likely increase the diversity of the results.

The optimization could also be extended to a 3D blade, rather than the 2D airfoil optimization that was executed in this work. This increases the complexity of the optimization, for the number of variables increases rapidly. In this case, parameters such as chord and twist distributions have to be taken into account as well.

The multi-objective optimization could, in future works, be expanded to include other design considerations as well. Instead of performing a two-objective optimization (aerodynamic vs acoustic performance), a third objective could be added, in the form of a structural model. This would undoubtedly have a significant impact on the computation time of the optimization, but if set up properly, could result in high quality airfoils.

A final recommendation that would be very interesting to look at is to include the regulations as constraints into the optimization. The Pareto front will then contain a set of solutions that all stay within the noise limit. The conversion of the legislation into constraints would be difficult, for the rules itself are complex. The usability of the results of such an optimization are very much dependent on the proper conversion of the regulation on the one hand, and the quality of the noise prediction model on the other.

References

Alander, J.T., 1992. On optimal population size of genetic algorithms - Alander. *CompEuro '92. "Computer Systems and Software Engineering"*, pp.65–70.

Amiet, R., 1975. Acoustic radiation from an airfoil in a turbulent stream. *Journal of Sound and Vibration*, 41, pp.407–420. Available at: http://www.sciencedirect.com/science/article/pii/S0022460X75801052.

Amiet, R.K., 1976. Noise due to turbulent flow past a trailing edge. *Journal of Sound and Vibration*, 47(3), pp.387–393.

Bak, C. et al., 2014. Airfoil design: Finding the balance between design lift and structural stiffness. *Journal of Physics: Conference Series*, 524.

Bak, C., Bertagnolio, F. & Aagaard Madsen, H., 2009. Design of High Lift Airfoils With Low Noise and High Aerodynamic Performance. In T. Buhl, ed. *Research in Aeroelasticity EFP-2007-II*. Denmark. Forskningscenter Risoe. Risoe-R. Danmarks Tekniske Universitet, Ris� Nationallaboratoriet for B�redygtig Energi, pp. 76–86.

Van Beek, A. & Van den Haspel, B., 1989. *Noise contours for wind turbines (dutch)*,

Blake, K., 1988. of Flow-Induced Sound and Vibration . Vol . I : General Concepts and Elementary Sources. , 83(1), pp.1397–1398.

Blake, W.K., 1986. *Mechanics of flow-induced sound and vibration*, Orlando, Flo: Academic press.

Boorsma, K. & Bulder, B., 2010. Silant, User Manual.

Boorsma, K. & Schepers, J., 2011. Enhanced wind turbine noise prediction tool SILANT. In *Fourth International Meeting on Wind Turbine Noise*. Rome. Available at: ftp://ecn.nl/pub/www/library/report/2012/m12004.pdf.

Brondsted & Nijssen, 2013. *Advances in Wind Turbine Blade Design and Materials* 1st ed., Woodhead Publishing.

Brooks, T. & Schlinker, R.H., 1983. Progress in rotor broadband noise research. *Vertica*, 7(4), p.21.

Brooks, T.F., Pope, D.S. & Marcolini, M.A., 1989. *Airfoil self-noise and prediction*, National Aeronautics and Space Administration, Office of Management, Scientific and Technical Information Division.

Buhl, M.L., 2005. A New Empirical Relationship between Thrust Coefficient and Induction Factor for the Turbulent Windmill State A New Empirical Relationship between Thrust Coefficient and Induction Factor for the Turbulent Windmill State. , (August).

Burton, T. et al., 2001. *Wind energy handbook*, John Wiley & Sons Ltd..

Carlén, I., 2005. Aerodynamic characteristics for the Siemens-2.3-93 rotor. , pp.1–14.

Chaviaropoulos, P. & Hansen, M., 2000. Investigating three-dimensional and rotational effects on wind turbine blades by means of a quasi-3D Navier-Stokes solver. *Journal of Fluids Engineering*. Available at: http://cat.inist.fr/?aModele=afficheN&cpsidt=1400263.

Chen, P.-Y., Chen, C.-H. & Wang, H., 2009. A Neural Network: Family Competition Genetic Algorithm and Its Applications in Electromagnetic Optimization. *Applied Computational Intelligence and Soft Computing*, 2009, pp.1–12. Available at: http://www.hindawi.com/journals/acisc/2009/474125/.

Chklovski, T., 2012. Pointed-Tip Wings at Low Reynolds Numbers. Available at: http://www.wfis.uni.lodz.pl/edu/Proposal.htm [Accessed March 1, 2015].

Colby, W., Dobie, R. & Leventhall, G., 2009. Wind turbine sound and health effects: An expert panel review. , (December).

Comsa, M., 2015. Small Wind Turbines. Available at: http://www.cleanenergybrands.com/shoppingcart/knowledgemanager/questions/157/101+Small+Wind+Turbines [Accessed March 1, 2015].

Curle, N., 1955. The influence of solid boundaries upon aerodynamic sound. *Proceedings of Royal Society London*, 231, pp.505–514.

Devenport, W. et al., 2010. *Aeroacoustic Testing of Wind Turbine Airfoils Aeroacoustic Testing of Wind Turbine Airfoils*, Virginia.

Du, Z. & Selig, M., 1998. A 3-D stall-delay model for horizontal axis wind turbine performance prediction. *AIAA Paper*. Available at: http://arc.aiaa.org/doi/pdf/10.2514/6.1998-21.

Eggers, A., Chaney, K. & Digumarthi, R., 2003. An Assessment of Approximate Modeling of Aerodynamic Loads on the UAE Rotor. In *41st Aerospace Sciences Meeting and Exhibit*. Aerospace Sciences Meetings. American Institute of Aeronautics and Astronautics. Available at: http://dx.doi.org/10.2514/6.2003-868.

Errasquin, L.A., 2009. *Airfoil Self-Noise Prediction Using Neural Networks for Wind Turbines*. Virginia Polytechnic Institute and State University.

Fink, M.R. & Bailey, D.A., 1980. Airframe noise reduction studies and clean-airframe noise investigation. *Final Report United Technologies Research Center, East Hartford, CT.*, 1.

Gasch, O.F., 2014. *Assessment , Development and Validation of Wind Turbine Rotor Noise Prediction Codes*. Technical University of Denmark.

Glauert, H., 1926. *The analysis of experimental results in the windmill brake and vortex ring states of an airscrew*, London: HMSO. Available at: http://www.worldcat.org/title/analysis-of-experimental-results-in-the-windmill-brake-and-vortex-ring-states-of-an-airscrew/oclc/312799286.

Goel, T. & Stander, N., 2010. A Study on the Convergence of Multiobjective Evolutionary Algorithms. In *13th Multidisciplinary Analysis and Optimization Conference*. pp. 1–18.

Gotshall, S. & Rylander, B., 2008. Optimal Population Size and the Genetic Algorithm. *Population*.

Grasso, F., 2008. *Multi-Objective Numerical Optimization Applied to Aircraft Design*.

GWEC, 2014. Global wind report 2014 - annual market update. Available at: http://www.gwec.net/publications/global-wind-report-2/global-wind-report-2014-annual-market-update/ [Accessed May 12, 2015].

Hagg, F., 1996. *User's documents SILANT (in Dutch)*, Amsterdam.

Hand, M.M. et al., 2001. Unsteady Aerodynamics Experiment Phase VI : Wind Tunnel Test Configurations and Available Data Campaigns Unsteady Aerodynamics Experiment Phase VI : Wind Tunnel Test Configurations and Available Data Campaigns. , (December).

Hansen, M.O.L., 2008. *Aerodynamics of Wind Turbines* 2nd ed., London: Earthscan.

Herrig, A. et al., 2006. Trailing-edge noise measurements using a hot-wire based coherent particle velocity method. *24th AIAA Applied Aerodynamics* …. Available at: http://arc.aiaa.org/doi/pdf/10.2514/6.2006-3876 .

Howe, M.S., 1991. Noise produced by a sawtooth trailing edge. *The Journal of the Acoustical Society of America*, 90(July), pp.482–487. Available at: http://link.aip.org/link/?JASMAN/90/482/1

Hubbard, H.H. & Shepherd, K.P., 1990. *Wind turbine acoustics*, National Aeronautics and Space Administration, Office of Management, Scientific and Technical Information Division.

IEC 61400-11, 2002. IEC 61400-11 (2002): Wind turbine generator systems–Part 11: Acoustic noise measurement techniques.

J. E. Ffowcs Williams and L. H. Hall, 1970. Aerodynamic sound generation by turbulent flow in the vicinity of a scattering half plane. *Journal of Fluid Mechanics*, 40, pp.657–670.

Kim, T. et al., 2010. Design of low noise airfoil with high aerodynamic performance for use on small wind turbines. *Science in China Series E: Technological Sciences*, 53(1), pp.75–79. Available at: http://link.springer.com/10.1007/s11431-009-0415-7.

Kulfan, B.M., 2008. Universal Parametric Geometry Representation Method. *Journal of Aircraft*, 45(1), pp.142–158. Available at: http://arc.aiaa.org/doi/abs/10.2514/1.29958 .

Kundu, P.K. & Cohen, I.M., 2008. *Fluid mechanics* 4th ed., Academic Press.

Lindenburg, C., 2004. Modelling of rotational augmentation based on engineering considerations and measurements. *European Wind Energy Conference, London*. Available at: ftp://ecn.nl/pub/www/library/report/2004/rx04131.pdf.

Liu, S. & Janajreh, I., 2012. Development and application of an improved blade element momentum method model on horizontal axis wind turbines. *International Journal of Energy and Environmental Engineering*, 3(1), p.30. Available at: http://www.journal-ijeee.com/content/3/1/30.

Lowson, M., 1993. A new prediction model for wind turbine noise. In *Renewable Energy-Clean Power 2001*. pp. 177–182. Available at: http://ieeexplore.ieee.org/xpls/abs_all.jsp?arnumber=264101 [Accessed April 19, 2013].

Lutz, T., Wolf, A. & Würz, W., 2011. *Design and Verification of an Airfoil with Trailing-Edge Flap and Unsteady Wind-Tunnel Tests*, Stuttgart.

Manwell, J.F., McGowan, J.G. & Rogers, A.L., 2002. *Wind energy explained: theory, design and application. 2002,*

Meadows, D.. et al., 1972. *The Limits to Growth*, Available at: http://www.donellameadows.org/wp-content/userfiles/Limits-to-Growth-digital-scan-version.pdf.

Montgomerie, B., 2004. *Methods for Root Effects, Tip Effects and Extending the ANgle of Attack Range to +- 180, with application to Aerodynamics for Blades on Wind Turbines and Propellers.pdf,*

Moriarty, P., 2005. NAFNoise User’s guide.

Moriarty, P., Guidati, G. & Migliore, P., 2005. Prediction of turbulent inflow and trailing-edge noise for wind turbines. *Proc. of the 11th AIAA/CEAS ...*, (May), pp.23–25. Available at: http://arc.aiaa.org/doi/pdf/10.2514/6.2005-2881 [Accessed April 18, 2013].

NWEA, 2015. Windenergie, de feiten. Available at: http://www.nwea.nl/windenergie-de-feiten [Accessed May 12, 2015].

Oerlemans, S., 2011. *Wind turbine noise : primary noise sources*,

Oliveira, G. De, 2014. Private correspondence.

De Oliveira, G., 2011. *Wind Turbine Airfoils with Boundary Layer Suction - A Novel Design Approach*. TU-Delft.

Parchen, R., 1998. *Progress report DRAW : a prediction scheme for trailing edge noise based on detailed boundary layer characteristics,*

Reuss Ramsay, R., Hoffmann, M.J. & Gregorek, G.M., 1995. *Effects of Grit Roughness and Pitch Oscillations on the S809 Airfoil*, Golden, CO. (US).

Van Rooij, R., 1996. *Modification of the boundary layer calculation in RFOIL for improved airfoil stall prediction,*

Sant, T., 2007. *Improving BEM - based Aerodynamic Models in Wind Turbine Design Codes*.

Schlichting, H., 1968. *Boundary-Layer Theory*, New York: McGraw-Hill.

Shen, W.Z. et al., 2005. Tip loss corrections for wind turbine computations. *Wind Energy*, 8(4), pp.457–475.

Snel, H., Houwink, R. & Bosschers, J., 1994. Sectional prediction of lift coefficients on rotating wind turbine blades in stall. Available at: ftp://www.kernenergie.nl/pub/www/library/report/1993/c93052.pdf.

Tangler, J. & Kocurek, J.D., 2005. Wind Turbine Post-Stall Airfoil Performance Characteristics Guidelines for Blade-Element Momentum Methods. *Power*, (October 2004), pp.1–10. Available at: http://www.nrel.gov/docs/fy05osti/36900.pdf.

Timmer, W. a. & van Rooij, R.P.J.O.M., 2003. Summary of the Delft University Wind Turbine Dedicated Airfoils. *ASME 2003 Wind Energy Symposium*, pp.11–21. Available at: http://proceedings.asmedigitalcollection.asme.org/proceeding.aspx?articleid=1598539.

Timmer, W.A., 2010. Aerodynamic characteristics of wind turbine blade airfoils at high angles-of-attack. In *TORQUE 2010: The Science of Making Torque from Wind*. pp. 71–78.

Timmer, W.A., 2014. Private correspondence.

Tulapurkara, E.G., 2015. Flight dynamics I - Airplane performance web course notes. Available at: http://nptel.ac.in/courses/101106041/8 [Accessed March 1, 2015].

Vargas, L., 2008. *Wind Turbine Noise Prediction*. Technical University of Lisbon.

Viterna, L.A. & Corrigan, R.D., 1982. Fixed pitch rotor performance of large horizontal axis wind turbines. *Annual Review of Fluid Mechanics*, 15(1), pp.69–85. Available at: http://naca.larc.nasa.gov/search.jsp?R=524871&id=2&as=false&or=false&qs=Ns=HarvestDate|1&N=4294871842.

Wagner, S. (Siegfried) et al., 1996. *Wind turbine noise / S. Wagner, R. Bareiss, G. Guidati*, Berlin ; New York : Springer.

White, F.M., 2009. *Fluid Mechanics* 4th ed., Available at: http://dx.doi.org.proxy.lib.utk.edu:90/10.1007/978-3-540-71343-2.

White, F.M., 1991. *Viscous Fluid Flow*, New York: McGraw-Hill.

WWEA, 2014. Half-year Report 2014. Available at: http://www.wwindea.org/webimages/WWEA_half_year_report_2014.pdf [Accessed May 12, 2015].

Zhu, W.J., 2004. *Modelling Of Noise From Wind Turbines*. Technical University of Denmark.

Zingg, D.W., Nemec, M. & Pulliam, T.H., 2008. A comparative evaluation of genetic and gradient-based algorithms applied to aerodynamic optimization. *Revue européenne de mécanique numérique*, 17(1-2), pp.103–126.

Appendix A - SILANT input file

```
# Properties for noise prediction with Silant:
air_density      1.225
rotor_blades     3
root_radius      2.5
rotor_radius     46.5
wind_velocity    10
pitch_angle      -1
rotor_speed      14.4
tilt_angle       6
cone_angle       2
9  Number of files in airfoil_table
"Profile1.dat"   12
"Profile2.dat"   14
"Profile3.dat"   14
"Profile4.dat"   13
"Profile5.dat"   13
"Profile6.dat"   12
"Profile7.dat"   12
"Profile8.dat"   12
"Profile9.dat"   10.2
# Radius    Prof    Chord    Twist   PitchAxis    Alpha    U_eff
21  Length of table with blade properties
   4.282           0        2.917    17.834  50        35.699  9.243
   6.423           1        3.462    18.910  25        18.646  13.236
   8.565           1        3.307    16.837  25        11.143  15.783
   10.706          1        3.158    14.775  25        8.571   18.487
   12.847          2        2.992    12.705  25        7.959   21.412
   14.988          3        2.832    10.674  25        7.357   24.368
   17.129          4        2.668    8.967   25        7.360   27.397
   19.270          4        2.505    7.455   25        7.155   30.438
   21.412          5        2.344    5.959   25        7.318   33.649
   23.553          5        2.179    4.595   25        7.764   36.764
   25.694          6        2.020    3.619   25        7.811   39.884
   27.835          6        1.862    2.803   25        7.843   43.025
   29.976          7        1.704    2.065   25        7.907   46.179
   32.117          7        1.546    1.329   25        8.096   49.343
   34.259          8        1.387    0.607   25        8.391   52.494
   36.400          8        1.238    -0.010  25        8.572   55.670
   38.541          8        1.101    -0.528  25        8.755   58.854
   40.682          9        0.970    -1.015  25        8.973   62.041
   42.823          9        0.848    -1.456  25        9.152   65.234
   44.964          9        0.734    -1.895  25        9.384   68.430
   46.267          9        0.659    -2.164  25        9.584   70.376
hub_height       80        #hhub
roughn_length    0.05      #z0
ksi_max          0.99      #ksi_max
spl_calc         1         #Calculate SPLs?
meteo_calc       1         #calculate refraction and ground effect?
r_max            112       #r_max
observerheight   0         #height of observer
n_r              1         #n_r
n_phi            1         #n_phi
n_azi            1         #n_azi
elementfile      0         #file for comparison of   element contributions
azimuthfile      1         #file for comparison of   azimuth dependence
observerfile     1         #file for comparison of   observer positions
```

Appendix B - SILANT BL-file

Example of a SILANT boundary layer displacement thickness data file.

```
Profile9
2       14.4    # Nr of Reynolds, nr of AOA
0      3000000        3000000        4500000        4500000
2.0     0.023953       0.015701       0.022338       0.014883
2.2     0.024405       0.015441       0.022857       0.014663
2.4     0.024540       0.015234       0.023060       0.014485
2.6     0.024866       0.015068       0.023448       0.014345
2.8     0.025344       0.014810       0.023925       0.014104
3.0     0.025598       0.014570       0.024256       0.013879
3.2     0.025994       0.014377       0.024719       0.013693
3.4     0.026509       0.014227       0.025111       0.013537
3.6     0.026799       0.013974       0.025989       0.013297
3.8     0.027555       0.013743       0.026809       0.013082
4.0     0.028299       0.013552       0.027969       0.012905
4.2     0.029206       0.013357       0.030204       0.012751
4.4     0.030663       0.013104       0.037398       0.012457
4.6     0.038374       0.012824       0.043894       0.012154
4.8     0.046083       0.012565       0.045022       0.011979
5.0     0.047535       0.012377       0.045817       0.011839
                            .
                            .
                            .
11.0    0.097652       0.005468       0.083441       0.005760
11.2    0.105521       0.005207       0.090498       0.005524
11.4    0.113222       0.004931       0.097876       0.005304
11.6    0.120931       0.004646       0.105064       0.005091
11.8    0.128558       0.004349       0.112666       0.004883
12.0    0.136012       0.003869       0.119631       0.004666
12.2    0.143429       0.003386       0.126654       0.004446
12.4    0.150713       0.001385       0.133846       0.004103
12.6    0.158152       0.001374       0.141112       0.003863
12.8    0.165123       0.001363       0.148628       0.003592
13.0    0.172489       0.001353       0.156215       0.003295
13.2    0.179605       0.001343       0.162579       0.002082
13.4    0.186261       0.001334       0.168601       0.001082
13.6    0.192228       0.001325       0.174837       0.001075
13.8    0.198034       0.001316       0.181193       0.001067
14.0    0.203682       0.001307       0.186230       0.001059
14.2    0.209176       0.001298       0.192326       0.001052
14.4    0.214517       0.001289       0.197203       0.001044
```

Appendix C - BEM Validation

To calculate the velocity and angle of attack distribution along the blade of the wind turbine, the Blade Element Momentum Theory, as explained in section 2.3 is applied. The model is validated against experimental data of the NREL phase VI wind turbine from the Unsteady Aerodynamic Experiment (UAE). This turbine was mainly chosen because of the availability of the data.

The NREL Phase VI rotor is a two-bladed 10.1 meter diameter stall-regulated wind turbine rotor with a rated power of 19.8 kW. The blades are based on the S809 airfoil, and are both tapered and twisted. The twist and chord distributions as well as the blade planform and the airfoil shape can be seen in Figure C.1, Figure C.2 and Figure C.3.

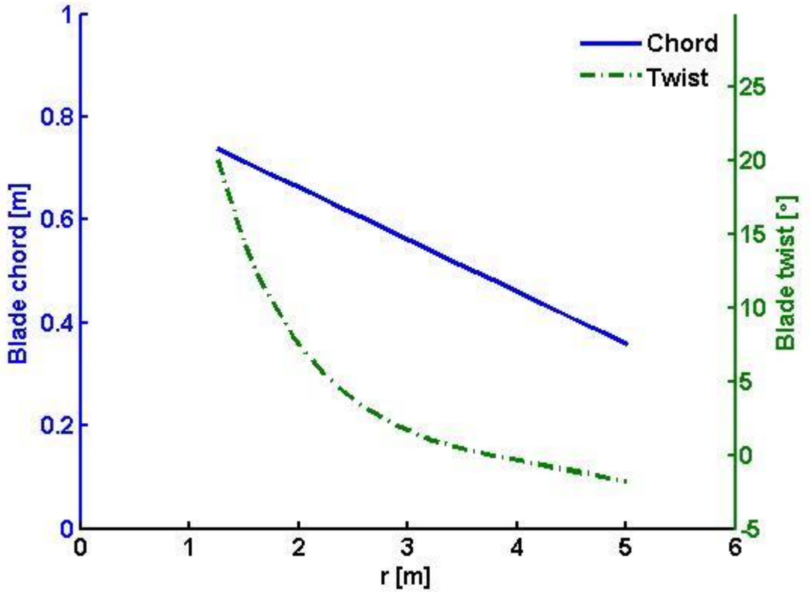

Figure C.1: blade chord and twist

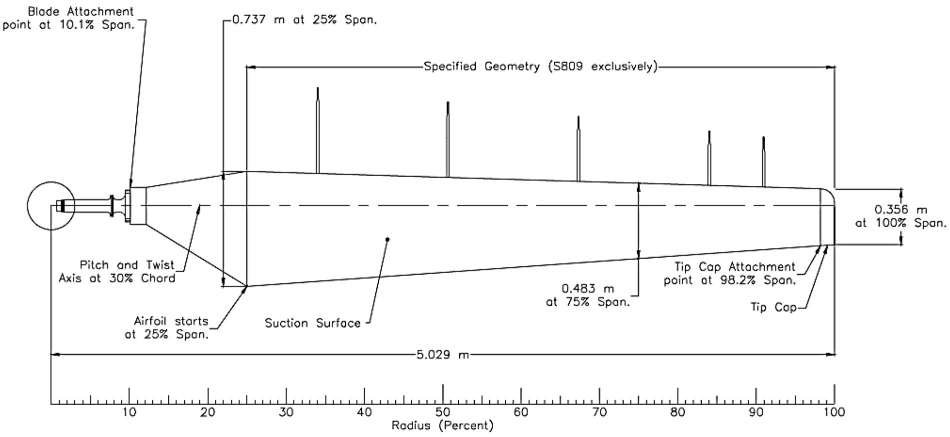

Figure C.2: blade planform (Hand et al. 2001)

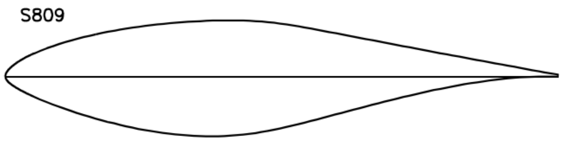

Figure C.3: S809 airfoil shape (Reuss Ramsay et al. 1995)

In the UAE Phase VI experiments, the turbine was tested in the NASA AMES wind tunnel over a wide range of operating conditions. Operating conditions that were varied contained: pitch angle, yaw angle, upwind/downwind configuration, RPM, among others. To validate the BEM model, only the experimental data collected in the H-configuration were considered. An overview of the specifications of the turbine along with the operating conditions is shown in Table C.1.

Table C.1: Turbine specifications and experimental test conditions

NREL Phase VI specifications			
Parameter	Value	Parameter	Value
No. of blades	2 [-]	Power regulation	Stall
Rotor diameter	10.06 [m]	Airfoil type	S809
Hub height	12.192 [m]	Blade chord	Figure C.1
Rated power	19.8 kW	Blade twist	Figure C.1
Test Conditions			
Parameter	Value	Parameter	Value
Tilt angle	0 [°]	Pitch angle	3 [°]
Cone angle	0 [°]	Density	1.244 [kg/m^3]
Rotational speed	71.63 [rpm]	Yaw angle	0 [°]

On the blade, several pressure taps were placed to acquire detailed surface pressure data; the taps are located at 30%, 47%, 63%, 80% and 95% of the radius. These pressure tap distributions were then integrated to obtain C_n, C_t and C_m. The blade was also equipped with five-hole pressure probes at 34%, 51%, 67%, 85% and 91% of the radius to measure the local inflow angle (Hand et al. 2001).

To verify whether the BEM model can accurately predict the flow conditions at the blade, the measurements from NREL are now compared to the prediction made by the code. Since these results are used as an input for Silant, the main focus is on the correct prediction of the spanwise distribution of V_{rel} and angle of attack α. The power predictions have to be accurate as well, because this is one of the optimization parameters. First, the accuracy of derived flow angles is tested. The LFA measured by the probes is compared to the calculated inflow angles by the BEM model. This is shown in Figure C.4 and Figure C.5.

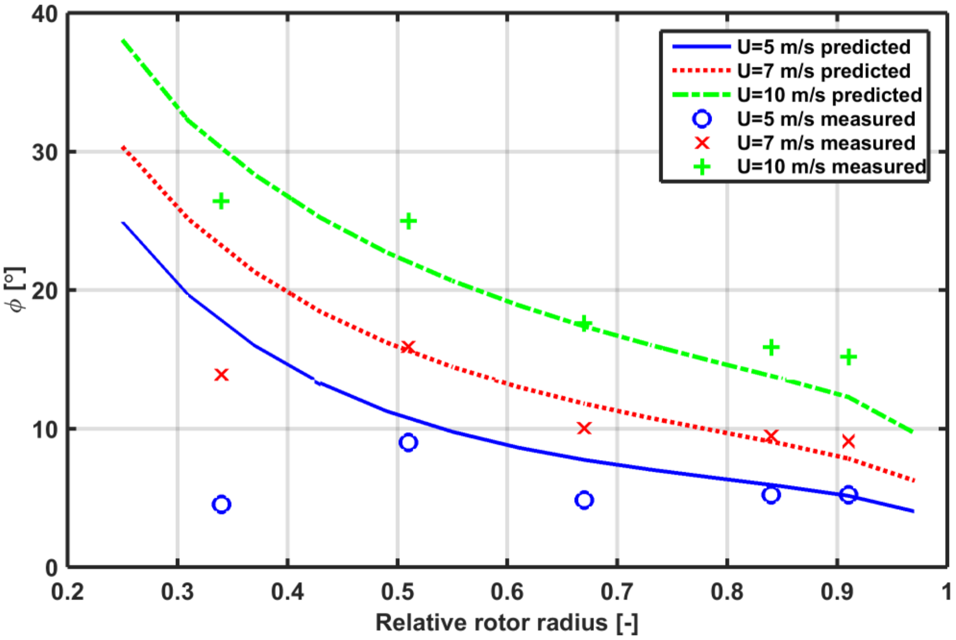

Figure C.4: Comparison of predicted inflow angle distribution with measurements for low wind speeds

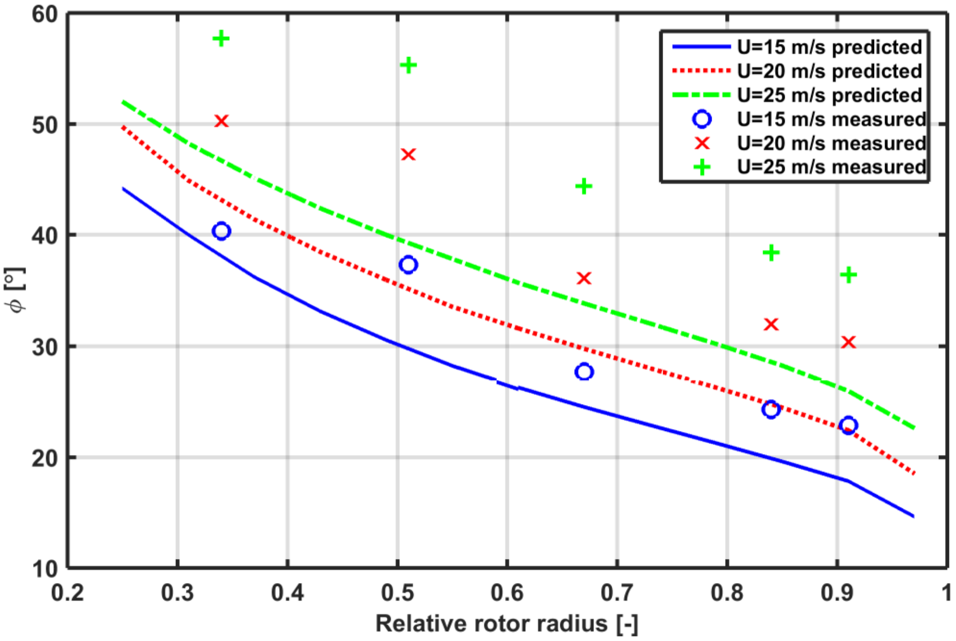

Figure C.5: Comparison of predicted inflow angle distribution with measurements for medium and high wind speeds

It can be observed that, at lower wind speeds, the BEM model manages to predict the local inflow angle fairly well, especially at the mid and outer section of the blade. The model has trouble predicting the angle in the root section of the blade. At higher wind speeds however, the BEM model is unable to accurately calculate the inflow angle. As the wind speeds increase, so does the error, and the maximum discrepancy between the measured and the calculated angles is about 15^{o}, which is considerably high. The prediction of the relative velocity compared to measurements at several wind speeds can be found in the figure below.

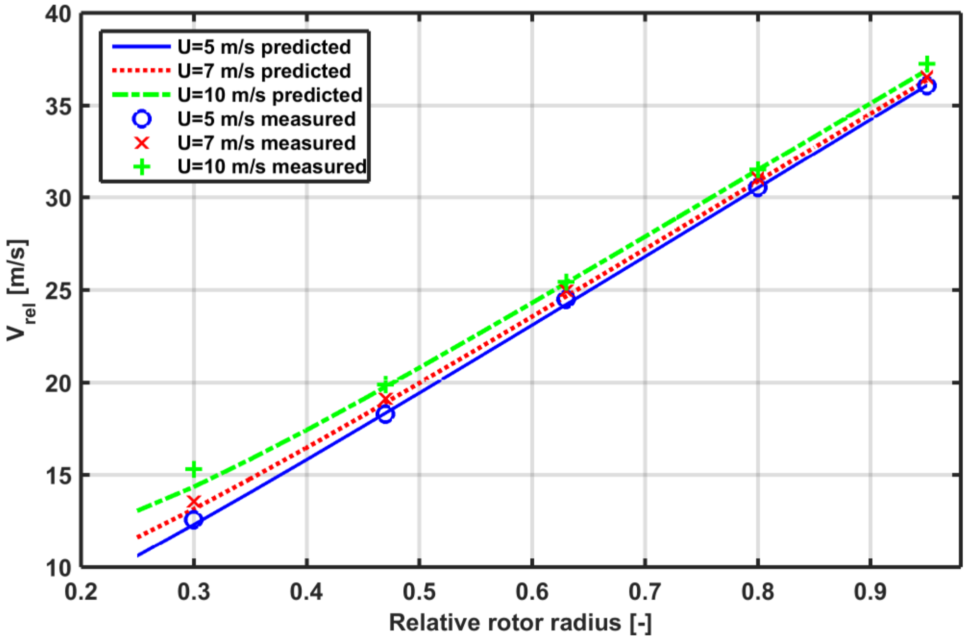

Figure C.6: Comparison of V_{rel}, calculated by the BEM model with derived from measurements for low inflow velocities

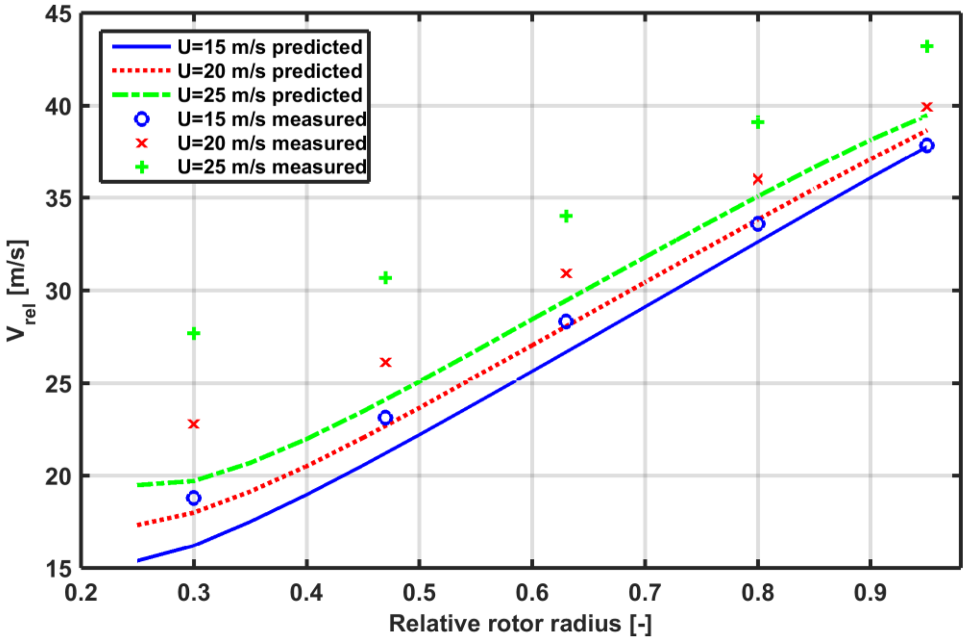

Figure C.7: Comparison of V_{rel}, calculated by the BEM model with derived from measurements for high inflow velocities

The same conclusions can be drawn when the relative wind speed is considered, which are shown in the Figure C.6 & Figure C.7 above. For low wind speeds, the BEM predictions are very good and the error is very small at every part of the blade. At higher wind speeds, again, the error increases as the wind speed goes up. It can therefore be concluded that the model performs adequately as long as the conditions remain sub-stall. When the turbine starts to experience stall behavior at higher wind speeds, the predictions become less and less accurate. Several reasons can be attributed to this. One of them that contributes to the error for higher wind speeds is that the Montgomerie extrapolation is not able to reproduce the exact stall behavior of the airfoil. The drag is somewhat under predicted while the decrease in lift in the stall region is less severe. Furthermore, although a 3D correction model is included, this too is never 100% accurate and further increases the error. These factors all affect the lift, drag and thereby induction and angle of attack prediction.

However, the fact that the BEM method becomes less capable of predicting the relative velocity and angle of attack at higher wind speeds is of lesser importance. The main goal of the BEM analysis is to provide the necessary input for the aero-acoustic prediction tool SILANT, which is exclusively used for an acoustic analysis. Since noise evaluation of a wind turbine is only performed for wind speeds between 6 and 10 m/s, it is especially important that the BEM model performs well in this range. For higher wind speeds, the noise emitted by the wind turbine is masked by the background noise from the wind itself. Furthermore, the predictions made by SILANT are based on a pitch-regulated wind turbine; the angles of attack will therefore mostly remain below stall angle and the error in the predictions made by the BEM code will be smaller.

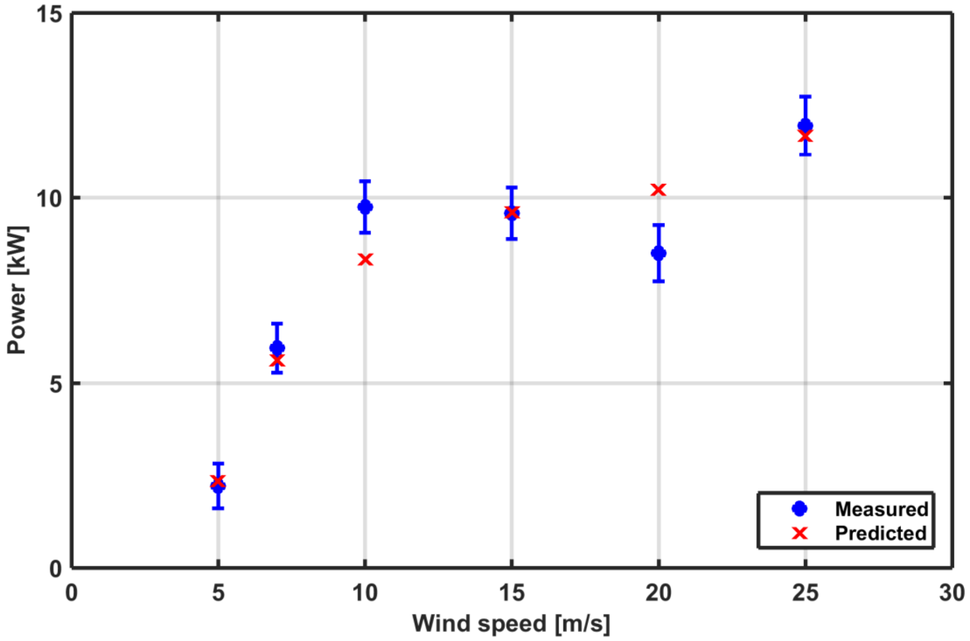

Figure C.8: NREL phase VI turbine predicted and measured power curve

Above, the measured aerodynamic power produced with the standard deviation is plotted along with the calculated power (Figure C.8). When the two are compared, the most noticeable aspect of the figure is that the power predictions at 15 and 25 m/s are quite accurate, while the calculated power at 10 and 20 m/s deviates quite significantly from the measured one. For reasons mentioned above, the BEM method is unable to predict the drop in power in stall conditions.

It can therefore be concluded, that for lower wind speeds, the BEM model predictions are reasonably accurate. At higher wind speeds, the model systematically under predicts the measured parameters. However, the occurrence of low to moderate wind speed is the highest; the BEM model calculation will in most cases be sufficiently accurate, and it is therefore a suitable tool for the purpose of predicting wind turbine noise.

Appendix D - Prediction of TBL-TE noise according to BPM model

In section 6.1.2, the general equations to compute the Turbulent Boundary Layer – Trailing Edge and Separation-Stall noise are presented. However, the details of the method still have to be clarified. This appendix provides the full set of expressions necessary to calculate the TBL-TE noise using the Brooks, Pope and Marcolini model.

Recall that the general expression to compute the TBL-TE noise comprise of three noise contributions, SPL_p, SPL_p and SPL_α, which have the following form:

$$SPL_{tot} = 10\log\left(10^{\frac{SPL_p}{10}} + 10^{\frac{SPL_s}{10}} + 10^{\frac{SPL_\alpha}{10}}\right) \tag{D.1}$$

$$SPL_p = 10\log\left(\frac{\delta_p^* M^5 s D_H}{r_e^2}\right) + A\left(\frac{St_p}{St_1}\right) + (K_1 - 3) + \Delta K_1 \tag{D.2}$$

$$SPL_s = 10\log\left(\frac{\delta_s^* M^5 s D_H}{r_e^2}\right) + A\left(\frac{St_s}{St_1}\right) + (K_1 - 3) \tag{D.3}$$

$$SPL_\alpha = 10\log\left(\frac{\delta_s^* M^5 s D_H}{r_e^2}\right) + B\left(\frac{St_s}{St_2}\right) + K_2 \tag{D.4}$$

These equations are applied if $\alpha \leq 12.5° \wedge \alpha \leq \alpha_{stall}$. The authors assumed that turbulent boundary layer flow changes to stalled flow conditions. At angles of attack above either of the two angles the following set of equations is used:

$$SPL_p = -\infty \tag{D.5}$$

$$SPL_s = -\infty \tag{D.6}$$

$$SPL_\alpha = 10\log\left(\frac{\delta_s^* M^5 s D_l}{r_e^2}\right) + A\left(\frac{St_s}{St_2}\right) + K_2 \tag{D.7}$$

This indicates that the noise in this case is totally dominated by separation stall noise. The Strouhal number at the pressure side and suction side are:

$$St_p = \frac{f\delta_p}{U} \tag{D.8}$$

$$St_s = \frac{f\delta_s}{U} \tag{D.9}$$

And

$$St_1 = 0.02M^{-0.6} \tag{D.10}$$

$$St_2 = St_1 \times \begin{cases} 1 & \alpha < 1.33° \\ 10^{0.0054(\alpha-1.33)^2} & 1.33° \le \alpha \le 12.5° \\ 4.72 & 12.5° < \alpha \end{cases} \tag{D.11}$$

The shape functions A and B are given in a similar manner:

$$A(a) = A_{min}(a) + A_R(a_0) \cdot [A_{max}(a) - A_{min}(a)] \tag{D.12}$$

$$B(b) = B_{min}(b) + B_R(b_0) \cdot [B_{max}(b) - B_{min}(b)] \tag{D.13}$$

In the function A, the terms $A_{max}(a)$ and $A_{min}(a)$ are defined as:

$$A_{min}(a) = \begin{cases} \sqrt{67.552 - 886.788a^2} - 8.219 & a < 0.204 \\ -32.665a + 3.981 & 0.204 \le a \le 0.244 \\ -142.795a^3 + 103.656a^2 - 57.757a + 6.006 & 12.5° < \alpha \end{cases} \tag{D.14}$$

$$A_{max}(a) = \begin{cases} \sqrt{67.552 - 886.788a^2} - 8.219 & a < 0.13 \\ -15.901a + 1.098 & 0.13 \le a \le 0.321 \\ -4.669a^3 + 3.491a^2 - 16.699a + 1.149 & 12.5° < \alpha \end{cases} \tag{D.15}$$

Where *a* is defined as the ratio of two Strouhal numbers:

$$a = \left|\log(St/St_{peak})\right| \tag{D.16}$$

Where St = St_p or St_s, St_{peak} = St_1,St_2 or $0.5(St_1+St_2)$. $A_R(a_0)$ is the interpolation factor determined from:

$$A_R(a_0) = \frac{-20 - A_{min}(a_0)}{A_{max}(a_0) - A_{min}(a_0)} \tag{D.17}$$

a_0 is a function of the chord Reynolds number Re (=Uc/ν):

$$a_0(Re) = \begin{cases} 0.57 & Re < 9.52 \cdot 10^4 \\ (-9.57 \cdot 10^{-13})(Re - 8.57 \cdot 10^5)^2 + 1.13 & 9.52 \cdot 10^4 \le Re \le 8.57 \cdot 10^5 \\ 1.13 & 8.57 \cdot 10^5 < Re \end{cases} \tag{D.18}$$

The subfunctions for shape function B can be computed in a similar manner:

$$B_{min}(b) = \begin{cases} \sqrt{16.888 - 886.788b^2} - 4.109 & b < 0.13 \\ -83.607b + 8.138 & 0.13 \le b \le 0.145 \\ -817.810b^3 + 355.210b^2 - 135.024b + 10.619 & 0.244 < b \end{cases} \tag{D.19}$$

$$B_{max}(b) = \begin{cases} \sqrt{16.888 - 886.788b^2} - 4.109 & b < 0.10 \\ -31.330b + 1.854 & 0.10 \leq b \leq 0.187 \\ -80.541b^3 + 44.174b^2 - 39381b + 2.344 & 0.187 < b \end{cases} \tag{D.20}$$

In these equations, b is the ratio of the Strouhal number defined in equation (D.9)

$$b = |\log(St_s/St_2)| \tag{D.21}$$

The interpolation factor $B_R(b_0)$ is:

$$B_R(b_0) = \frac{-20 - B_{min}(b_0)}{B_{max}(b_0) - B_{min}(b_0)} \tag{D.22}$$

Like, a_0, b_0 is a function of Reynolds number too:

$$b_0(Re) = \begin{cases} 0.30 & Re < 9.52 \cdot 10^4 \\ -4.48 \cdot 10^{-13} \cdot (Re - 8.57 \cdot 10^5)^2 + 0.56 & 9.52 \cdot 10^4 \leq Re \leq 8.57 \cdot 10^5 \\ 0.56 & 8.57 \cdot 10^5 < Re \end{cases} \tag{D.23}$$

In the individual SPL-contribution expressions (D.2) to (D.4), the parameters K1 and K2 are the amplitude functions:

$$K_1 = \begin{cases} 4.31\log(Re) + 156.3 & Re < 2.47 \cdot 10^5 \\ -9.0\log(Re) + 181.6 & 2.47 \cdot 10^5 \leq Re \leq 8.57 \cdot 10^5 \\ 128.5 & 8.0 \cdot 10^5 < Re \end{cases} \tag{D.24}$$

$$K_2 = K_1 + \begin{cases} -1000 & \alpha < \gamma_0 - \gamma \\ \sqrt{\beta^2 - (\beta/\gamma)^2(\alpha - \gamma_0^2)} + \beta_0 & \gamma_0 - \gamma \leq \alpha \leq \gamma_0 + \gamma \\ -12 & \gamma_0 + \gamma < \alpha \end{cases} \tag{D.25}$$

Where

$$\begin{cases} \gamma = 27.094Ma + 3.31 \\ \gamma_0 = 23.43Ma + 4.651 \\ \beta = 72.65Ma + 10.74 \\ \beta_0 = -34.19Ma - 13.82 \end{cases} \tag{D.26}$$

For nonzero angles of attack, the SPL_p contribution expression (D.4) contains the pressure level adjustment function ΔK:

$$\Delta K_1 = \begin{cases} \alpha\left[1.43\log Re_{\delta_p^*} - 5.29\right] & Re_{\delta_p^*} \leq 5000 \\ 0 & 5000 < Re_{\delta_p^*} \end{cases} \tag{D.27}$$

Where $Re_{\delta_p^*}$ is the Reynolds number based on the pressure side displacement thickness:

$$Re_{\delta_p^*} = \frac{U \cdot \delta_p^*}{\nu} \tag{D.28}$$

Note: all angles in the appendix are in degrees.

Appendix E - Modified BPM model: comparison with other airfoils

This appendix evaluates the predictive capabilities of the modified BPM model more thoroughly. Because section 7.2 only contains a comparison with a single airfoil, it is desirable to check whether the same degree of accuracy is obtained for other airfoils as well. The airfoils considered in this appendix are the NREL S831 and the Risø B1-18, both of 18% thickness. The assessment only includes a comparison for moderately high positive angles of attack, for noise levels in the optimization will merely comprise of these angles.

The airfoils are both part of the same measurement campaign (Devenport et al. 2010), conducted at the Viriginia Tech (VT) Stability Wind Tunnel , and sponsored by the NREL. The wind tunnel is a continuous, single-return, subsonic wind tunnel with 7.3m long removable rectangular test sections of square cross section. The far-field noise was measured by means of an equal aperture spiral microphone array, containing 63 microphones. These were positioned behind a Kevlar acoustic transparent cloth outside of the test section, at a distance of 3 meter. The data were collected in 1/12-octave bands, so it is therefore necessary to convert to 1/3-octave bands for comparison purposes.

In the measurement campaign, the airfoils were subjected to various operating conditions; they are presented to the reader in the table E.1 below.

Table E.1: operating conditions of the VT measurement campaign

Case no.	**airfoil**	**c [m]**	**Trip**	**α [°]**	**Re [-]**	**U [m/s]**	**Ma [-]**
1	B1-18	0.914	No trip	3	3.15×10^6	56.0	0.1639
2	B1-18	0.914	No trip	6	3.15×10^6	56.0	0.1638
3	S831	0.914	No trip	3	3.15×10^6	56.0	0.1626
4	S831	0.914	No trip	6	3.15×10^6	56.0	0.1627

As can be seen in the table, the Reynolds numbers considered in this campaign are slightly higher than those used in section 7.2. This combined with a larger chord, results in lower flow speeds necessary to reach the desired Reynolds number. These conditions are applied to the modified BPM model, and compared to the Virginia Tech measurements; the results can be found in the figures below.

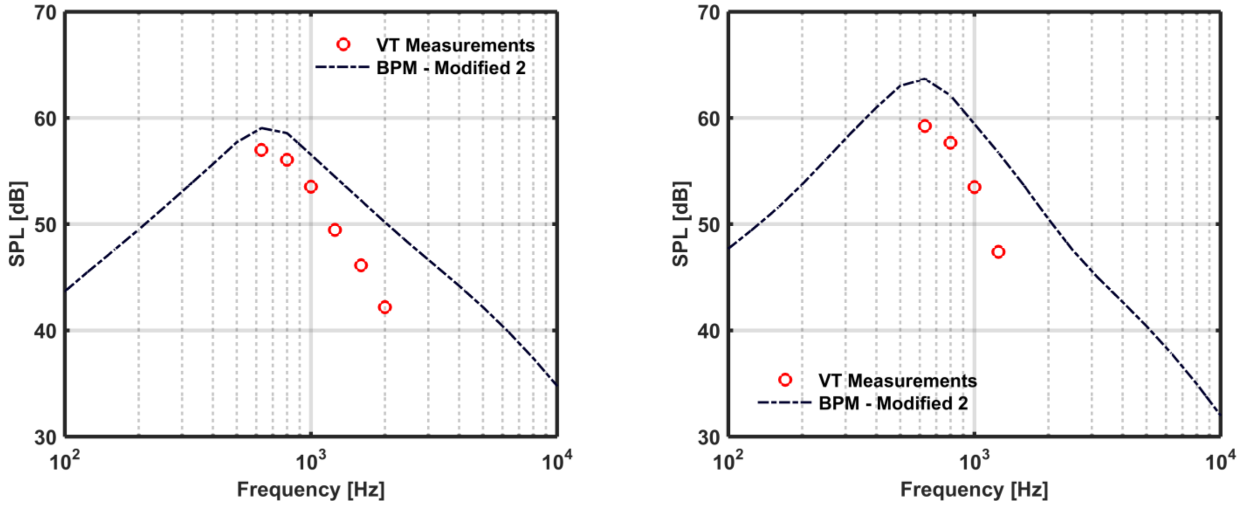

(a) Risø B1-18, 3 degrees (b) Risø B1-18, 6 degrees

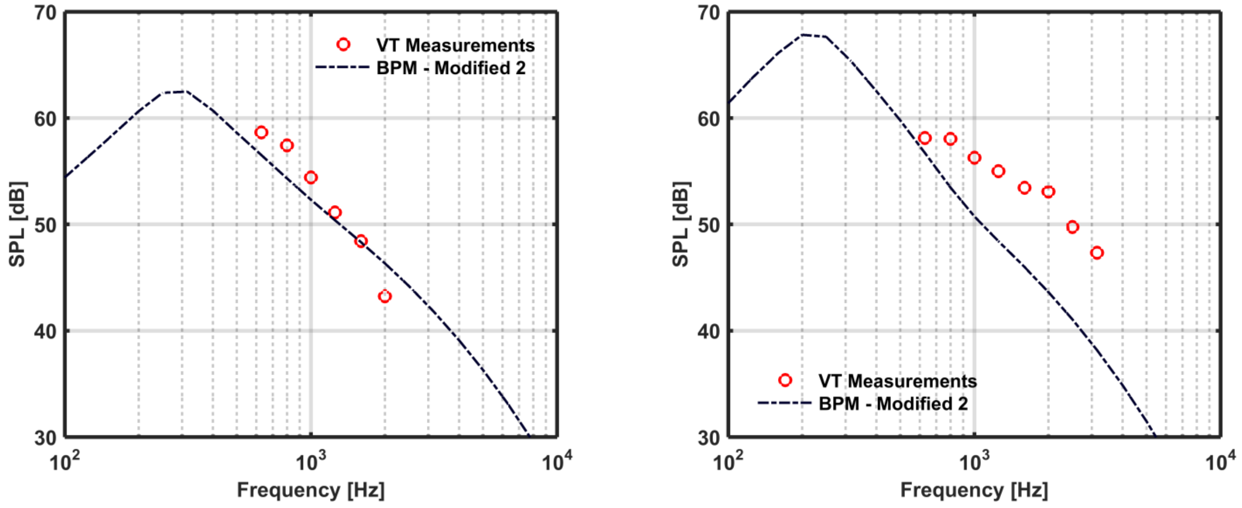

(c) S831 airfoil, 3 degrees (d) S831 airfoil, 6 degrees

Figure E.1: Noise prediction for the S831 and Risø B1-18 airfoils at 3 and 6 degrees for a Reynolds number of ~3 million at a flow velocity of 56 m/s

The figures indicate that the noise prediction at an angle of attack of 3 degrees is reasonable, especially for the S831 airfoil. In case of the B1-18 airfoil, the prediction is not as accurate. The modified BPM model overpredicts the SPL by a few dB.

For an angle of attack of 6 degrees, the modified BPM model performs slightly worse. For the S831 airfoil, the slope of the predictions matches the slope of the measurements. However, the curve of the calculated SPL is shifted upwards by ±4 dB. As for the S831 airfoil, the roll-off of the measurements deviates from the one computed by the BPM model. The maximum noise level also appears to be higher. This cannot be determined with certainty, since the VT measurements only cover a limited frequency range (500-5000 hz).